



HAL
open science

Three-dimensional particle tracking velocimetry for the study of thermal convection airflow in buildings

Sijie Fu

► **To cite this version:**

Sijie Fu. Three-dimensional particle tracking velocimetry for the study of thermal convection airflow in buildings. Other. Université Côte d'Azur, 2016. English. NNT : 2016AZUR4078 . tel-01450272

HAL Id: tel-01450272

<https://theses.hal.science/tel-01450272>

Submitted on 31 Jan 2017

HAL is a multi-disciplinary open access archive for the deposit and dissemination of scientific research documents, whether they are published or not. The documents may come from teaching and research institutions in France or abroad, or from public or private research centers.

L'archive ouverte pluridisciplinaire **HAL**, est destinée au dépôt et à la diffusion de documents scientifiques de niveau recherche, publiés ou non, émanant des établissements d'enseignement et de recherche français ou étrangers, des laboratoires publics ou privés.

UNIVERSITE NICE SOPHIA ANTIPOLIS - UFR Sciences
Ecole Doctorale en Sciences Fondamentales et Appliquées EDSFA

T H E S E

pour obtenir le titre de
Docteur en Sciences
de l'UNIVERSITE Nice Sophia Antipolis

Discipline : Sciences pour l'Ingénieur

présentée et soutenue par

Sijie FU

**Vélocimétrie par suivi 3D de particules pour la caractérisation
des champs thermo-convectifs dans le bâtiment**

Thèse dirigée par Pascal Henry BIWOLE et Richard PASQUETTI

soutenue le 31 Octobre 2016

Jury:

M.	Christian INARD	Professeur	Rapporteur
Mme.	Amina MESLEM	Professeur	Rapporteur
M.	Pascal Henry BIWOLE	Maître de Conférences	Directeur de thèse
M.	Richard PASQUETTI	DR CNRS	Directeur de thèse
M.	Nicolas COSTE	Docteur Ingénieur	Examineur
M.	Christian MATHIS	CR CNRS	Examineur

Vélocimétrie par suivi 3D de particules pour la caractérisation des champs thermo-convectifs dans le bâtiment

Résumé: L'objectif de cette thèse est de réaliser une étude approfondie sur la vélocimétrie par suivi 3D de particules (3D Particle Tracking Velocimetry, 3D PTV) pour l'air intérieur convectif thermique. Ce travail concentre principalement sur l'étude de la littérature, l'évaluation de performance des algorithmes de mesure de la 3D PTV, et l'étude expérimentale d'air intérieur convectif thermique en utilisant la technologie 3D PTV.

Dans le chapitre 1, la technologie 3D PTV typique et ses principales applications antérieures pour l'étude d'air intérieur sont examinées. Les quatre principales parties du système de mesure 3D PTV sont introduites, et cette étude suggère que la technologie 3D PTV a besoin de nouvelles améliorations pour l'étude d'air intérieur. En outre, La technologie de vélocimétrie par traces de particules (Particle Streak Velocimetry) et ses principales applications rencontrées dans l'étude des écoulements d'air intérieur sont également introduites.

Dans le chapitre 2, les performances de mesure d'un algorithme de corrélation croisée typique 2D PIV et un algorithme de corrélation croisée modifié 3D PTV sont comparées numériquement du point de vue de la densité de suivi, qui est l'indice indiquant la difficulté du suivi et qui est rarement considéré dans les études antérieures. Et une comparaison expérimentale entre deux algorithmes sont effectués.

Dans le chapitre 3, les performances de mesure de plusieurs algorithmes complets de 3D PTV sont ensuite comparées numériquement. Les différences entre ces algorithmes sont générées par différents algorithmes de suivi temporel et méthodes d'appariement spatial. La comparaison est basée sur la précision, la couverture du volume de mesure, et la longueur de la trajectoire pour chaque algorithme, relativement à la densité de suivi des particules et au nombre total d'images. Les algorithmes les plus performants sont en outre comparés expérimentalement dans un écoulement réel tridimensionnel dans une cavité cubique.

Dans le chapitre 4, sur la base de l'analyse des algorithmes de 3D PTV, l'étude expérimentale d'écoulements d'air intérieur générés par la méthode de ventilation par mélange est conduite. L'investigation est effectuée en conditions isotherme, anisotherme, et en présence d'une source de chaleur. Grâce aux mesures expérimentales, les trajectoires d'écoulements d'air, la vitesse et la température sont obtenus. A partir de ces résultats, certaines structures d'écoulement d'air sont détectées. Une méthode est proposée pour traiter les résultats expérimentaux pour la validation et le développement de modèles CFD.

Mots-clés: Vélocimétrie par suivi 3D de particules, écoulement de l'air intérieur, performance de la mesure, algorithmes, densité de suivi, simulation, investigation expérimentale

Three-dimensional particle tracking velocimetry for the study of thermal convection airflow in buildings

Abstract: The objective of this thesis is to conduct a comprehensive study on 3D Particle Tracking Velocimetry (PTV) for thermal convective indoor airflow. This work mainly concentrates on the literature survey, the performance evaluation of 3D PTV measurement algorithms, and the experimental investigation of thermal convective indoor airflow using 3D PTV measurement technology.

In chapter 1, typical 3D PTV technology and its main previous applications for indoor airflow study are carefully reviewed. The four main parts of 3D PTV measurement system are introduced, and the future improvements needed for the 3D PTV technology applied in airflow is underlined. Besides, Particle Streak Velocimetry and its main previous applications for indoor airflow fields are also introduced.

In chapter 2, the measurement performance of a typical 2D PIV cross-correlation algorithm and a modified 3D PTV cross-correlation algorithm are compared numerically from the perspective of tracking density, which is the index of tracking difficulty and is seldom considered in the previous study. In addition, an experimental comparison between two algorithms is conducted.

In chapter 3, the measurement performances of seven complete 3D PTV algorithms are compared numerically. Different temporal tracking algorithms and spatial matching methods generate the differences among these algorithms. The comparison is based on the accuracy, the measuring volume coverage, and the achievable correct trajectory length of each algorithm with respect to the particle tracking density and the total number of frames. The measurement algorithms showing better performances in numerical study are further compared on the experimental measurement of a real three dimensional airflow in a cubic cavity.

In chapter 4, based on the analysis of 3D PTV technology in the thesis, the experimental investigation of indoor airflow generated by mixing ventilation method is conducted. The investigation is done for isothermal condition, non-isothermal condition, and heat source condition. Through the experimental measurements, the airflow's trajectories, velocity and temperature are obtained, and some airflow structures are detected from these information. A method is proposed to further process the original experimental results, and benchmark experimental data for validating and developing CFD models is generated.

Keywords: 3D Particle Tracking Velocimetry, indoor airflow, measurement performance, algorithms, tracking density, numerical simulation, experimental investigation

TO MY FAMILY

Acknowledgments

First and foremost, I would like to express my sincere gratitude to my advisors Dr. Richard PASQUETTI and Dr. Pascal Henry BIWOLE for the help and support during the past three years. Dr. Richard PASQUETTI has always been kind to answer the questions during the research progress. Dr. Pascal Henry BIWOLE gave me most directions, help and encouragements. When I faced the difficulties or was in doubt about the research results, he always gave me confidence and encouragements. He has never spared his time to discuss with me about the research and correct my scientific publications. He also gave me much help for my life in France. Without their valuable help, this work would not have been achieved. I'm honoured of being their student.

I am grateful to Dr. Christian MATHIS for all his valuable contributions in daily work, and for being a member of my thesis committee.

I would like to thank Dr. Harunori N. YOSHIKAWA and Dr. Philippe MAISSA for their help in daily work.

I would also like to express my thanks to Pr. Amina MESLEM for welcoming me to visit her research group, and for reviewing my thesis as the member of my thesis committee. The visit was a pleasant and valuable experience.

I would also like to express my appreciation and thanks to Pr. Christian INARD and Dr. Nicolas COSTE for being as the members of my thesis committee.

I would also like to thank my colleagues in LJAD, it is very pleasant to work in such a laboratory.

Special thanks go to my teachers and friends who supported me during all the periods of my studies.

Last but not least, I would like to express my deepest gratitude to my parents for their continuous love, support and encouragements during all the periods of my studies.

This thesis work was financially supported by the Conseil Régional PACA.

Contents

Introduction.....	1
Introduction.....	5
1 Revue du suivi Lagrangien de particules pour l'étude des écoulements d'air intérieur	9
Particle Tracking Velocimetry for indoor airflow fields: A review.....	11
Abstract.....	11
1. Introduction.....	12
2. PTV equipments and methods for indoor applications.....	13
2.1 Illumination system.....	14
2.2 Tracer particles.....	15
2.3 Image recording devices.....	17
2.4 Tracking algorithms.....	18
3. Applications of PTV in indoor airflow field measurements.....	23
4. PSV technologies and applications for indoor airflow.....	29
5. Limitations and future developments.....	31
5.1 Equipment.....	31
5.2. Methods.....	31
6. Conclusion.....	32
Acknowledgements.....	32
2 Comparaison numérique et expérimentale de la précision et de l'exactitude de la vélométrie 3D par suivi de particules (PTV) et de la vélométrie par images de particules (PIV) pour l'étude des écoulements d'air intérieur.....	35
Numerical and Experimental Comparison of 3D Particle Tracking Velocimetry (PTV) and Particle Image Velocimetry (PIV) Accuracy for Indoor Airflow Study.....	39
Abstract.....	39
1. Introduction.....	40
2. Comparing the effect of tracking density on 3D PTV and typical PIV.....	41
2.1 Synthetic images.....	42
2.2 Measurement algorithms.....	44
2.3 Evaluation parameters.....	47
2.4 Results.....	48
3. Comparison of 3D PTV and typical PIV for experimental measurement.....	52
3.1 Experiment set-up.....	52
3.2 Results.....	54
4. Conclusions.....	55
Acknowledgements.....	55
3 Comparaison numérique et expérimentale d'algorithmes complets de vélométrie 3D par suivi de particules (PTV) algorithmes pour l'étude des écoulements d'air intérieur ...	57

Numerical and Experimental Comparison of Complete Three-dimensional Particle Tracking Velocimetry (PTV) algorithms for Indoor Airflow Study.....	61
Abstract.....	61
1. Introduction	62
2. Descriptions of the compared complete 3D particle tracking algorithms	63
2.1 Multi-camera calibration	64
2.2 Image processing	64
2.3 Particle center detection.....	65
2.4 Spatial matching and 3D reconstruction.....	65
2.5 Temporal tracking algorithms.....	67
2.6 Flow chart of the complete 3D particle tracking algorithms	68
3. Numerical study	69
3.1 Synthetic images	69
3.2 Results.....	71
3.2.4 Further experimental tests of airflow using Plexiglas cuboid cavity	75
4. Discussions	79
5. Conclusions	79
Acknowledgment.....	80
Appendix	81
4 Etude expérimentale d'écoulements d'air intérieur par vélocimétrie par suivi 3D de particules (PTV).....	83
Experimental Investigation of Indoor Airflow Distribution using 3D Particle Tracking Velocimetry (PTV) Technology	85
Abstract.....	85
1. Introduction	86
2. Experimental facility, condition and procedure	87
2.1 Experimental facility	87
2.2 Experimental condition.....	88
2.3 Experimental procedure.....	89
3. Experimental results	92
3.1 Isothermal condition	92
3.2 Non-isothermal condition.....	95
3.3 Heat source condition	101
3.4 Supplement	103
4. Conclusions	104
Acknowledgment.....	104
Appendix	105
Conclusions and perspectives	119
Conclusions and perspectives	121
Bibliography / Bibliographie	123

List of Figures

Figure 0-1: La part des différentes méthodes d'évaluation pour la performance de la ventilation dans les bâtiments [10].....	1
Figure 0-2: The share of different ventilation performance assessment methods in buildings [10]	5
Figure 1-1: Basic layout of 3D PTV for large-scale measurement.....	13
Figure 1-2: Front view of a BalcarQuadlite halogen lamp used for 3D PTV [45]	14
Figure 1-3: Single helium filled soap bubble. Light scattered on the shell can be seen. [54]	15
Figure 1-4: Sketch used for generation of neutrally buoyant helium filled soap bubbles: (a) the Orifice type nozzle; (b) the three-channel generator. [56]	16
Figure 1-5: Influence of bubble diameter and film thickness τ on density ratio of HFSSBs. [59]	16
Figure 1-6: Several calibration targets for large scale airflow measurement	20
Figure 1-7: Flow chart of particle tracking strategies	21
Figure 1-8: Measurement of global airflow field at a spliced plane with 100% ventilation rate by Yan, BEE group [46]	24
Figure 1-9: PTV measurement for natural convection using HFLBs: (a) Experimental facility; (b) 3D balloon trajectories. [47]	24
Figure 1-10: PTV measurement over a heater in a room [27]	25
Figure 1-11: Velocity field extracted recorded in a full-scale aircraft cabin mock-up: (a) from 2525 streaks; (b) from 4476 streaks. [91]	29
Figure 2-1: Biais pour les méthodes 3D PTV et PIV typiques sur la direction-x (a) et la direction-y (b) sous la condition de déplacement linéaire des particules dans la direction-x	36
Figure 2-2: Erreurs aléatoires pour les méthodes 3D PTV et PIV typiques sur la direction-x (a) et la direction-y (b) sous la condition de déplacement linéaire des particules dans la direction-x	37
Figure 2-3: Biais pour les méthodes 3D PTV et PIV typiques sur la direction-x (a) et la direction-y (b) sous la condition de déplacement circulaire des particules	37
Figure 2-4: Erreurs aléatoires pour les méthodes 3D PTV et PIV typiques sur la direction-x (a) et la direction-y (b) sous la condition de déplacement circulaire des particules	37
Figure 2-5: Biais pour les méthodes 3D PTV et PIV typiques sur la direction-x (a) et la direction-y (b) sous la condition de déplacement des particules sous écoulement de Kovaszny	38
Figure 2-6: Erreurs aléatoires pour les méthodes 3D PTV et PIV typiques sur la direction-x (a) et la direction-y (b) sous la condition de déplacement des particules sous	

écoulement de Kovaszny.....	38
Figure 2-7: An example of the synthetic images (512 pixel × 512 pixel)	43
Figure 2-8: Schematic of linear particle movement (a), circular particle movement (b) and Kovaszny flow particle movement (c, d)	44
Figure 2-9: Flow chart of particle tracking strategies [104]	45
Figure 2-10: Illustration of the identification algorithm for spatial matching	47
Figure 2-11: Bias of 3D PTV and typical PIV methods on x-direction (a) and y-direction (b) under the condition of linear particle motion along the x-direction.....	49
Figure 2-12: Random errors of 3D PTV and typical PIV methods on x-direction (a) and y-direction (b) for the condition of linear particle motion along the x-direction.....	49
Figure 2-13: Bias of 3D PTV and typical PIV methods on x-direction (a) and y-direction (b) under the condition of circular particle motion	50
Figure 2-14: Random errors of 3D PTV and typical PIV methods on x-direction (a) and y-direction (b) under the condition of circular particle motion	50
Figure 2-15: Bias of 3D PTV and typical PIV methods on x-direction (a) and y-direction (b) under the condition of Kovaszny flow particle motion	51
Figure 2-16: Random errors of 3D PTV and typical PIV methods on x-direction (a) and y-direction (b) under the condition of Kovaszny flow particle motion.....	51
Figure 2- 17: Outline of the low-speed tailpipe.	52
Figure 2-18: PIV measurement set-up	53
Figure 2-19: Low-speed tailpipe inside experimental room MINIBAT, Lyon, France. The position of the three PTV cameras is shown by white circles.	54
Figure 2-20: Comparison of velocity measurement results with PIV/PTV on a low-speed tailpipe.....	54
Figure 3-1: Le diagramme des sept algorithmes complets de suivi de particules en 3D comparées.....	58
Figure 3-2: Flow chart of main particle tracking strategies	63
Figure 3-3: Calibration target.....	64
Figure 3-4: Illustration of the identification algorithm for spatial matching [123]	66
Figure 3-5: Flow chart of the seven complete 3D particle tracking algorithms compared	69
Figure 3-6: The schematic of the two types of particle motions.....	71
Figure 3-7: An example of synthetic images with Beltrami flow solution from one camera's view.....	71
Figure 3-8: γ 3D (a) and E3D (b) of different 3D PTV algorithms performing on Kovaszny flow motion with respect to the tracking density	72
Figure 3-9: γ 3D (a) and E3D (b) of different 3D PTV algorithms performing on Beltrami flow motion with respect to the tracking density	73
Figure 3-10: L_{correct} of different 3D PTV algorithms performing on Kovaszny flow motion (a) and Beltrami flow motion (b) with respect to the tracking density.....	73
Figure 3-11: γ 3D (a) and E3D (b) of different algorithms performing on Kovaszny flow	

motion with respect to the number of tracked frames.....	74
Figure 3-12: γ 3D (a) and E3D (b) of different algorithms performing on Beltrami flow motion with respect to the number of tracked frames.....	74
Figure 3-13: $L_{correct}$ of different 3D PTV algorithms performing on Kovasznay flow motion (a) and Beltrami flow motion (b) with respect to the tracked frame	75
Figure 3-14: The mock-up of experimental set-up	76
Figure 3-15: The relevant facility of experimental set-up	76
Figure 3-16: The particle trajectories which the length is bigger than 10 using four algorithms.....	79
Figure 4-1: Organigramme du post-traitement des résultats de mesure 3D PTV.....	84
Figure 4-2: The schematic of experimental facility	88
Figure 4-3: The distributions of thermocouples inside test cavity.....	88
Figure 4-4: Flow chart of 3D PTV measurement	90
Figure 4-5: Camera calibration target	90
Figure 4-6: Flow chart of processing the results.....	92
Figure 4-7: The trajectories with respect to all cases under isothermal condition.....	93
Figure 4-8: Velocity magnitude contours with respect to all cases under isothermal condition.....	94
Figure 4-9: PDF of u , v , w with respect to all cases under isothermal condition (u : red, v : green, w : blue, the solid line is the Gaussian fit)	95
Figure 4-10: The trajectories with respect to all cases under non-isothermal condition. Volume $0\text{mm} < Z \leq 270\text{mm}$	96
Figure 4-11: The trajectories with respect to all cases under non-isothermal condition. Volume $270\text{mm} < Z \leq 540\text{mm}$	97
Figure 4-12: The trajectories with respect to all cases under non-isothermal condition. Volume $540\text{mm} < Z < 730\text{mm}$	98
Figure 4-13: Velocity magnitude contours with respect to all cases under non-isothermal condition.....	99
Figure 4-14: PDF of u , v , w with respect to all cases under non-isothermal condition (u : red, v : green, w : blue, the solid line is the Gaussian fit)	100
Figure 4-15: The average temperature difference between the air inlet and measured points, with respect to all cases under the non-isothermal condition.....	100
Figure 4-16: The trajectories with respect to all cases under heat source condition. Volume $Y > 506.5\text{mm}$	101
Figure 4-17: Velocity magnitude contours with respect to all cases under heat source condition.....	102
Figure 4-18: PDF of u , v , w with respect to all cases under heat source condition (u : red, v : green, w : blue, the solid line is the Gaussian fit)	103
Figure 4-19: The average temperature difference between the air inlet and measured points with respect to all cases under heat source condition.....	103

List of Tables

Table 1-1: Summary of PTV applications for indoor airflows	26
Table 1-2: Brief summary of PSV systems for indoor airflows	30
Table 3-1: Tracking density calculated for each camera with respect to four tracking algorithms.....	77
Table 3-2: Measured average velocity magnitude for the four algorithms evaluated (m/s)	77
Table 3-3: Average length of tracked particle trajectory (number of linked frames).....	77
Table 3-4: Calibration parameters of camera 1	81
Table 3-5: Calibration parameters of camera 2.....	81
Table 3-6: Calibration parameters of camera 3.....	82
Table 4-1: Inlet air velocity under isothermal condition.....	89
Table 4-2: Inlet air velocity and over-temperature of supply air to cavity air under non-isothermal condition	89
Table 4-3: Inlet air velocity and heat power under heat source condition.....	89
Table 4-4: Average velocity information for areas close to the selected Z planes with respect to case 3 under isothermal condition	105
Table 4-5: Average velocity information for areas close to the selected Z planes with respect to case 3 under non-isothermal condition.....	107
Table 4-6: Average velocity information for areas close to the selected Z planes with respect to case 4 under non-isothermal condition.....	110
Table 4-7: Average velocity information for areas close to the selected Z planes with respect to case 2 under heat source condition	113

Introduction

L'utilisation d'énergie et les émissions de carbone ont augmenté rapidement avec l'augmentation de la population et le développement économique dans le monde [e.g. 1-4], ce qui accroît les préoccupations au sujet des difficultés de stock, de l'épuisement des ressources énergétiques et au sujet des impacts environnementaux majeurs. En général, la consommation finale d'énergie est divisée en trois secteurs principaux : l'industrie, le transport et les 'autres', qui comprend la consommation d'énergie dans les bâtiments. Actuellement, la consommation d'énergie dans les bâtiments compte pour 20 %-40 % de la consommation d'énergie totale [5-7], par conséquent, le développement des bâtiments à faible consommation d'énergie, proche de zéro ou égal à zéro en bilan net est une tendance répandue.

Parmi les consommations d'énergie dans le bâtiment, la consommation de CVC (systèmes de chauffage, ventilation et climatisation) en constitue la plus grande partie, ce qui représente environ 10% à 20% de l'énergie finale dans les pays développés [5]. Par conséquent, la façon d'améliorer l'efficacité énergétique des systèmes CVC est toujours une affaire importante pour les chercheurs et les ingénieurs. Les performances des systèmes de ventilation et de distribution d'air, en tant que partie principale des systèmes CVC, affectent les consommations d'énergie totales dans les bâtiments [8], et ont aussi une influence directe sur la qualité de l'air intérieur (IAQ) [9, 10]. Afin d'améliorer les performances des systèmes de ventilation et de distribution d'air, les différentes méthodes d'évaluation ont été développées et appliquées. Chen [11] a résumé ces sept méthodes, dont des modèles analytiques, des modèles empiriques, des expérimentations à échelle réduite, des expérimentations à grande échelle, des modèles de réseau multizone, des modèles zonaux et enfin de la Computational Fluid Dynamics (CFD). Parmi ces méthodes, la CFD représente environ 70%, cf. 0-1. Cependant, en utilisant la technologie actuelle, il est encore impossible de prédire avec précision la structure des champs de vitesse d'air intérieur avec des caractéristiques particulières de turbulence à basse vitesse et de tridimensionnalité [12]. En outre une simulation CFD fiable doit également être basée sur des données expérimentales abondantes pour être validée. Par conséquent, la mesure expérimentale tient encore un rôle important.

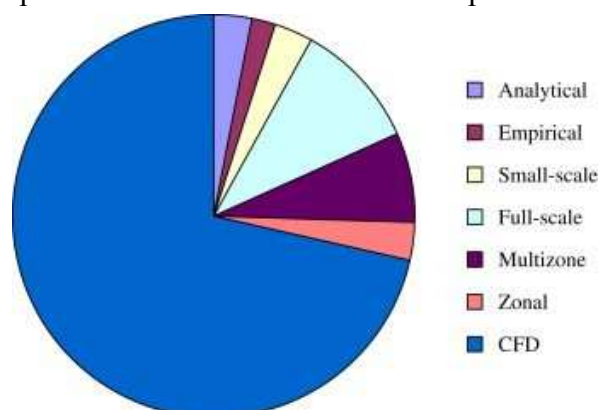


Figure 0-1: La part des différentes méthodes d'évaluation pour la performance de la ventilation dans les bâtiments [10]

Ce n'est pas une tâche facile que de mesurer l'écoulement d'air intérieur avec précision, car il se fait généralement à grande échelle, en tridimensionnel, turbulent et instable. Sun et Zhang [13] ont résumé les principales méthodes modernes pour la mesure l'écoulement d'air intérieur. Ces méthodes peuvent généralement être divisées en deux groupes: les technologies basées, soit sur une mesure ponctuelle, soit sur une mesure globale. La technologie ponctuelle, comme les sondes fil/film/sphère chaud, l'Anémométrie à Ultrasons (UA) et l'Anémométrie Laser Doppler (LDA), a été largement appliqué dans les expérimentations antérieures. Cependant, ces méthodes de mesure recueillent seulement des informations de point, et les outils de mesures ont généralement intrusifs, et peuvent parfois perturber l'écoulement d'air local. La technologie globale y compris la Vélocimétrie par images de particules (PIV) et la Vélocimétrie par suivi 3D de particules (3D Particle Tracking Velocimetry, 3D PTV), surmonte les insuffisances de la technologie ponctuelle, et a été appliquée de plus en plus ces dernières années. La technologie PIV, grâce à son développement industriel et aux systèmes commerciaux largement disponibles, a été la méthode la plus fréquemment utilise en vélocimétrie optique pour la mesure d'écoulement d'air intérieur [14]. Cependant, la technologie PIV typique donne généralement les champs vectoriels bidimensionnel au lieu de tridimensionnels, en dépit de sa résolution spatiale et temporelle, en raison des limites de l'éclairage et de la densité des particules traceurs. Par rapport à la technologie PIV, la technologie PTV peut surmonter ces lacunes, et peut fournir des trajectoires, ce qui est utile pour mieux comprendre les caractéristiques d'écoulement d'air intérieur. Par conséquent, la technologie PTV dévient progressivement un outil puissant pour la mesure d'écoulement d'air intérieur.

Bien que la technologie 3D PTV ait été développée et appliquée pour la mesure d'écoulement d'air intérieur dans les études antérieures, la recherche est principalement axée sur les développements et les vérifications des algorithmes de mesure indépendantes. Il n'y a cependant aucune recherche complet, en particulier sur l'évaluation de la performance. Par conséquent, cette thèse conduit tout d'abord une recherche complet sur la technologie 3D PTV, à partir des aspects de l'étude de la littérature et de l'évaluation de la performance. Ensuite, la technologie 3D PTV est utilisé comme principal outil de mesure pour conduire une étude expérimentale d'écoulement d'air intérieur sous la condition de ventilation de mélange. Opposée à la ventilation de déplacement, la ventilation de mélange ne repose pas sur la présence de sources de chaleur interne sa fin de ventiler la pièce et peut donc également être utilisée, mais sans s'y limiter, dans les cas (presque) isothermes. Par ailleurs, la ventilation de mélange peut être caractérisée par une distribution relativement uniforme [15,16]. Notre étude génère également une référence expérimentale en tridimensionnel sur la ventilation de mélange.

La section 1 propose un examen détaillé de la technologie 3D PTV et des applications antérieures dans le domaine de l'air intérieur. La technologie PTV typique pour les champs d'écoulement d'air intérieur, y compris les équipements et les méthodes, est introduite dans cette partie. Ensuite, les applications antérieures pertinentes sont résumées. Finalement, les limites et les perspectives de la 3D PTV sont discutées.

La section 2 compare les performances des algorithmes de mesure des 3D PTV et PIV

typiques, en utilisant les méthodes de simulation et expérimentale. En particulier, l'indice de densité de suivi, qui traduit la difficulté de suivi, est utilisé comme critère d'évaluation.

La section 3 évalue les performances des sept algorithmes de mesure complets de la 3D PTV, en utilisant la simulation et la méthode expérimentale. La densité de suivi et les cadres de suivi sont sélectionnés comme les facteurs d'évaluation. Grâce à cette section, l'algorithme et la procédure de mesure 3D PTV optimale peuvent être décidés, puis ultérieurement appliqués dans la section 4 pour conduire une investigation expérimentale.

Dans la section 4, est conduite une investigation expérimentale sur l'écoulement d'air intérieur avec ventilation de mélange, en utilisant la technologie 3D PTV optimale. Les résultats expérimentaux sont en tridimensionnel, ce qui est utile pour comprendre les caractéristiques de l'écoulement d'air intérieur. Sur la base des résultats expérimentaux, une analyse est effectuée, qui vise à générer une référence tridimensionnelle pour la simulation CFD à l'avenir.

Introduction

Energy use and carbon emissions have been growing rapidly along with the population increase and the economic development in the world [e.g.1-4], which raises concerns about supply difficulties, exhaustion of energy resources and heavy environmental impacts. Generally, final energy consumption is divided into three main sectors: industry, transport, and 'others', which includes building energy consumption. Nowadays, building energy consumption accounts for a 20%--40% of the total final energy consumption [5-7], therefore, developing low energy consumption, nearly zero energy consumption and net zero energy consumption buildings has been a prevalent trend.

Among building energy consumptions, the consumption of HVAC (Heating, Ventilation and Air Conditioning) systems is the largest part, which has accounted for about 10%-20% of final energy in developed countries [5]. Therefore, how to improve the energy efficiency of HVAC systems is always an important issue for researchers and engineers. The performance of ventilation and air distribution system, as a main part of HVAC systems, not only affects the total energy consumptions in buildings [8], but also has direct influence on the indoor airflow quality (IAQ) [9, 10]. In order to improve the performance of ventilation and air distribution systems, different assessment methods have been developed and applied. Chen [11] summarized these seven methods, including analytical models, empirical models, reduced-scale experiments, full-scale experiments, multizone network models, zonal models and Computational Fluid Dynamics (CFD). Among these methods, CFD accounts for about 70%, as the Figure 0-2 shows. However, it is still not possible to predict the structure of indoor airflow with the distinct characteristics of low speed turbulence and three-dimensionality accurately using current technology [12]. And a reliable CFD simulation usually needs abundant experimental data to validate. Therefore, experimental measurement still plays a significant role.

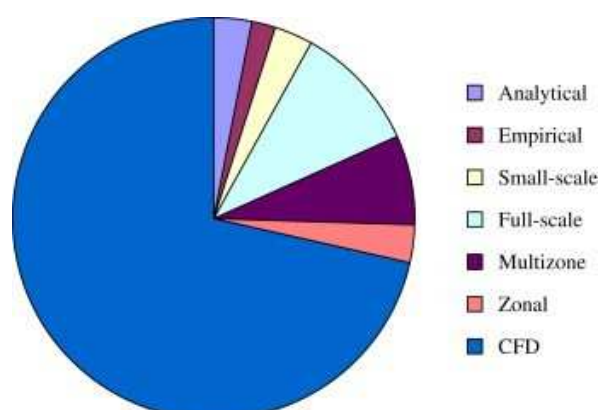


Figure 0-2: The share of different ventilation performance assessment methods in buildings [10]

It is not an easy task to measure the indoor airflow accurately, because it is usually large-scale, three-dimensional, turbulent and unsteady. Sun and Zhang [13] summarized main

modern methods for indoor airflow measurement. These methods generally can be divided into two groups: point-wise technology and global-wise technology. Point-wise technology, such as hot-wire/hot-film/hot-sphere anemometry (HWA/HFA/HAS), ultrasonic anemometry (UA) and laser Doppler anemometry (LDA), has been applied widely in previous experiments. However, these measurement methods only gather point information, and the measurement tools are usually intrusive, which may disturb the local airflow. Global-wise technology, including Particle Image Velocimetry (PIV) and Particle Tracking Velocimetry (PTV), overcomes the shortcomings of point-wise technology, and has been applied more and more recent years. PIV technology, because of well-developed technologies and available commercial systems, has been the most widely used optical velocimetry method for indoor airflow measurement [14]. However, typical PIV technology usually yield two-dimensional vector fields instead of three-dimensional, despite its high spatial and temporal resolution, due to the limitations of illumination and particle tracers. Compared to PIV technology, PTV technology can overcome these shortcomings, and can generate trajectories, which is useful to understand the characteristics of indoor airflow better. Therefore, PTV technology gradually becomes a powerful tool for indoor airflow measurement.

Although 3D PTV technology has been developed and applied for indoor airflow measurement in previous studies, the research mainly focused on the developments and verifications of independent measurement algorithms. There is no comprehensive research, especially on the performance evaluation. Therefore, this thesis firstly conducts a comprehensive research on 3D PTV technology, from the aspects of literature survey, and of performance evaluation. Then 3D PTV technology is employed as the main measurement tool to conduct an experimental investigation of indoor airflow under the condition of mixing ventilation. In contrast to displacement ventilation, mixing ventilation does not rely on the presence of internal heat sources to ventilate the room and can therefore be used in, but not limited to, (nearly) isothermal cases. Besides, mixing ventilation can be characterized by relatively uniform distributions [15, 16]. Our investigation also generates a three-dimensional experimental benchmark on mixing ventilation.

Section 1 gives a detailed review about 3D PTV technology and previous applications in indoor airflow field. Typical PTV technology for indoor airflow fields, including equipments and methods, is introduced in this part. Then previous relevant applications are summarized. Eventually, the limitations and future developments of 3D PTV are discussed.

Section 2 compares the performances of 3D PTV measurement algorithms and typical PIV measurement algorithms using simulation and experimental method. Especially, the tracking density index, which reflects the tracking difficulty, is used as the evaluation factor.

Section 3 evaluates the performances of seven complete 3D PTV measurement algorithms using simulation and experimental method. Tracking density and tracked frames are selected as the evaluation factors. Through this section, an optimal 3D PTV measurement algorithm and procedure can be decided, and then later is applied in the section 4 to conduct experimental investigation.

Section 4 conducts an experimental investigation on indoor airflow with the condition of mixing ventilation using an optimal 3D PTV technology. The experimental results are three

dimensional, which is useful for understanding the characteristics of indoor airflow. Based on the experimental results, some analysis is carried out, aimed at generating three-dimensional benchmarks for CFD simulation in the future.

1 Revue du suivi Lagrangien de particules pour l'étude des écoulements d'air intérieur

Résumé en français

La mesure expérimentale tient un rôle important dans l'étude des mouvements d'air intérieur, d'où le développement et l'utilisation de nombreuses méthodes de mesure à cette fin. Selon le principe de mesure, ces méthodes peuvent être divisées en deux groupes, les techniques de mesure Eulériennes et les techniques de mesure Lagrangiennes.

Pour les techniques de mesure Eulériennes, telles que les sondes fil/film/sphère chaude, l'Anémométrie à Ultrasons (UA), l'Anémométrie Laser Doppler (LDA) et la Vélocimétrie par Images de Particules (PIV), la vitesse du fluide v est une fonction de la position x et du temps t , comme indique l'Eq.(1-1).

$$\vec{v} = \frac{d \vec{x}}{dT} \quad (1-1)$$

Pour les techniques de mesures lagrangiennes, comme la vélocimétrie par traces de particules (Particle Streak Velocimetry, PSV) et la vélocimétrie par suivi de particules (Particle Tracking Velocimetry, PTV), la vitesse du fluide est le résultat de l'Eq. (1-2), par le suivi de chaque particule dans le temps, et les trajectoires des particules individuelles sont générées.

$$\vec{v}(x(T), T) = \frac{d \vec{x}}{dT} \quad (1-2)$$

Parmi ces méthodes de mesure, les technologies PIV, PSV et PTV sont également considérées comme étant globales. Avec l'utilisation de la technologie optique et des traceurs de particules, on peut obtenir l'information globale des champs d'écoulements d'air l'intérieur, plutôt que des informations locales. Les outils de mesure ne sont pas intrusifs, par conséquent, le champ d'écoulement d'air local ne sera pas perturbé. Ces dernières années, les technologies PIV, PSV et PTV ont été appliquées de plus en plus fréquemment dans l'étude d'écoulement d'air intérieur, et en particulier la technologie PIV, de nombreux systèmes commerciaux sont désormais disponibles et des logiciels analytiques ont été développés. Cependant, les systèmes typiques de PIV peuvent seulement obtenir des informations en deux dimensions dans un plan, ou alors, à petite échelle, des informations à trois dimensions, en raison des limitations du système d'éclairage et des traceurs. Ceci peut être un inconvénient pour la mesure d'air intérieur dans les bâtiments. Par rapport à la technologie de PIV, la technologie PTV surmonte ces défauts, et donc progressivement adoptée comme méthode de mesure pour l'étude de l'air intérieur.

Dans cette thèse, la technologie PTV est utilisée pour étudier les caractéristiques des champs d'écoulement d'air intérieur. Afin de mieux utiliser la technologie PTV, dans ce chapitre, un résumé détaillé de la technologie PTV pour les champs d'écoulement d'air

intérieur est présenté. Tout d'abord, les équipements et les méthodes de la PTV pour les applications d'écoulement d'air intérieur sont introduits avec soin, ceci en quatre parties: le système d'éclairage, les traceurs (particules), le système d'enregistrement d'images et l'algorithme de suivi. Ensuite, les principales applications antérieures de la technologie PTV pour la mesure des champs d'écoulement d'air intérieur seront résumées. Enfin, les limites et les perspectives de la technologie PTV pour les champs d'écoulement d'air intérieur seront discutées. Par ailleurs, la technologie PSV et ses principales applications antérieures pour la mesure des champs d'écoulement d'air intérieur sont également résumées.

Ce chapitre montre, en particulier pour les écoulements turbulents, que la façon dont les informations quantitatives et détaillées sont obtenues par PTV est critique pour l'analyse des propriétés de turbulence et le développement de simulations numériques. De plus, ce chapitre indique qu'il n'y a pour l'instant pas de systèmes PTV universellement applicables. Par conséquent, de nombreuses hypothèses et des compromis doivent être faits, afin de satisfaire les besoins de la recherche. Enfin, ce chapitre suggère à l'utilisateur qu'une procédure conviviale de mesure PTV et des algorithmes de suivi rapides sont importants pour le développement de la technologie PTV et son application dans le futur.

Ce chapitre est basé sur l'article de revue:

Sijie Fu, Pascal Henry Biwole, Christian Mathis. Particle Tracking Velocimetry for indoor airflow fields: A review. *Building and Environment* 87: 34-44.

Particle Tracking Velocimetry for indoor airflow fields: A review

Sijie Fu, Pascal Henry Biwole, Christian Mathis, 2015. *Building and Environment* 87: 34-44.

Abstract

Airflow field measurement plays a significant role in creating a thermally comfortable indoor environment, by providing adequate quantitative information of indoor air distribution and local air velocity. In recent years, the Particle Tracking Velocimetry (PTV) technique has gradually become a promising and powerful tool for indoor airflow field measurement. This paper firstly gives an overview of the equipments and methods involved in typical PTV applications to indoor environments, and then introduces related applications of PTV for measuring indoor airflow fields. The Particle Streak Velocimetry (PSV) technique for indoor airflow measurement is also introduced. This paper shows how the quantitative and detailed turbulent flow information obtained by PTV measurement is critical for analyzing turbulent properties and developing numerical simulations. The limitations and future developments of PTV and PSV techniques are also discussed.

Keywords: Particle Tracking Velocimetry (PTV), indoor airflow, measurement, Particle Streak Velocimetry (PSV)

1. Introduction

Ventilation and air distribution systems, as a main part of Heating, Ventilation and Air Conditioning (HVAC) systems in modern buildings, have received increased attention in recent years [17-26]. The performance of ventilation and air distribution systems not only influences the indoor air quality directly [9, 10], but also strongly affects the total energy consumptions in buildings [8]. Among the evaluations indices referring to ventilation and air distribution systems, there are airflow patterns (such as trajectory, impingement, separation, circulation, reattachment, buoyancy, vortices etc) and airflow field (temperature, velocity and pressure). Numerical simulation using Computational Fluid Dynamics (CFD) models is the most prevalent research method now, and it accounts for about 70% of studies dealing with the performance of ventilation and air distribution system in buildings [11]. Yet, it is still not possible to predict the structure of indoor airflows with the distinct characteristics of low speed turbulence and three-dimensionality accurately using current computer technology [12]. Therefore, experimental measurements are still a fundamental and important step in the indoor airflow studies, and high quality experimental data plays a key role in the validation and development of numerical models. Besides, the local airflow fields around devices in ventilated rooms, such as heat sources, are still poorly known [27] and experimental data is one of the best ways to understand them.

Because the indoor airflow is usually large-scale, three dimensional, turbulent and unsteady, it is not an easy task to measure it accurately. The most common modern measurement methods for indoor airflow have been summarized by Sun and Zhang [13]. Generally, the measurement methods are categorized into “point-wise” and “globe-wise”. The point-wise techniques usually refer to measurement methods that gather only one-point velocity information, such as hot-wire/hot-film/hot-sphere anemometry, which also intrusively disturbs the local airflow, ultrasonic anemometry (UA), and laser Doppler anemometry (LDA). Therefore, they are not the best choice for indoor airflow measurement. Globe-wise techniques usually refer to optical velocimetry and are regarded as an effective alternative tool for measuring indoor airflow distributions. Optical velocimetry can obtain the velocities and related statistical information in a global domain without disturbing the airflows. Particle Image Velocimetry (PIV), Particle Streak Velocimetry (PSV) and Particle Tracking Velocimetry (PTV) are the most prevalent methods among the globe-wise techniques. They have been applied for indoor airflow measurement more and more in recent years.

The PIV is regarded as the most widely used optical velocimetry method for indoor airflow measurement with well-developed technologies, rich experimental literature and available commercial systems. Cao et al. summarized and discussed the PIV technologies and applications for indoor airflow measurement during the past decade [14]. However, typical PIV can only yield two-dimensional vector fields instead of three-dimensional, despite its high spatial and temporal resolution. PSV and PTV are both capable of obtaining velocity vector and air trajectories from one dimension to three dimensions and allow a direct observation of the airflow.

The PTV is a powerful tool to study both indoor air quality and thermal comfort, since the

neutrally buoyant tracers used show the displacement of airborne pollutants, and air velocity vectors are measured. This study aims to provide a review of the PTV for indoor airflow measurement, its key components and related research applications. This paper only reviews published PTV methods used by researchers for indoor air applications. The information on hardware, algorithms and results for PTV in liquids, though instructive and sometimes similar, is not considered by this paper. The use of the PSV technique for indoor airflow study is also reviewed. Last, the advantages, limitations and future application of PTV and PSV techniques for indoor airflow measurement are discussed.

2. PTV equipments and methods for indoor applications

The term “Particle Tracking Velocimetry” (PTV) was first introduced in the literature in 1980[28]. During the past 30 years, the PTV technique has been widely applied to investigate small-scale flows [29-34], but now it is also gradually being used for the measurement of large-scale flows, especially in indoor airflow studies. The measurement principle and major developments of PTV have been reviewed in previous excellent scientific literatures [35-37], thus we will only present the PTV technologies focusing on the application in large-scale indoor airflows.

Regarded as a Lagrangian measurement method, PTV determines particle trajectories and velocities through capturing and analyzing each particle image to locate the particles’ centers and connecting image tracks. Similar to a PIV system, a PTV system generally consists of four main parts: illumination system, image recording devices, tracer particles and image evaluation methods (algorithms). Figure 1-1 illustrates a basic 3D PTV system for large scale measurement. There is still no available commercial PTV system for indoor airflow measurement. Several representative PTV systems for indoor airflow measurement as well as their applications will be summarized in the following sections.

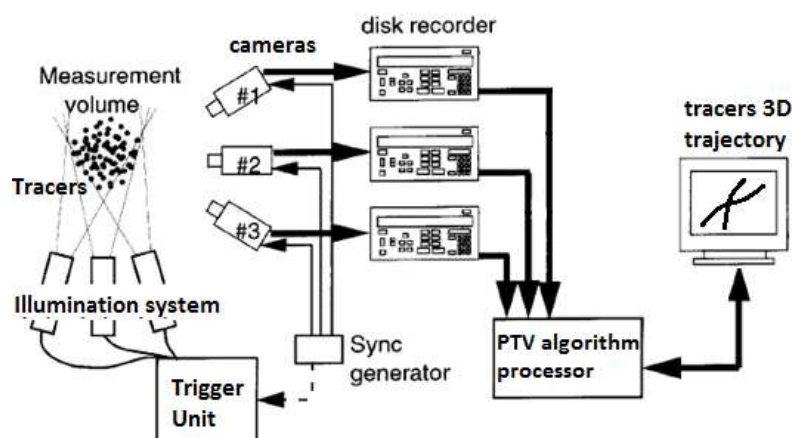


Figure 1-1: Basic layout of 3D PTV for large-scale measurement

2.1 Illumination system

In indoor airflow measurements using the PIV technique, a double-pulsed Nd:Yag laser system with an articulated delivery arm to generate a green light sheet of 532 nm wavelength is the most widely used illumination system. The laser is also the most universal light source in traditional small-scale PTV measurements [29, 38-41]. However, this light source is unpractical in large-scale measurement volumes with PTV technique, because the low energy of the laser hardly satisfies the illumination needs. Jones et al. estimated that a 10W laser could only illuminate an area of the order of 1 m² [42]. Thus if the laser is used as the light source in a large-scale measurement volume, the power of the laser needs to be huge. It is almost impossible to handle such a laser in ordinary laboratories. Besides, when the thickness of the laser beam expands, the energy density of the laser will also decrease rapidly.

For these reasons, it is more practical to adopt conventional light sources when using the PTV technique for measurements in large volumes. The most generally adopted conventional light sources can be divided into two categories, one that generates light pulses, such as photographic flash lamps, and the other that uses steady state illuminations, such as halogen lamps and arc lamps. For example, a BalcarQuadlite halogen is shown in Figure 1-2. These light sources have been applied in the PTV systems for indoor airflow measurement to ensure taking a good quality of image [43-47]. The main drawback in using photographic lamps or strobe light is the rapid decrease in light intensity as the frequency increases. Thus, the frequency of the flash is generally limited to 2 or 3 Hz [47]. This limitation implies that only slow moving flows can be measured. Another limitation is the difficulty to synchronize the flash with the cameras.

It should also be noticed that both pulsed and continuous light sources usually generate a lot of heat so that the indoor airflows may be disturbed. Thus in practice, they are only turned on for a few seconds when the cameras are recording, or they are staged outside the test area behind a glazed panel. In this regard, the use of last generation high power light emitting diodes (LED) could be a promising way to provide light for PTV due to their higher luminous efficacy and their lower heat dissipation compared to traditional illumination devices. LED has been successfully used recently for 3D PTV [48, 49].



Figure 1-2: Front view of a BalcarQuadlite halogen lamp used for 3D PTV [45]

2.2 Tracer particles

Tracer particles affect the quality of indoor PTV measurements directly, since PTV actually measures the velocity and trajectory of flow driven tracer particles instead of the airflow itself. The choice of the tracers is crucial for the reliability of the measurement. That choice is usually a compromise among the considerations of neutral density with respect to the fluid, size and lifetime that suits the phenomenon to be measured, light scattering capability which should be sufficient for image taking.

In this regard, the scattering cross section C_s is used to evaluate the scattering behavior of the particles. C_s is a function of the ratio of the particle diameter d_p to the light wavelength λ for spherical particles. Melling [50] compared the approximate C_s for particles with different diameters, and found that the larger the particles the stronger the scattering behavior.

Tracers of diameter less than $1\mu\text{m}$ used in small-scale PIV and PTV cannot be used in large-scale PTV since they are too tiny to scatter enough light and to be singled out and tracked individually. Helium-Filled Soap Bubbles (HFSBs) are the most widely used tracer particles in large-scale airflow measurement. The underlying principle is to inflate a liquid film with a lighter-than-air gas to compensate for the weight of the membrane. HFSBs have good characteristics of neutral density, short relaxation time, high light scattering efficiency, relative suitable size ranging from 1 to 4mm, as well as relative suitable lifetime [51-56]. A picture of a HFSB can be seen on Figure 1-3.



Figure 1-3: Single helium filled soap bubble. Light scattered on the shell can be seen. [54]

A bubble generator nozzle with three concentric tubes is usually used to generate HFSBs, one tube for helium, one for air and the last one for the bubble fluid. The flow rate in each tube is usually controlled separately and determines the bubble's diameter. There are two different types of nozzle used for the generation of bubble fluid [57], one is the Pitot tube type which is the more ancient and still the most used one, and the other is the Orifice type nozzle, which can generate more bubbles per second. A sketch of the Orifice type nozzle and a three-channel generator is illustrated in Figure 1-4. More details regarding the bubble generation can be found in Bosbach et al. [56].

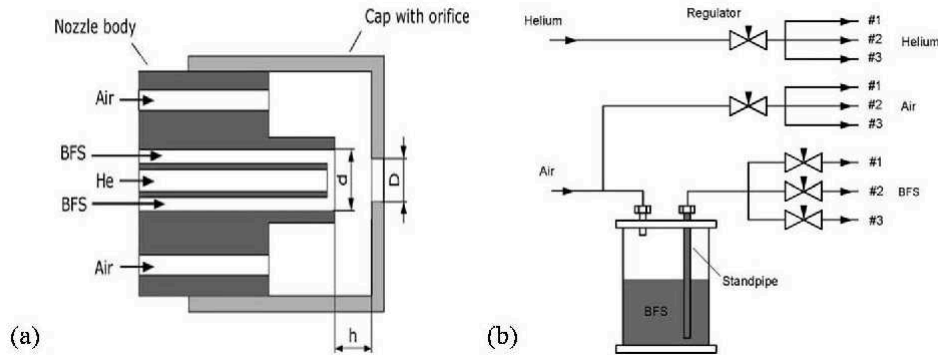


Figure 1-4: Sketch used for generation of neutrally buoyant helium filled soap bubbles: (a) the Orifice type nozzle; (b) the three-channel generator. [56]

From a theoretical viewpoint, a general equation of motion for a single rigid sphere in the non-uniform flow was given by Maxey and Riley [58]. Based on Maxey and Riley’s equation, Kehro and Bragg [59] conducted a complete study of the HFSB physics and showed that a neutral particle reliably follows the flow, provided the changes of properties of the flow are negligible with respect to its diameter. Some experimental and numerical studies were done to compare the effects of different bubble diameters and shell thicknesses on the ratio of fluid density to bubble density. [29, 59] (see Figure 1-5).

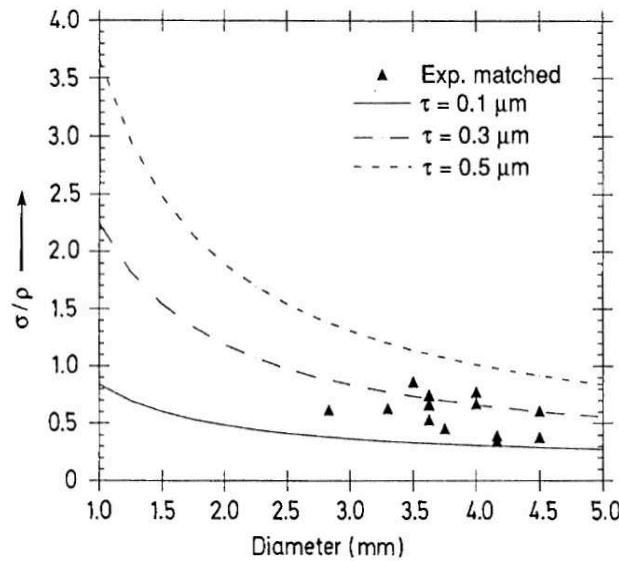


Figure 1-5: Influence of bubble diameter and film thickness τ on density ratio of HFSBs. [59]

In addition, if the external forces (gravitational, centrifugal and electrostatic) can be considered negligible and the particles have approximately spherical shape, an equation satisfying most flows can be found in Melling [50].

When the Reynolds number (Re) is low, Stokes’ drag law (Eq.1-3) is considered to apply to evaluate the tracking behavior of particles [50]. In the equation, where g is the gravitational acceleration, ρ_p and ρ_f are the density of the particles and the fluid respectively, μ is the dynamic viscosity of the fluid, and d_p is the diameter of the particles. However, it is noticeable that the Stokes’ drag law may underestimate the actual velocity lag when the airflow has a

high turbulence level.

$$u_g = d_p^2 \frac{(\rho_p - \rho_f)}{18\mu} g \quad (1-3)$$

The Stokes number (St) is also used to evaluate the tracking behavior of particles. St is the ratio of the particle response time τ_p to the time scale τ_f of the airflow. The Stokes number can be estimated as follows [60]:

$$St = \frac{2}{9} \frac{\rho_p}{\rho_f} \left(\frac{a}{L} \right)^2 \cdot Re \quad (1-4)$$

where a is the particle radius, L is the characteristic flow length scale and Re the Reynolds number of the flow. The recommended St of tracer particles for airflow is less than 0.1[14], which is the case for HFSBs used in slow motion room airflow.

Recently, helium-filled latex balloons (HFLBs) with a diameter of about 150 mm were used as tracer particles in a large measurement volume to investigate natural convection [47, 61]. The tracking behavior of the particles was evaluated using Stokes number, and the St was between 0.02 and 0.2. More detailed analyses of HFLBs can be found in [47, 61].

2.3 Image recording devices

The maximum frame rate and the camera resolution are the two main factors when choosing image recording devices. The frame rate is chosen based on the maximum airflow velocity so that the particle displacement is less than a quarter of the size of research windows; the rule is as the following equation:

$$\Delta t \leq \frac{\Delta d_{\max}}{V_{\max}} = \frac{L}{4 V_{\max}} \cdot d_{\max} = \sqrt{d_x^2 + d_y^2} \quad (1-5)$$

where d_x and d_y are the pixel coordinates of the displacement on the image plane, and L is the pixel size of the research window. Besides, it is helpful to minimize tracking ambiguities by increasing the frame rate as the particle seeding density increases. Therefore, the frame rate should usually be decided so that the maximum displacement of a particle is smaller than the minimum distance between two particles. In practice, frame rates up to 100 fps are usually sufficient to study the indoor airflows away from walls and ventilation inlets.

The size of the particles used, the size of the field visualized, the illumination employed and the background determine the choice of the camera resolution. The general rule is that the particles must be seen clearly. Agui and Jimenez gave the field of observation of a sensor as following [62]:

$$\text{Field of observation} = \text{Surface of the detector} / M \quad (1-6)$$

where M is the enlargement of the optical system. Eq. (1-7) gives the diameter of a particle on the digital image.

$$d = (M^2 d_p^2 + d_d^2 + d_r^2)^{1/2} \quad (1-7)$$

where d_p is the real diameter of the particle, d_r is the size of pixel or grain in the case of a photographic film, and d_d is the minimal diameter due to the refraction. d_d is given by Adrian as

follows [39]:

$$d_d = 2.44 \cdot NO \cdot \lambda \cdot (1 + M) \quad (1-8)$$

where NO is the aperture of the lens and λ is the wavelength of the light used. The observable depth of field δ_z where particles are seen accurately is also given by Adrian as follows:

$$\delta_z = 4 \cdot NO^2 \cdot \lambda \cdot \left(1 + \frac{1}{M}\right)^2 \quad (1-9)$$

Besides, it is preferable to choose the sensors featuring a high number of gray levels under the condition of poor contrast with the background or very large light sheet. It is noticeable that a large size pixel could offer a better sensitivity but a poorer resolution than a smaller size pixel.

Coupled charged devices (CCD) cameras are the most common image recording devices used in PTV systems for indoor airflow measurement. CCD cameras usually have increased spatial resolution, convenient data transmission and image processing, minimum exposure time, high light sensitivity as well as low background noise. Normally, CCD camera with 8 to 10 bits sensor rate is sufficient for most PTV measurements. More and more complementary metal oxide semiconductor (CMOS) cameras have been employed in PTV systems recently [27, 48]. Compared to CCD cameras, they allow recording speeds in the range of a few kHz with acceptable noise levels. A detailed comparison between CCD cameras and CMOS cameras can be found in Hain et al. [63]. Given the small size of the tracers relative to the size of the measuring volumes, most research teams use cameras with pixel resolution equal to or higher than 4 megapixels.

Due to the size of the measuring volumes and the relatively short distance from cameras to the latter, wide-angle lenses from 22mm down to 15mm are usually used for indoor PTV. Lenses with focal length from 24mm to 15mm [27] or even less can be used. The resulting image distortion is usually compensated for after the camera calibration procedure.

2.4 Tracking algorithms

The procedure to obtain particle trajectories from raw particle images can be divided into five main steps: namely multi-camera calibration, image processing, particle center detection, 2D or 3D tracking and 3D reconstruction. A detailed review of usual tracking algorithms can be found in Ouellette et al. [64]. Here, we will focus on the distinct features of PTV algorithms used in large airflow as reported by researchers of this topic.

2.4.1 Multi-camera calibration

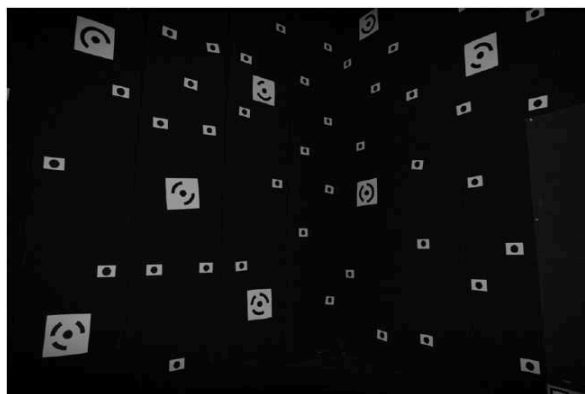
In a multi-camera system, multi-camera calibration is the way of establishing the mathematical relationship between each camera 2D pixel (image) coordinates and a physical 3D reference frame. The calibration step gives access to the cameras' intrinsic and extrinsic parameters including focal length, principal point, skew angle, distortion coefficients and rotation and translation matrices from each camera reference frame to the physical 3D reference frame. Those parameters are yielded by the minimization of the reprojection error between the

known 3D coordinates of the calibration target, and the same coordinates calculated via a mathematical camera model. The calibration algorithms employed do not differ from those used in small scale and liquid PTV. In large scale airflows, Biwole et al. [27] and Barker [49] used the calibration method proposed by Zhang [66] while Li [67] used the procedure presented by Svoboda et al. [68].

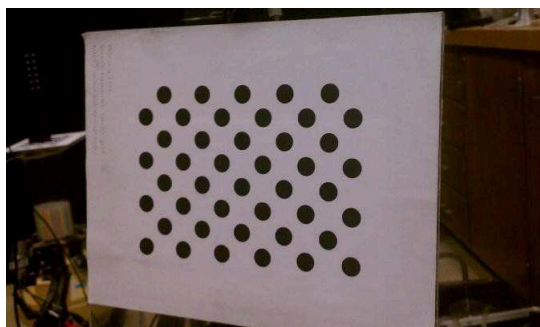
The calibration target must be big enough to allow the detection of its specific points by the cameras. The target may be a full three-dimensional object such as a cube, or a two-dimensional (planar) object such as described in Zhang [66]. In the latter case, the target must be moved so that it is viewed from different angles by each camera and the in-depth coordinate is derived from the in-plane coordinates by trihedral projection as shown on Figure 1-6(a). Biwole and Yan et al. [27, 46] used a planar checkerboard with black and white 3 cm large squares for calibration in a 3.1 m \times 3.1 m \times 2.5m test-room. The checkerboard had 14 horizontal squares and 10 vertical squares, as shown on Figure 1-6(a). A planar checkerboard composed of a 12 \times 12 array of 6 cm black and white squares was also used by Biwole et al. in a mock-up aircraft cabin [45]. Resagk et al. [69] used a large number of coded targets on the walls of a test facility with 4.2 m length, 3.0 m width and 3.6 m height, as shown on Figure 1-6(b). Barker [49] used a planar calibration board containing 44 black circles as shown on Figure 1-6(c). This pattern board seemed to give better calibration results with lower re-projection errors than the checkerboard pattern. Multi-camera calibration may be done before or after particle image acquisition.



(a) Calibration target used by Biwole et al.[27]



(b) Calibration targets used by Resagk et al.[69]



(c) Calibration target used by Barker[49]

Figure 1-6: Several calibration targets for large scale airflow measurement

2.4.2 Image processing

As in other traditional imaging techniques, the background is first averaged then removed from the seeded flow images. The image processing procedure highly depends on contrast between the illuminated particles and the background. In case of poor contrast of the background to the particle images, a high pass filter may be applied by the use of a threshold value setting to zero all pixel values lower than the threshold. Erosion by structuring elements of the form $[1, 1]$ and $[1, 1]^T$ can also be used to get rid of single-pixel noise.

A particularity of 3DPTV in large scale flows arises when helium filled bubbles get close to the recording cameras. Those bubbles can create many fake particle centers, which are out of the common view field and therefore must be removed. To do so, Biwole et al. [27] proposed an image processing procedure consisting of filling the particle by the use of structuring element before subtracting them from the original particle images.

2.4.3. Particle center detection

For particle center detection, the weighted averaging method [36, 70], is the most used with gas filled bubbles [27, 49, 51] because of its easy implementation and effectiveness. In spite of higher capabilities when handling overlapping particles, Gaussian fitting methods [71, 72] perform poorly on gas filled soap bubbles because their light intensity profile cannot always be approximated by a Gaussian function. One particle can feature two distinct peaks of intensity as

shown on Figure 1-3. Besides, Gaussian fitting methods are computationally expensive.

2.4.4. Particle tracking

There is no difference tracking schemes used for PTV in liquids and PTV in the air. The tracking strategies may be divided into two types: The first type (Figure 1-7 (a)) consists in first tracking each particle in the image domain of each camera separately through time based on the successive frames (2D tracking), and then reconstructing the 3D trajectories by spatial matching of the 2D trajectories obtained. The second type (Figure 1-7 (b)) is the inverse: Here, the particles 3D coordinates are calculated at each time step and the tracking is done directly in the object domain.

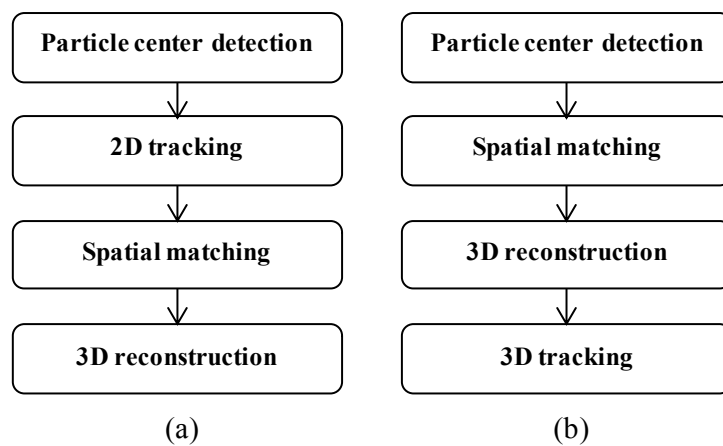


Figure 1-7: Flow chart of particle tracking strategies

The main advantage of the first type of tracking is its easy implementation since the actual tracking is done separately on each camera. However, this method is less accurate than the second for complex flow trajectories. For example, spiral trajectories may be judged unphysical in the 2D image domain while they are realistic in the 3D domain. The main drawback of the second type of algorithms is the accumulation of computational errors with time since the 3D reconstruction must be done at each time step.

Some hybrid tracking scheme using features from each type can be found in the literature [40]. For the study of indoor air, Zhao et al. [73], Sun et al. [43, 44], Yan et al. [46, 74] and Biwole et al. [27, 45] used the first type of scheme while Lobutova et al. [47, 61] and recently Barker et al. [49, 75] and Klimentew et al. [76, 77] used the second type of scheme with good results. To track particle from one time step to the next, all teams have used multi-frame tracking algorithms [37, 40] due to their capacity of tracking trajectories for a long period and their robustness against noise. Those algorithms consist in extrapolating the 2D or 3D position of the particle on the next frame based on three to five previous positions. The extrapolated position is used as a cost function that has to be minimized among different candidate particles inside a search region. Depending on the heuristic, the cost function accounts for constraints on the amplitude and direction of velocity or acceleration of the particle.

In addition, many other algorithms have been developed in the past, such as PIV-PTV

tracking, probability-match tracking as well as velocity gradient-tensor tracking [78-80]. Most of these algorithms use extrapolation methods to predict the future particle centers. Although they perform well in the condition when the particle positions are detected precisely, their performance drops significantly with the increase of input noise [64]. Li et al. developed a novel multi-frame tracking algorithm by employing a regression method instead of the extrapolation method to process the noisy data. Their regression method used up to five previous particle positions to create trajectories [81]. Biwole et al. proposed a method combining traditional PIV fast-normalized cross-correlation to account for particle shape and light intensity, and Lagrangian extrapolation based on up to three previous positions to account for particle history [45].

For 3D reconstruction, the epipolar constraint has become a standard and well known method [36]. Biwole [45] proposed another method based on the comparison of particles 3D coordinates calculated by two cameras at a time in a three-camera system. His method allowed avoiding the explicit calculation of the fundamental matrix used in the epipolar constraint method and permitted spatial correspondence of particle from the first frame. Yan developed a hybrid spatial matching strategy which improved the detecting rate and increased detectable volumes [46].

2.4.5. Tracking accuracy assessment methods

Apart from errors due to particle weight neutrality, errors in 3D PTV mainly come from the error in the determination of calibration parameters and errors in the tracking algorithms internal design. The following methods have been used to evaluate the tracking accuracy of PTV methods for indoor air:

- The distance between a known trajectory and the reconstructed trajectory: Lobutova [47] gave a precise trajectory to a single glass sphere by the use of a stepper motor with a preset angular velocity. Biwole [45] used a single table tennis ball which he manually displaced on eleven precisely known locations. Barker [49] used a static object with fixed particles 3.0 mm in diameter.
- The use of direct comparison between raw and calculated trajectories by back projection: this method consists of projecting the calculated 3D trajectories onto the cameras image planes according to their calibration. The resulting 2D trajectories are then compared to the actual raw particle 2D trajectories obtained by simply adding up all particle image frames. This method allows avoiding the use of a specially designed validation apparatus. The result of such a comparison can be found in Biwole et al. [27].
- The use of synthetic particles: instead of real particles, images of synthetic particles with known 3D displacements are created based on the forward projection of their successive 3D coordinates onto each camera image plane using real camera calibration data. The calculated and synthetic trajectories are then compared.
- The use of PIV 3D standard image data sets: Particle images and their true trajectory are given in standard image data files, such as those released by the Visualization Society of Japan [65]. Since the calibration details are also given, users can test the effectiveness of their

PTV algorithms.

The assessment parameters used are the distance between actual and calculated trajectory [38], the ratio of the number of correct 3D trajectory tracking by the total number of input 3D trajectories [37, 64], the number of 3D tracked positions which are identical to input 3D particle positions [81], and the relative difference between the known magnitude of acceleration and the measured value [49]. The value of those parameters greatly depends on the seeding density and the complexity of the measured flow but for correctly tracked particles, the error between the reconstructed and real path is generally less than the particle diameter i.e. a few millimeters [27, 47]. This is consistent with the fact that the method is based on tracking each individual particle image. A methodology to specifically assess the accuracy of PTV for near wall measurements based on synthetic particles can be found in Kähler et al. [82].

3. Applications of PTV in indoor airflow field measurements

The applications of PTV technique for indoor airflow measurements are summarized in this section. Table 1-1 lists the representative systems as well as their related applications reviewed mainly from the available international publications. This review may not be complete due to the continuous developments of PTV technique, but represents the status and trend of indoor PTV applications now.

The measurement of airflow patterns and velocities in ventilated rooms is the main application. Three research groups are well known in the field. The bio-environmental engineering (BEE) research group of the University of Illinois at Urbana-Champaign developed both a large-scale Volumetric PTV (VPTV) system [43, 44] and a large-scale Hybrid PTV (HPTV) system [46] and employed them to investigate global and local airflow issues. They obtained abundant experimental data for validating and developing CFD models [44, 46, 73, 74, 83-85]. Figure 1-8 shows an example of their measurement results using the HPTV system. Their studies suggested the PTV technique could be a practical method to help predicting indoor air distribution in large-scale spaces.

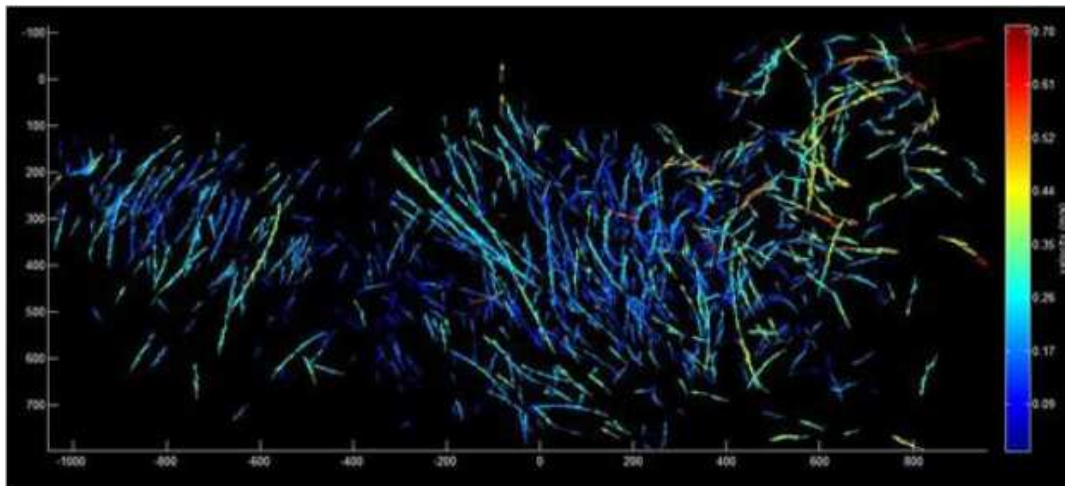


Figure 1-8: Measurement of global airflow field at a spliced plane with 100% ventilation rate by Yan, BEE group [46]

Research groups at Germany's Universities of Technology of Ilmenau, Dresden, Berlin and Aachen developed and applied a 3D PTV system to investigate convection. Lobutova et al. [47, 61] studied large-scale flow patterns in Rayleigh-Bénard convection. Their results confirmed that four different flow patterns existed in the bulk region. Probability density functions of the velocity and acceleration fluctuations were calculated from the measured data. The sketch of the experimental facility used and the 3D trajectories obtained are illustrated in Figure 1-9. Steinhoff et al. employed their redesigned 3D-PTV system to measure the structure of natural convection airflow and mixed natural and forced convection airflow [86]. Their studies also suggested 3D-PTV technique could be a powerful measurement tool for 3D and time-dependent analysis of indoor airflows.

The Research group at the Thermal Sciences Research Center of the University of Lyon built a PTV system to help validation and improvement of CFD models of air distribution in rooms. They mainly studied forced convection and natural convection over heat sources. Figure 1-10 shows the path of helium filled soap bubbles over a heater in a room [27].

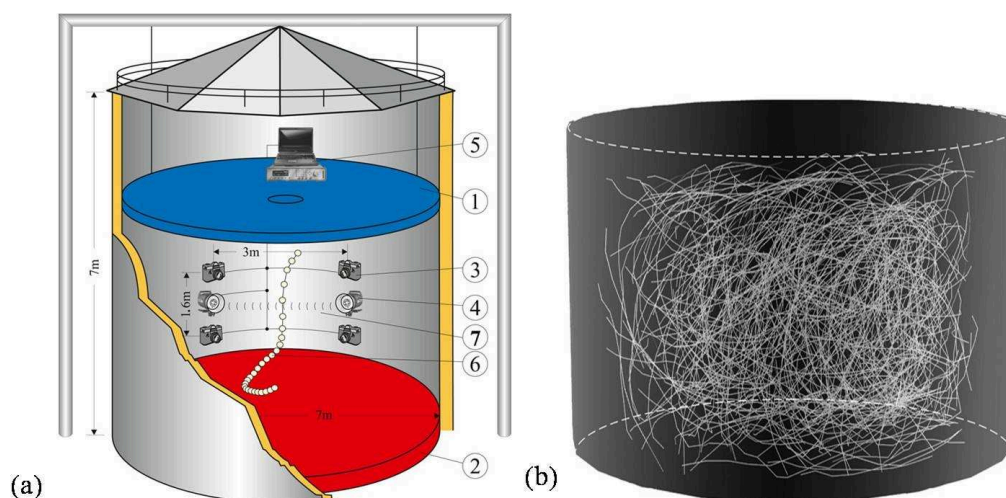


Figure 1-9: PTV measurement for natural convection using HFLBs: (a) Experimental facility; (b) 3D balloon trajectories. [47]



Figure 1-10: PTV measurement over a heater in a room [27]

Table 1-1: Summary of PTV applications for indoor airflows

Researchers	Affiliation	Illumination system	Image recording device	Tracer particles	Measurement scale (L × W × H)	Application
Resagk et al. [69,87]	TU Ilmenau & TU Berlin & TU Dresden	Halogen lamps	Four Canon EOS 20D CMOS cameras (resolution: 3504 × 2336 pixels, 5 fps set)	HFSBs, 3mm	4.2m × 3.0m × 3.6m	Visualization of large-scale forced airflow structure
Biwole et al. [27,45]	Univ. of Lyon & Univ. of Illinois at Urbana-Champaign	Six BalcarQuadrlite halogen lamps (power: 1000W each)	Three Dalsa 4M60 CMOS cameras (4 Megapixels, resolution: 2352 × 1728 pixels, 15mm Canon lens for each camera, 100 fps set)	HFSBs, 1.2-3mm	3.1m × 3.1m × 2.5m	Measurement of air velocity distributions under different measured conditions
		Six spotlights (power: 500W each)	Three TMC-1402 CL CCD cameras (resolution: 1392 × 1040 pixels, 12mm Edmund lens for each camera, 30 fps set)		5.5m × 3.7m × 2.4m	

		Eight incandescent spotlights (power: 120W each), and two copper lights (power: 500W each)	Three TMC-1402 CL CCD cameras (resolution: 1392 × 1040 pixels, 12mm Edmund lens for each camera, 30/15 fps set)		4m × 3m × 2m	
Sun et al. [43,44, 74,83-85]	Univ. of Illinois at Urbana-Champaign & NIOSH	Sixteen projector lamps (power: 300W each) Thirty-six incandescent spotlights (power: 120W each)	Two digital cameras (resolution: 3072 × 2048 pixels)	HFSBs, 1.2-3 mm	5.5m × 3.7m × 2.4m 4.7m × 4.3m × 2.1m	Measurement of airflow patterns and distributions in ventilated rooms as well as validation of CFD models
Yan [46]	Univ. of Illinois at Urbana-Champaign	Thirty-six incandescent spotlights (power: 120W each), and two copper lightings (power: 500W each)	Three TMC-1402 CL CCD cameras (resolution: 1392 × 1040 pixels, 12mm Edmund lens for each camera, 30fps set)	HFSBs, 1.2-3mm	4.4m × 4.2m × 2m	Measurement of global and local flow filed in a full-scale aircraft cabin mock-up
Barker [49, 75]	Univ. of Illinois at Urbana-Champaign	Light panels (FancierStudio) containing 500	Six motion capture cameras (Optitrack Model	HFSBs, 1.2-3mm	3m × 3m × 6m	Measurement of velocity, Reynolds stress,

		LED each. Power: 50W each.	V120: SLIM, resolution: 640 × 480 pixels, 120 fps, embedded with FPGA, 2.8-8 mm focal length, Tamron lens each)			and turbulent kinetic energy in an unconfined round turbulent air jet and an unconfined forced vortex
Lobutova et al. [47,61]	TU Ilmenau & RWTH Aachen Univ. & Audi Co.	Two Elinchrom high-power flash lamps, 3Hz	Four CANON EOS 20D SLR CMOS cameras (8 megapixels, CANON EFS 10–22 mmf/3.5–4.5 USM lenses, 3 fps)	HFLBs, 150 mm	7.16m × 3.58m (D × H, cylinder)	Investigation of large-scale natural convection airflow
Steinhoff et al. [48,86]	RWTH Aachen Univ. & TU Ilmenau	Twelve LED-light source (power: 1500 lpm each)	Four NeosCMOS cameras (Zeiss Distagon 25MM/F2,8 ZF2 f-mount lens, 25 fps)	HFSBs, 2mm	7.16m × 3.58m (D × H, cylinder) 5m × 4m × 3m	Investigation of natural convection and mixed (natural and forced) convection airflow

4. PSV technologies and applications for indoor airflow

The principle of the PSV technique is the capture of particle streak images by using a longer camera exposure time than for the PTV method. The set-up of a 2D PSV system is the same as atypical PIV system. The performance of PSV measurements for two-dimensional flow fields is excellent, but they perform poorly in three-dimensional fields when a narrow laser sheet is used in the systems because the streaks may be truncated [39]. Therefore, thick light sheet has been tested for three-dimensional airflow measurements in large volumes.

A brief summary of 3D-PSV measurement for indoor airflow is listed in Table 1-2. Scholzen and Moser developed a 3D PSV system with a 120mm thick white light sheet, and tracked particles in a 2.4 m × 1.7 m × 1.2 m ventilated space. Although good results were obtained, the depth of the tracked field was limited to 12 cm [88]. Machacek reported a 3D large-scale PSV system for wind tunnels. Halogen spot lamps were applied in the system, and three velocity components could be measured in a volume of about 1.5 m³ large. However, the spatial resolution was insufficient due to the low particle seeding density affected by the crossing of particle path segments [51]. Sun and Zhang employed a PSV system with a special designed algorithm to measure the airflow field in a 5.5m × 2.4m × 3.7m test room. Although their method gave acceptable results, the depth of the tracked area was only 6.5cm and many particle streaks were bowed [89]. Rosenstiel and Grigat developed a new segmentation method for large-scale PSV systems. Local image statics combined with classic edge detection and removal of the scene background was considered, thus allowing a good noise removal system. An algorithm for solving the classification problem of binarized stark segments was also proposed, and a comparison to previous existing PSV systems [90] showed better results [91]. The extracted vector fields from recorded streak images in a full-scale aircraft cabin mock-up are illustrated in Figure 1-11. Recently, some researchers have used the PSV technique to study the air motion around the human body and its interactions with the room ventilation [92]. They found that convective heat transfer coefficients around the body strongly increase with falling room temperature, while radiative heat transfer coefficients decrease.

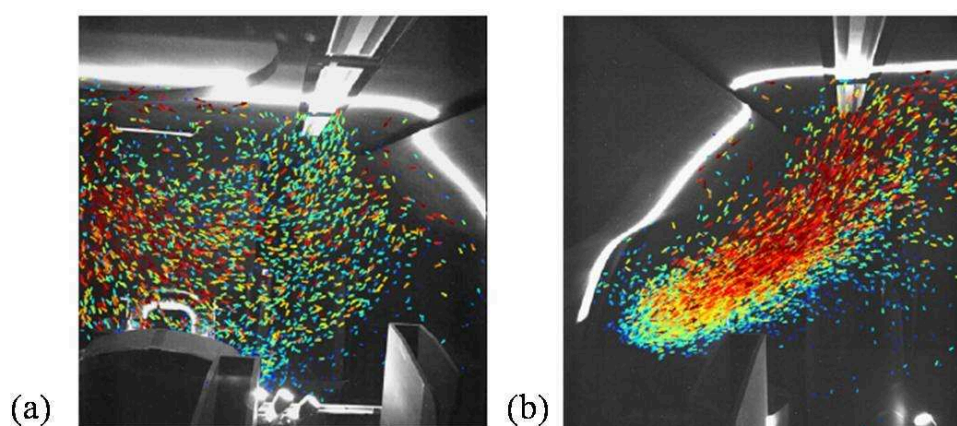


Figure 1-11: Velocity field extracted recorded in a full-scale aircraft cabin mock-up: (a) from 2525 streaks; (b) from 4476 streaks. [91]

Table 1-2: Brief summary of PSV systems for indoor airflows

Researchers	Affiliation	Illumination system	Image recording device	Tracer particles	Measurement scale
Scholzen and Moser [88]	ETH-Zürich	120mm white light sheet (several air-cooled 400W arc lamps)	Three synchronous photographic cameras	HFSBs	2.4m × 1.7m × 1.2m
Machacek [54]	ETH-Zürich	Halogene spot lamps (power: 2000W, 1000W, 120W)	Two Pulnix TM6710 CCD cameras (resolution: 640 × 480 pixels, 8mm Schneider Kreuznach lens, 120fps)	HFSBs	4m × 3m × 2m
Sun and Zhang [89]	Univ. of Illinois at Urbana-Champaign	Details not given	Two digital cameras (resolution: 3072 × 2048 pixels)	HFSBs	5.5m × 2.4m × 3.7m
Rosenstiel and Grigat [91]	TU Hamburg-Harburg	A gas-discharge lamp	Pulnix TM-1010 camera	HFSBs	Covering 4 m ²
Voelker et al [92]	Univ. of Kaiserslautern & Ed. Züblin AG	Light-emitting diodes (LED)	A high-resolution camera (21.1 megapixels, 3.9fps, 24mm focal length)	HFSBs	0.7m × 1 m

5. Limitations and future developments

The limitations and needed future developments of PTV and PSV techniques for indoor airflow applications are concerned both with the equipment and the methods.

5.1 Equipment

The powerful light sources employed in large scale PTV and PSV applications interact with the flow through convection and radiation heat transfers. As mentioned in section 2.1, the design and generalization of high light power, low heat generation light sources such as LED should help decrease this unwanted effect.

Regarding the tracer particles, the main limitation of HFLBs and HFLBs arises from the fact that the size of tracers should be smaller than the smallest characteristic length of the studied phenomena. Therefore, those tracers cannot be used to study boundary layer flows. It is also difficult to use them in strongly turbulent flows since their size is usually bigger than the Kolmogorov length scales (the smallest scales in the spectrum that form the viscous sub-layer range). Another limitation arises from the lifetime and generation rate of tracer particles produced by current commercial generators, which are respectively limited to about two minutes and 300 particles per second [93]. The design of longer lasting particles and higher generation rate generators is critical to track longer air trajectories and to increase the spatial resolution of the measurement. Such a task has already been successfully tackled by some research teams [56].

Regarding recording devices, the development and use of cameras with ever higher pixel resolution along with faster data processing systems to avoid bottlenecks should help detect more particles in the measured flow and increase the seeding densities.

5.2. Methods

The PTV technique usually results in complex and time consuming tracking algorithms. The computation of a few tens of images with a few thousand of particles requires several hours on a desktop computer. To solve this problem, real-time 3D PTV is being researched. Among the most promising solutions to reduce the processing time is the parallel-processing framework. Employing these methods, a 100 to 200-fold speedup has already been reported by various researchers [75, 94, 95]. The authors believe that this excessive data processing time along with the experimental expertise needed for multi-camera calibration are the main causes limiting the development of commercial PTV systems.

The future development of PTV algorithms should also be aimed at increasing the number of particles that can be tracked. Mainly because of overlapping particle image issues, the seeding density is currently limited to around two thousand particles in most indoor air applications. This limitation seriously reduces the spatial resolution of the method.

In order to cope with the large dynamical range in room airflow i.e. when the velocity

difference between inlets and the central space is important, hybrid PSV-PTV algorithms have to be developed, with PSV working on high velocity areas and PTV working on low velocity areas. Such hybrid algorithms have already started being investigated [46].

Another foreseeable application is the development of multi-PTV systems for larger rooms such as atriums or conference rooms. More than the challenges in terms of multi-camera calibration and time synchronization, the major issue is to individually track thousands of tiny particles from one 3D PTV field to the next one. In this regard, the most obvious tag would be each particle's 3D coordinates.

Last, it is also noticeable that the PTV technique is not always the optimum option for indoor airflow studies. Near the inlets and outlets where the inlet air velocity is high or close to the walls, laser Doppler velocimetry or hot wire velocimetry, are usually better choices to yield turbulence statistics.

6. Conclusion

The key technologies composing a typical PTV system for indoor airflow applications were introduced and discussed. It was noted that no universally applicable PTV system has been found, as many assumptions and compromises had to be made in practical applications in order to satisfy the particular research needs. PSV systems for indoor airflow measurement were also briefly reviewed.

The reviewed publications show that the PTV technique has gradually become a powerful tool for indoor airflow measurement, but the range of applications is still very limited, mainly concentrating on full-scale model measurements. Very few studies on sub-scale residence environment were found, showing that there is still a lot to be gained from the use of the technique for indoor airflow study.

The validation and development of CFD numerical models for indoor environment prediction need to be supported by high quality experimental data. Although the PIV technique has been widely adopted to obtain experimental data for validating numerical models [96-99], it usually only measures the airflow velocity fields inside the laser sheet, and therefore, the numerical models cannot be validated for a fully three-dimensional flow. The PTV technique, as a powerful 3D measurement tool, obtains more complete experimental data to validate and develop numerical models from a holistic point of view. Further, information on the flow structures and airborne pollutant dispersion characteristics can be extracted directly from the data. The development of user friendly 3D PTV procedures with faster tracking algorithms is a key step toward the emergence of commercial systems.

Acknowledgements

This work was supported by a funding from the French National Research Agency (ANR) through the FLUBAT project (ANR-12-VBDU-0010). The authors would like to thank the Agency and all the members of the project for their support. The authors would also like to

acknowledge the financial support for this work through the grant “Bourse Doctorale Régionale-Volet DAS” from the Région Provence-Alpes-Côte d'Azur, France.

2 Comparaison numérique et expérimentale de la précision et de l'exactitude de la vélocimétrie 3D par suivi de particules (PTV) et de la vélocimétrie par images de particules (PIV) pour l'étude des écoulements d'air intérieur

Résumé en français

Les technologies PTV et PIV, qui présentent l'avantage de fournir une information globale, ont été de plus en plus appliquées à l'étude des écoulements de l'air intérieur. Pour établir une comparaison entre différentes technologies de mesure, la précision et l'exactitude des mesure est toujours un point crucial, il est donc important d'évaluer l'exactitude et la précision des méthodes PIV et PTV. Bien qu'il existe de nombreuses évaluations d'exactitude et de précision pour les technologies PTV et PIV, dans les études précédentes, la densité de suivi, définie comme le rapport de l'espacement moyen entre particules sur le déplacement moyen des particules, a été rarement considérée. Par conséquent, dans ce chapitre, les performances de chaque technique sont évaluées en considérant la densité de suivi. Puisqu'un objectif de cette thèse est d'étudier les caractéristiques des écoulements d'air l'intérieur en utilisant la technologie PTV, et que, généralement, des paires d'images sont utilisées pour évaluer la performance de la mesure PIV, dans ce chapitre, l'algorithme de corrélation croisée typique pour la 2D PIV, et l'algorithme de corrélation croisée modifiée pour la 3D PTV, cf. l'Eq. (2-1), sont sélectionnés pour représenter la technologie 2D PIV typique et la technologie 3D PTV respectivement.

$$\gamma(u, v) = \frac{\sum_{x,y} [f(x, y) - \bar{f}_{u,v}] [t(x-u, y-v) - \bar{t}]}{\sqrt{\sum_{x,y} [f(x, y) - \bar{f}_{u,v}]^2 \sum_{x,y} [t(x-u, y-v) - \bar{t}]^2}} \quad (2-1)$$

Pour l'algorithme de la 3D PTV, deux méthodes de correspondance spatiale différentes sont employées, cf. les équations Eq. (2-2) à Eq. (2-5) ci-dessous.

$$F_{ij} = [T_i - R_i R_j^T T_j]_x R_i R_j^T \quad (2-2)$$

$$[u]_x = \begin{pmatrix} 0 & -u_k & u_j \\ u_k & 0 & -u_i \\ -u_j & u_i & 0 \end{pmatrix} \quad (2-3)$$

$$[x'_i \quad y'_i \quad 1] F_{ij} \begin{bmatrix} x'_j \\ y'_j \\ 1 \end{bmatrix} < s \quad (2-4)$$

$$\min_{i,j} (\|A_i - B_j\|) = \min_{i,j} (\sqrt{|x_a - x_b|^2 + |y_a - y_b|^2 + |z_a - z_b|^2}) \quad (2-5)$$

Ce chapitre compare tout d'abord les performances de mesure 2D PIV typique et 3D PTV

numériquement. Les résultats suggèrent que, lorsque la densité de suivi est inférieure à deux, la 3D PTV ne peut généralement pas donner des résultats de mesure fiables. Cependant, quand la densité de suivi augmente, la 3D PTV a une meilleure capacité à mesurer les déplacements que la 2D PIV. Ensuite, des résultats obtenus par 3D PTV et par 2D PIV sont comparés expérimentalement à l'aide d'un écoulement d'air à faible turbulence généré par un jet à basse vitesse. Les résultats indiquent que la différence entre PIV et PTV devient d'autant plus grande que la vitesse de l'air est réduite. Ces conclusions suggèrent que la densité de suivi a une influence directe et importante sur les mesures de la PIV typique et de la 3D PTV. Par conséquent, la pré-évaluation d'une densité de suivi appropriée peut avoir un impact significatif sur le processus de mesure.

Ce chapitre est basé sur l'article de revue:

Sijie Fu, Pascal Henry Biwolé, Christian Mathis. Numerical and experimental comparison of 3D Particle Tracking velocimetry (PTV) and Particle Image Velocimetry (PIV) accuracy for indoor airflow study. Building and Environment 100: 40-49.

Dans l'article, pour la 3D PTV, seule la méthode de correspondance spatiale par calcul et comparaison des coordonnées 3D (Spatial matching B) a été utilisée à l'étude, les résultats obtenus en utilisant la méthode de correspondance spatiale par contrainte épipolaire (Spatial matching A) sont présentés dans les Figure 2-1 à Figure 2-6. Des conclusions similaires à l'étude numérique sont trouvées.

La partie expérimentale a été réalisée par le Dr Pascal Henry Biwolé à Lyon, France.

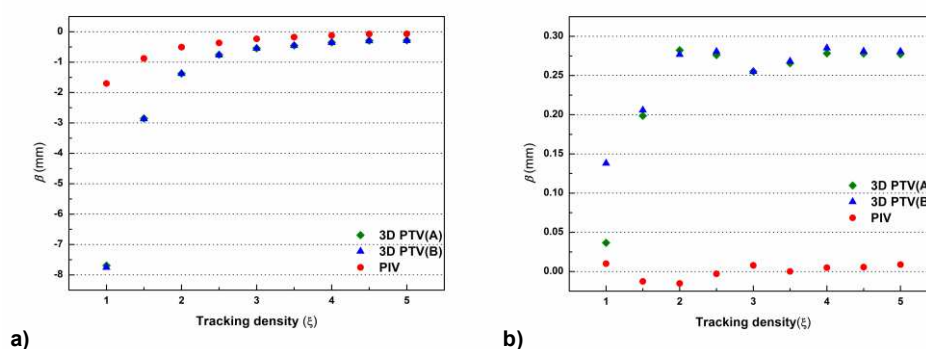


Figure 2-1: Biais pour les méthodes 3D PTV et PIV typiques sur la direction-x (a) et la direction-y (b) sous la condition de déplacement linéaire des particules dans la direction-x

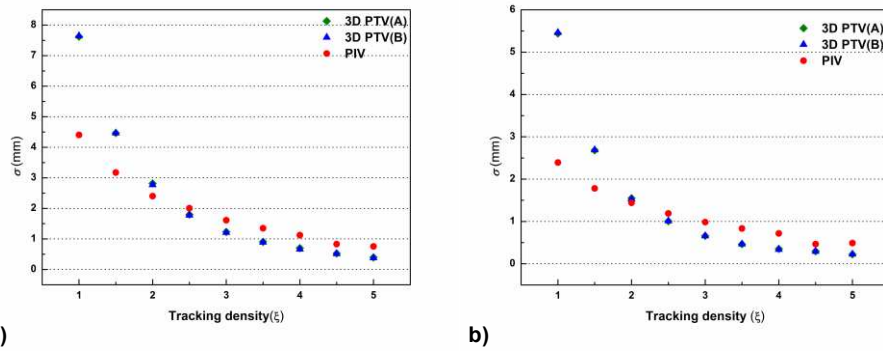


Figure 2-2: Erreurs aléatoires pour les méthodes 3D PTV et PIV typiques sur la direction-x (a) et la direction-y (b) sous la condition de déplacement linéaire des particules dans la direction-x

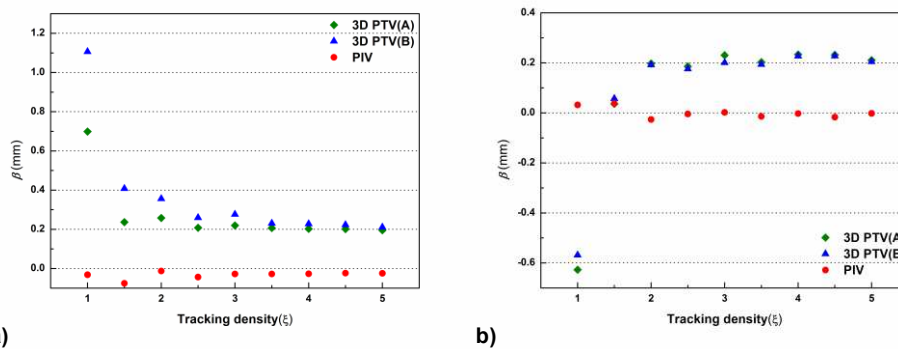


Figure 2-3: Biais pour les méthodes 3D PTV et PIV typiques sur la direction-x (a) et la direction-y (b) sous la condition de déplacement circulaire des particules

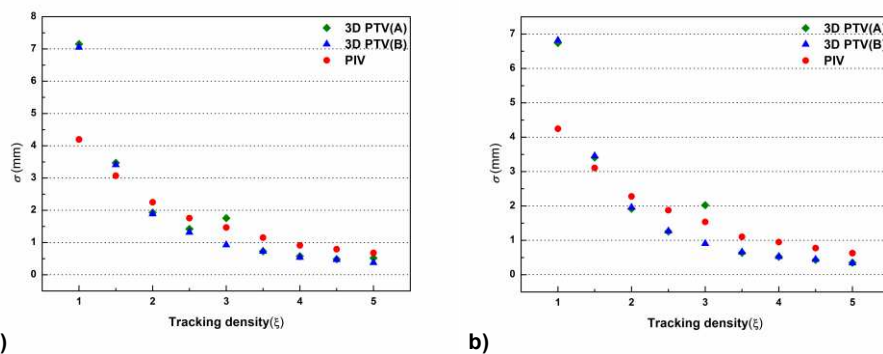


Figure 2-4: Erreurs aléatoires pour les méthodes 3D PTV et PIV typiques sur la direction-x (a) et la direction-y (b) sous la condition de déplacement circulaire des particules

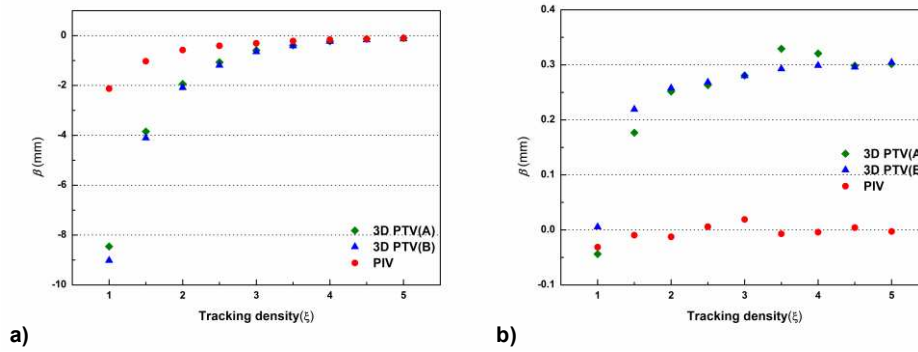


Figure 2-5: Biais pour les méthodes 3D PTV et PIV typiques sur la direction-x (a) et la direction-y (b) sous la condition de déplacement des particules sous écoulement de Kovaszny

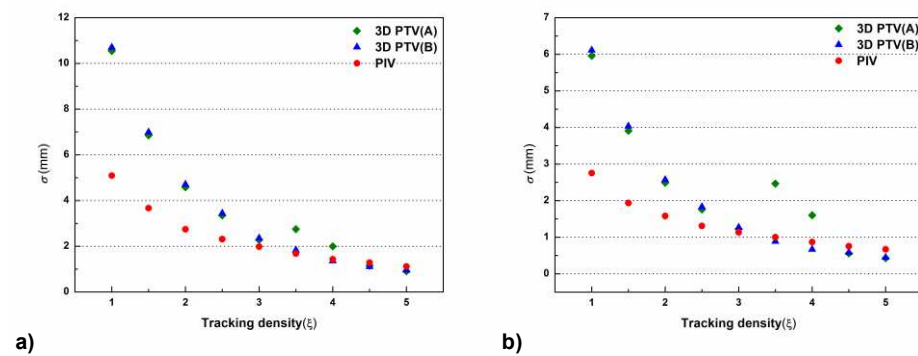


Figure 2-6: Erreurs aléatoires pour les méthodes 3D PTV et PIV typiques sur la direction-x (a) et la direction-y (b) sous la condition de déplacement des particules sous écoulement de Kovaszny

Numerical and Experimental Comparison of 3D Particle Tracking Velocimetry (PTV) and Particle Image Velocimetry (PIV) Accuracy for Indoor Airflow Study

Sijie Fu, Pascal Henry Biwole, Christian Mathis, 2016. Building and Environment 100: 40-49.

Abstract

Experimental measurement still plays an important role in indoor airflow study. To obtain three-dimensional and high-quality experimental data in building's indoor airflow study, Particle Tracking Velocimetry (PTV) and Particle Image Velocimetry (PIV) have been increasingly used. The accuracy and precision of measurement technologies is always a crucial issue. This paper first numerically compares the measuring performance of 3D PTV and typical 2D PIV algorithms on three laminar macro scale flows of known displacement, as a function of the particle tracking density defined as the ratio of mean particle spacing to mean particle displacement. Then, 3D PTV and 2D PIV results are compared using an experimental low-turbulence indoor airflow generated by a low-speed tailpipe. Results suggest that when the tracking density is smaller than two, 3D PTV generally cannot yield reliable measurement results. As the tracking density increases, 3D PTV has a better ability to measure larger displacement than PIV.

Keywords: 3D particle tracking velocimetry, 2D particle image velocimetry, measurement accuracy, tracking density

1. Introduction

Although Computational Fluids Dynamics (CFD) technology has been increasingly applied in recent years [11], experimental measurement still plays an important role to better understand the characteristics of indoor airflow. Besides, a reliable CFD simulation usually needs to be validated by abundant experimental data. For achieving high-quality experimental data, many experimental measurements are done using different modern measurement methods for indoor airflow. However, it is not an easy task to conduct perfect measurements when the airflow is unsteady and turbulent, and it is usually more difficult to measure the airflow in a three dimensional (3D) space.

Sun and Zhang [13] summarized main modern measurement methods for airflow. In general, these methods can be divided into point-wise techniques, such as Hotwire Anemometry (HWA), Ultrasonic Anemometry (UA) as well as Laser Dropper Anemometry (LDA), and global-wise techniques, including Particle Tracking Velocimetry (PTV), Particle Streak Velocimetry (PSV) and Particle Image Velocimetry (PIV). Compared to the point-wise techniques, because of the utilization of particle tracers and visualization technology, the global-wise techniques become non-intrusive for the measuring volumes, and have the ability to measure the airflow velocity fields of the whole domain directly, without displacing the measurement sensors on multiple points. Therefore, the local airflow is not be disturbed by the measurement tools, which can lead to a better understanding of the airflow characteristics.

Although PIV and PTV techniques are regarded as global-wise measurement techniques, they are actually based on different measurement principles. PIV technique, as an Eulerian measurement method, yields fluid velocity \vec{v} as a function of position x and time T , as described in Eq. (2-6). Generally, \vec{v} can be a one-, two- or three-dimensional vector, based on the PIV technique used.

$$\vec{v} = \frac{d\vec{x}}{dT} \quad (2-6)$$

In the PTV technique, as a Lagrangian measurement method, the fluid velocity \vec{v} is obtained through tracking the motion of each individual point, as a result of Eq. (2-7).

$$\vec{v}(x(T), T) = \frac{d\vec{x}}{dT} \quad (2-7)$$

Besides, Lagrangian measurement methods can yield individual point trajectories. More details on measurement principles of global-wise techniques can be found in scientific literature [e.g. 28, 39].

Abundant research has been done on PIV algorithms and on PIV accuracy evaluation during the past 25 years [e.g. 100-103]. Some commercial PIV measurement systems and some open-source PIV algorithms have also been developed and are now available. Typical PIV technology as well as its application in airflow study has been reviewed by Cao et al. [14],

and the review indicates that PIV technology is becoming a powerful measurement method in airflow study. However, PIV technology is still limited to large scale two-dimensional measurement or small-centimetric-scale three-dimensional measurement. This limitation comes from its need for laser illumination, which is very difficult to generate and control in safe experimental conditions in large three-dimensional space. Due to the availability and the easy and safe operation of ordinary halogen-like continuous light sources, 3D PTV technology can be applied in large scale three-dimensional measurement, but the complexity of tracking algorithms still limits its development to a certain extent. Nevertheless, it is more and more applied in indoor airflow measurement [104].

Whatever the measurement methods, the accuracy and precision respectively defined as the proximity of measurement results to the true value and the reproducibility of the measurement results, are always a crucial issue. However, it is not trivial to assess the accuracy and precision of PIV and PTV techniques. Regarding PIV technique, its accuracy and precision is always affected by a large range of parameters, such as particle image concentration, particle image size, background lighting, the positions of the camera, the ability of tracer particles to follow the flow, etc. [103, 105]. Similarly, these parameters also have influence on the accuracy and precision of the PTV technique. Substantial research has been devoted to investigate the effects of these parameters on the accuracy and precision of PTV and PIV techniques [e.g. 82, 106, 107]. Kim et al. [108] compared the experimental measurement results of Tomo-PIV and 3D PTV for micro-fluidic flows. Such a comparison is still lacking in large scale air volumes. Besides, in these previous researches, the effect of 'tracking density', an indicator of tracking difficulty introduced by Malik et al. [37], is seldom considered. Generally, bigger tracking density means easier particle tracking.

In traditional PIV, seeding density is usually chosen high [50], without any reference to the spacing-displacement ratio. On the contrary, in 3D PTV, the tracking density is generally chosen based on the ability of the tracking algorithm to tackle strong seeding density, on the size of the measuring volume and on the ability of the particle generator to produce numerous particles. Biwole et al. [27] tested their 3D PTV algorithm using a tracking density ranging from 2.1 to 8.1, while Barker et al. [75] and Lobutova et al. [47] used tracking density of the order of 25 for 3D PTV in volumes over three cubic meters.

This paper firstly investigates the effect of small tracking densities (from 1 to 5) on the accuracy and precision of macro scale 2D PIV and 3D PTV measurement using numerical methods. Then, typical 2D PIV and 3D PTV are used to conduct a comparative measurement on low turbulence airflow in real experimental conditions. The paper solely compares the ability of PIV and PTV to measure instantaneous velocity fields. The ability of PTV to provide trajectories is not taken into account since PIV is an Eulerian measurement method.

2. Comparing the effect of tracking density on 3D PTV and typical PIV

The “tracking density” index hereafter noted ζ is defined as the ratio of mean particle spacing in a nearest neighbor sense to mean displacement of particles between two

consecutive frames. Although the tracking density can be calculated in real experiment measurement, it is still impossible to quantify its effect on actual flows especially when they are turbulent. In real experimental conditions, many other parameters also have influences on final measurement results. Therefore, in this study, synthetic particle motion is employed to demonstrate the effect of the tracking density index on the accuracy and precision of measurement using 3D PTV and typical PIV techniques. The main advantage of using synthetic particle images is that simulation parameters can be varied systematically, and the individual contributions of different parameters to the total errors can be estimated.

2.1 Synthetic images

The method of using synthetic images has been applied to evaluate the performance of PIV and PTV algorithms under many different imaging and flow field conditions [e.g. 46, 75, 103, 106, 107, 109, 110]. Several publicly available image sets and image generation tools have been developed for this purpose [e.g. 111, 112]. In this study, a custom code written in the MATLAB[®] is developed to generate the synthetic images using the method described below.

Before generating synthetic images, multi-camera calibration parameters using three real PTV cameras, one PIV camera and a real calibration target object are obtained using the method proposed by Zhang [66]. Especially, the optical axis of the PIV camera is strictly perpendicular to the field of view. The parameters obtained for each camera are the focal length, the radial and tangential distortion coefficients, the principal point pixel coordinates, the skew coefficient defined as the angle between x_{cam} and y_{cam} pixel axes on the CCD chip, and the rotation and translation matrices defining the relationship between each camera 3D coordinate system and the common 3D (real world) coordinate system defined by the calibration target.

These parameters will be used to project the world's coordinates of prescribed particles onto the synthetic images. Three-dimensional coordinates (x, y, z) of a prescribed number of particles N_p are randomly generated in a three-dimensional volume $(X (0.5m) \times Y (0.5m) \times Z (0.5m))$. Because typical PIV measurement is usually conducted in a two-dimensional domain, the coordinates of particles on one direction (z -direction) are set to zero for synthetic images in this study. The number of particles N_p is prescribed dependent on the following principles: For PIV images, the number of particles for every independent interrogation window is set as four, which is the minimum number of particles which makes PIV work effectively [103]. For PTV images, since every independent particle will be tracked along the time, the particle concentration should not be too high. However, if the number of particles is too small, it leads to large mean particle spacing and therefore large displacement between two consecutive images when the tracking density is kept constant. Consequently, the number of particles for PTV images is defined as about ten percent of the number of particles for PIV images. The luminance is imposed randomly for each particle in the synthetic images. No noise is added on the synthetic images. An example of the particle image generated using the method described above is shown in Figure 2-7.

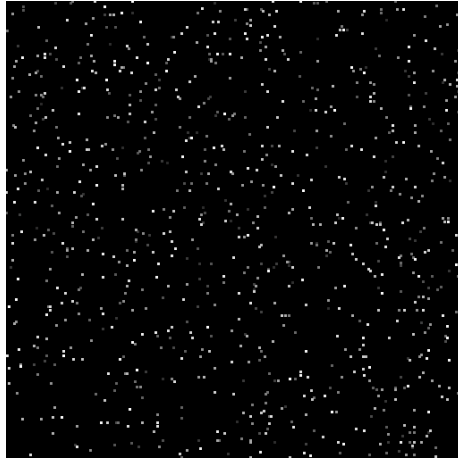


Figure 2-7: An example of the synthetic images (512 pixel \times 512 pixel)

Three laminar motions are imposed on each particle generated in the three dimensional volume: a linear motion of constant particle velocity, a circular motion of constant particle velocity, and a Kovaszny flow [113] motion of particle velocity defined as:

$$\begin{cases} v_x = 1 - \exp(\lambda x) \cos(2\pi y), v_y = \frac{\lambda}{2\pi} \exp(\lambda x) \sin(2\pi y) \\ \lambda = Re/2 - (Re^2/4 + 4\pi^2)^{0.5} \end{cases} \quad (2-8)$$

Here, the Reynolds number Re is chosen as 40, and special ratios are applied on the original velocity field so that the particle movement is suitable for different tracking densities.

Some additional conditions are applied for every type of particle motion. For linear motion, the particle displacement is imposed along the x -direction only. For circular motion, the particle displacement is concentric, based on the center of the measured domain. Figure 2-8 shows the schematic of the three types of particle movement described above.

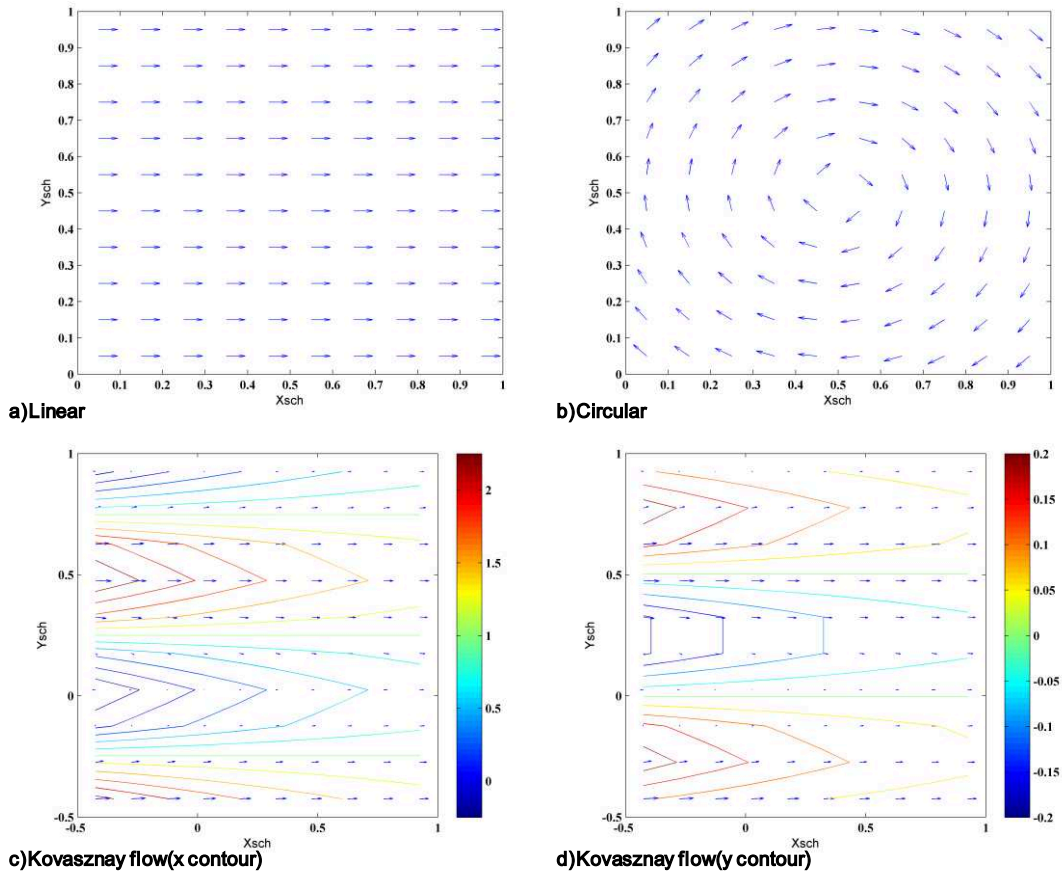


Figure 2-8: Schematic of linear particle movement (a), circular particle movement (b) and Kovaszny flow particle movement (c, d)

2.2 Measurement algorithms

2.2.1 PIV algorithm

For the 2D PIV technique, the preferred method is to perform the multi-step cross-correlation analysis between two consecutive images. The basic theory of cross-correlation analysis of PIV images has been introduced in previous papers [e.g. 114]. The cross-correlation function has a significant peak, providing the magnitude and direction of the velocity vector without ambiguity. The correlation methods are commonly based on the digital fast Fourier transform (FFT) algorithms to calculate the correlation functions. Other cross-correlation methods based on many other algorithms have also been developed and applied for PIV measurement [e.g. 106, 107]. The aim of this study is not to develop the PIV technique, therefore, the cross-correlation method based on the FFT algorithm is adopted for PIV analysis and all analysis are done using the open source software OpenPIV [115]. During the analysis process, the interrogation window size is set on 32 pixels \times 32 pixels, and no overlap is used.

2.2.2 PTV algorithm

For the 3D PTV technique, a complete tracking algorithm is usually made of five main steps: multi-camera calibration, image processing, particle center detection, 2D or 3D tracking and 3D reconstruction. Among these five main steps, the last three parts generally define the tracking strategy. Ouellette et al. [64] reviewed the usual tracking algorithm schemes. Through the function of the tracking strategy, the particle trajectories and fluid velocity are finally obtained. In general, particle tracking strategies may be divided into two types as illustrated in Figure 2-9 [104]. In the first type (Figure 2-9(a)), each particle in the image domain of each camera is tracked firstly through time based on the successive frames (2D tracking), and then the 3D trajectories are reconstructed by spatial matching of the 2D trajectories obtained. In the second type (Figure 2-9(b)), the 3D coordinates of particles are calculated at each time step and the tracking is done directly in the object domain (3D tracking). It is noted that spatial matching can also be done before 2D tracking for the first type of tracking strategies. Besides, some hybrid tracking scheme using features from each type can be found in the literature [e.g. 40].

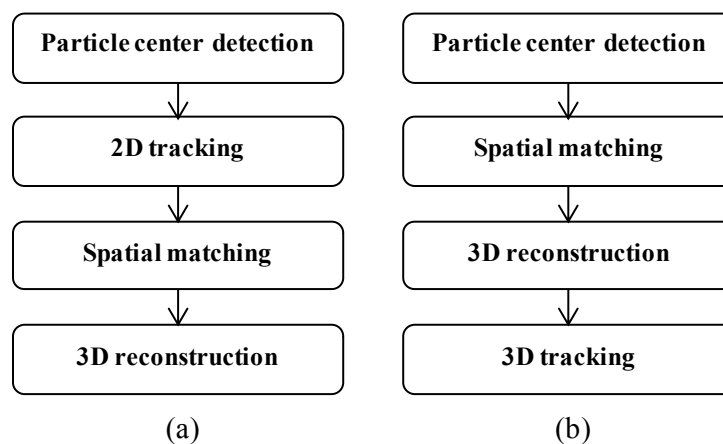


Figure 2-9: Flow chart of particle tracking strategies [104]

The aim of this study is to investigate the effect of tracking density, so image pairs are used to conduct the measurements with 2D typical PIV and 3D PTV techniques. However, 3D PTV techniques usually use simple methods to initialize trajectories on the first two frames, such as giving a constant search radius or choosing the particle with the position closer to the previous one. In this study, a modified fast normalized cross-correlation tracking algorithm is used in 2D tracking, which means the first type of tracking strategies is adopted to investigate the effect of tracking density for measurement results. The details of the complete 3D PTV algorithm are described as following:

1) Multi-camera calibration

Multi-camera calibration parameters using three real PTV cameras, one PIV camera and a real calibration target object are obtained using the method proposed by Zhang [66].

2) Image processing

Because the synthetic images are used in the analysis, the image processing step is not needed in this study.

3) Particle center detection

In this study, weight-average method is adopted to conduct particle center detection, due to the fact it is efficient, rapid and readily implemented.

4) 2D tracking

Temporal tracking is the most important part in 3D PTV algorithms. Here, a modified fast normalized cross-correlation tracking algorithm is used. The implementation of normalized cross-correlation follows the equation from [116]:

$$\gamma(u, v) = \frac{\sum_{x,y} [f(x, y) - \bar{f}_{u,v}] [t(x-u, y-v) - \bar{t}]}{\sqrt{\sum_{x,y} [f(x, y) - \bar{f}_{u,v}]^2 \sum_{x,y} [t(x-u, y-v) - \bar{t}]^2}} \quad (2-9)$$

where f is the research window, \bar{t} is the mean of the template (i.e. interrogation window) and $\bar{f}_{u,v}$ is the mean of $f(x, y)$ in the region under the template. Instead of searching a pattern made of a group of particles at the next frame, the pattern here becomes a single particle. And in order to solve the tracking ambiguities when there are more than one correlation peak, a procedure by the Lagrangian extrapolation of an estimate position using the last three or last two positions of the particle is applied, as Eq. (2-10) expresses. The physical meaning of the extrapolation is a minimization of changes in particle acceleration. The particle closest to the estimated position is chosen.

$$\mathbf{x}_{pre} = \mathbf{a}t^2 + \mathbf{b}t + \mathbf{c} \quad (2-10)$$

where \mathbf{x}_{pre} is the estimate position, t is the frame number and \mathbf{a} , \mathbf{b} , \mathbf{c} are the coefficients determined by polynomial curve fitting in a least square sense.

5) Spatial matching and 3D reconstruction

In this study, spatial matching is done before 2D tracking using the combined method of calculating real 3D coordinates and the epipolar constraint [117].

In general, there are two methods to do spatial matching, one is to use epipolar constraint and triangulation (referred to as spatial matching A in the following), and another is to calculate real world 3D coordinates of particles by triangulation using 2 cameras at a time and to compare the results (referred to as spatial matching B in the following).

The principle of spatial matching A is illustrated as:

$$F_{ij} = [T_i - R_i R_j^T T_j]_x R_i R_j^T \quad (2-11)$$

$$[u]_x = \begin{pmatrix} 0 & -u_k & u_j \\ u_k & 0 & -u_i \\ -u_j & u_i & 0 \end{pmatrix} \quad (2-12)$$

$$[x'_i \quad y'_i \quad 1] F_{ij} \begin{bmatrix} x'_j \\ y'_j \\ 1 \end{bmatrix} < s \quad (2-13)$$

where F_{ij} is the fundamental matrix of each pair of cameras, R_i, R_j, T_i, T_j are extrinsic parameters given by calibration, $[u]_x$ defines the cross-product used in Eq. (2-11), (x_i, y_i) and (x_j, y_j) are the normalized pixel coordinates from each trajectory, t is an instant time, and s is a threshold value which is empirically given the value $s = 1$. If (x_i, y_i) and (x_j, y_j) satisfy Eq. (2-13), it means that the particle is matched at this instant time.

Figure 2-10 illustrates the principle of spatial matching B. If real world 3D coordinates calculated by triangulation using a couple of centroids (1, 3) are ‘similar’ to the real world coordinates calculated using another couple (1, 5), then centroids 3, 1 and 5 are images of the same particle. The similarity criterion is defined as the minimum of Euclidean distance among every other 3D coordinates. Assuming $A_i(x_a, y_a, z_a)$ and $B_j(x_b, y_b, z_b)$ are two real world’s coordinates, Eq. (2-14) will be searched.

$$\min_{i,j} (\|A_i - B_j\|) = \min_{i,j} (\sqrt{|x_a - x_b|^2 + |y_a - y_b|^2 + |z_a - z_b|^2}) \quad (2-14)$$

where $\| \cdot \|$ is the 2-norm. At the end of the matching process, the remaining unmatched particles are usually discarded since those particles cannot be recorded by all three cameras. In this study, in order to match the particles only seen by two cameras, spatial matching A is applied when spatial matching B is finished. More details about spatial matching and 3D reconstruction can be found in [27, 118].

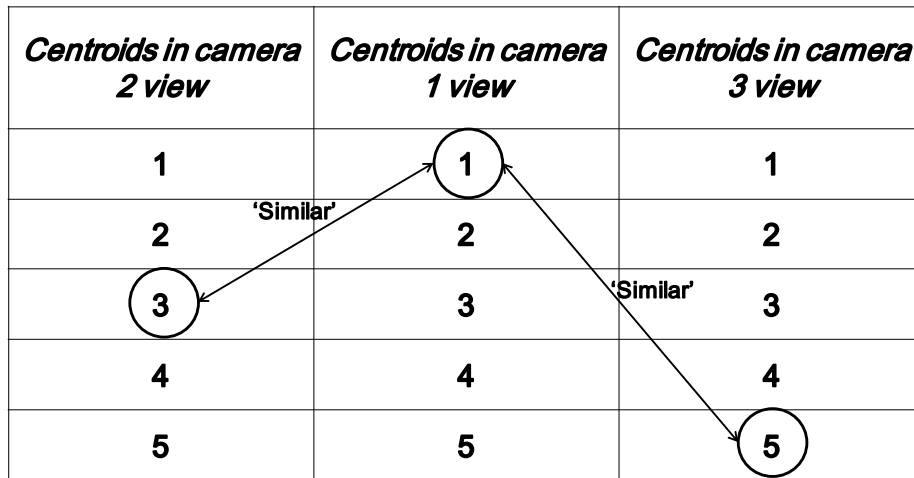


Figure 2-10: Illustration of the identification algorithm for spatial matching

2.3 Evaluation parameters

Bias (β) and random errors (σ) are chosen as the evaluation parameters to assess respectively the accuracy and precision of both typical PIV and 3D PTV measurement results. Bias is defined as:

$$\beta = \frac{1}{N} \sum_1^N (d_m - d_r) \quad (2-15)$$

where d_m is the ‘measured’ displacement obtained from typical PIV or 3D PTV algorithms

processing synthetic particle images which have an imposed ‘true’ displacement of d_r . To get β , the instantaneous local error ($d_m - d_r$) is averaged over N samples which are spatially distributed over the image area and across several image pairs where appropriate. Random error is isolated from RMS total error Eq. (2-16) and defined in Eq. (2-17).

$$\delta = \sqrt{\frac{1}{N} \sum_1^N (d_m - d_r)^2} \quad (2-16)$$

$$\sigma = \sqrt{\delta^2 - \beta^2} \quad (2-17)$$

The bias and random errors are calculated in millimeters. For every assumed type of particle movement, 20 image pairs are analyzed for every different tracking density.

2.4 Results

2.4.1 Linear particle motion

The bias on x-direction and on y-direction is shown in Figure 2-11 (a) and Figure 2-11 (b) respectively. Figure 2-11 (a) clearly suggests that the bias of both 3D PTV and typical PIV measurement is bigger as the tracking density is closer to one. Then, it tends toward zero as the tracking density increases. The absolute value of the bias of 3D PTV is always bigger than that of typical PIV, especially on small tracking densities. Because no displacement is imposed on the y-direction, the bias of both typical PIV and 3D PTV on the y-direction is nearly constant, regardless of the value of the tracking density, as shown in Figure 2-11 (b). For typical PIV, the bias varies between -0.0153mm and 0.00995mm for all tracking density, whereas for 3D PTV, it varies between 0.26238 mm and 0.28709 mm when the tracking density becomes higher than 2. When the tracking density is smaller than 2, the bias of 3D PTV shows the smaller value, however, its random errors have higher value. Therefore, it doesn't mean that 3D PTV has a better performance with much smaller tracking density.

Figure 2-12 shows the random errors of both 3D PTV and typical PIV measurement results. The figure clearly shows that the random errors of both measurement methods decrease and approach zero as the tracking density increases. When the tracking density is less than 2, the random error of 3D PTV is bigger than that of typical PIV. Then, around $\zeta = 2.5$, the random error of 3D PTV becomes smaller than that of PIV. The bias and random errors suggest that the typical PIV method usually performs better than the 3D PTV method when the tracking density is very small.

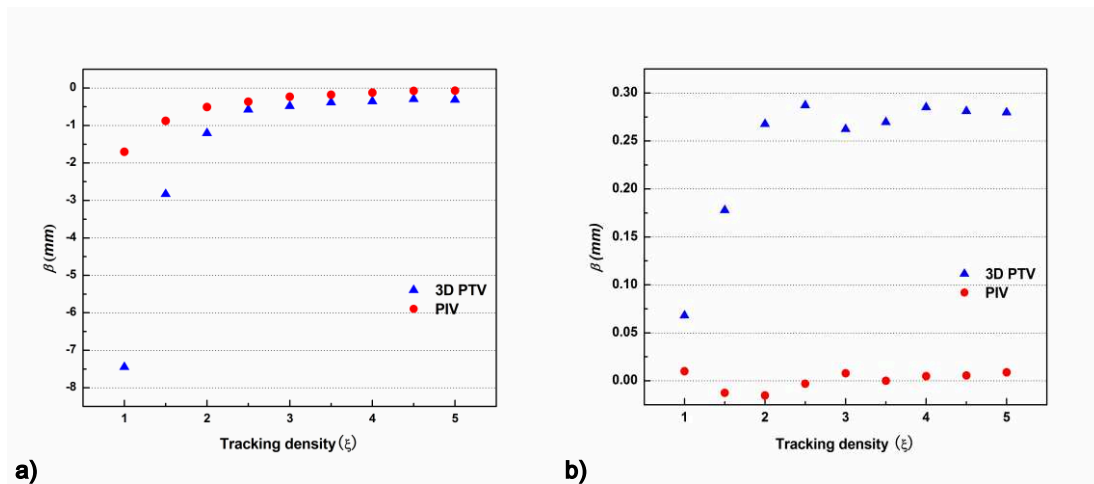


Figure 2-11: Bias of 3D PTV and typical PIV methods on x-direction (a) and y-direction (b) under the condition of linear particle motion along the x-direction.

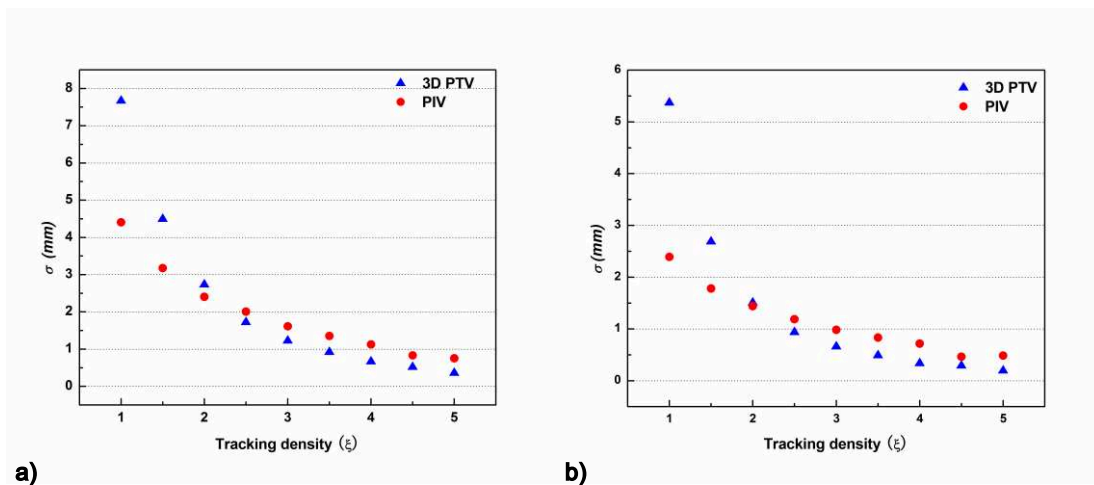


Figure 2-12: Random errors of 3D PTV and typical PIV methods on x-direction (a) and y-direction (b) for the condition of linear particle motion along the x-direction.

2.4.2 Circular particle motion

The bias and random errors of both 3D PTV and typical PIV for a circular particle motion are shown in Figure 2-13 and Figure 2-14 respectively. The figures show similar results as illustrated in the linear particle motion. However, it is noted that the bias of 3D PTV on x-direction tends toward 0.2 mm instead of zero as the tracking density increases. It is due to the cumulative effect of errors in camera calibration and particle center calculation, which reflect in the 3D reconstruction step. The bias of typical PIV on the same direction is around zero and varies between -0.0757 mm and -0.0128 mm for all tracking density. When the tracking density is equal to 2 or higher, the random error of 3D PTV becomes smaller than that of typical PIV on both x and y directions.

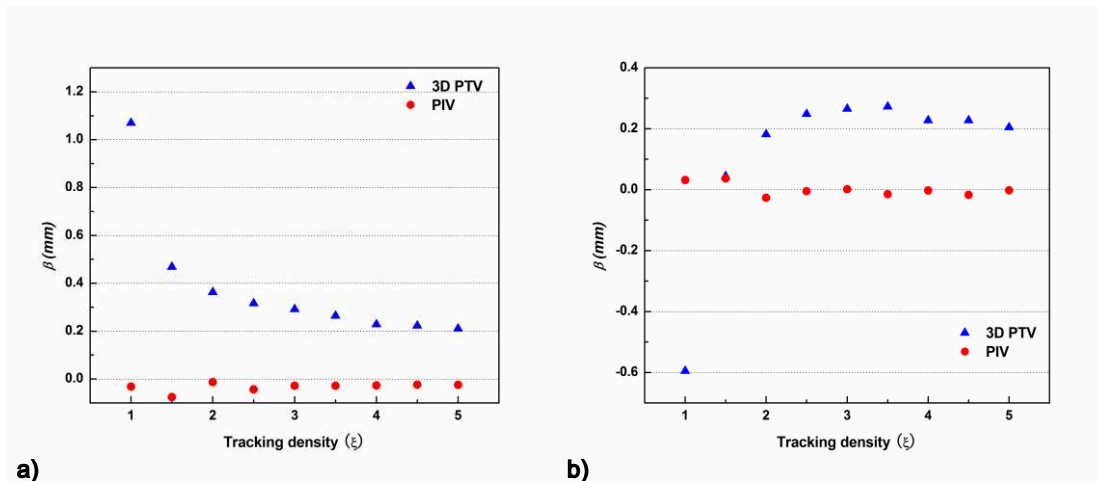


Figure 2-13: Bias of 3D PTV and typical PIV methods on x-direction (a) and y-direction (b) under the condition of circular particle motion

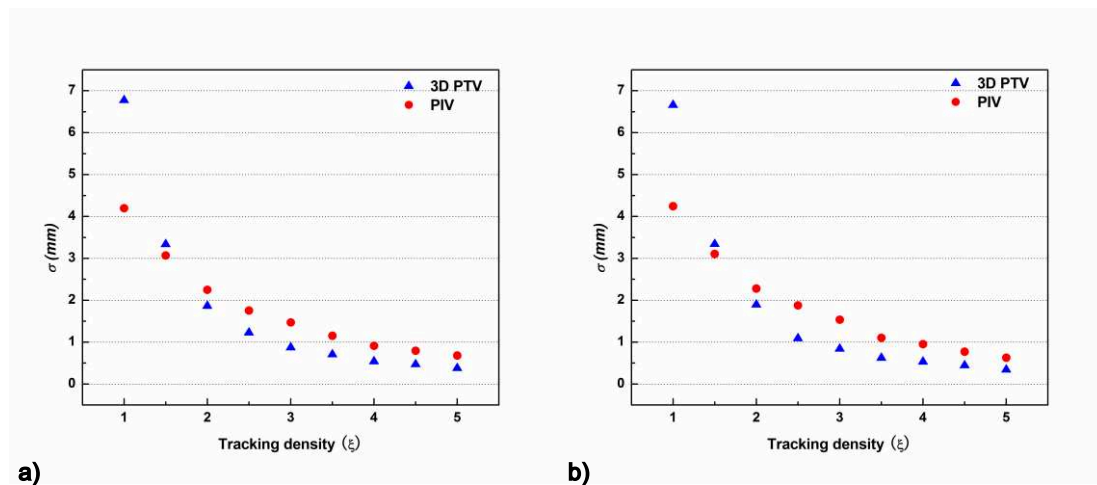


Figure 2-14: Random errors of 3D PTV and typical PIV methods on x-direction (a) and y-direction (b) under the condition of circular particle motion

2.4.3 Kovaszny flow particle motion

Figure 2-15 and Figure 2-16 illustrate the bias and random errors of both 3D PTV and PIV respectively, when applied on a laminar Kovaszny flow. Similar results as in sections 2.4.1 and 2.4.2 are found again. However, it is noted that when the tracking density is from 1 to 3.5, the bias and random error of 3D PTV are always bigger than that of typical PIV measurement results. Beyond $\xi = 3.5$, 3D PTV starts performing better than PIV in terms of random error.

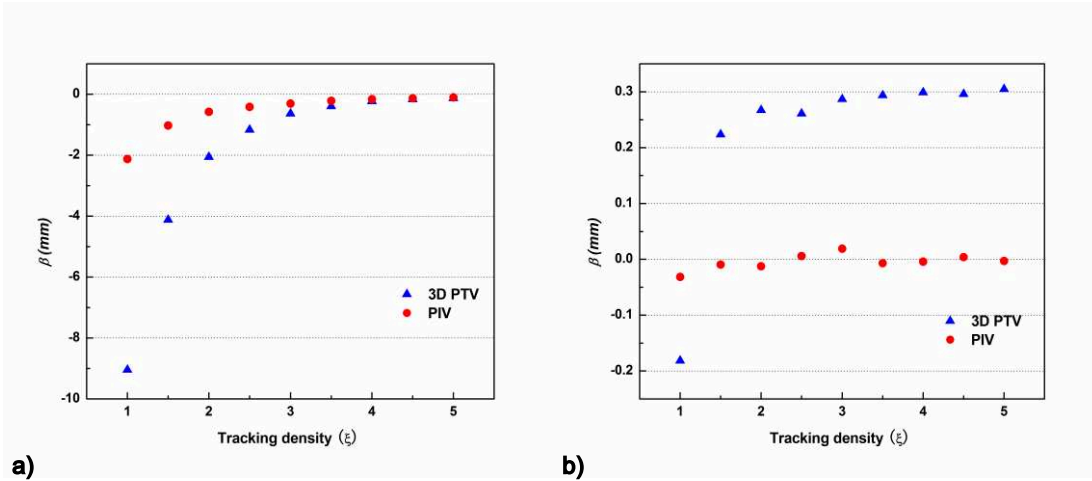


Figure 2-15: Bias of 3D PTV and typical PIV methods on x-direction (a) and y-direction (b) under the condition of Kovaszny flow particle motion

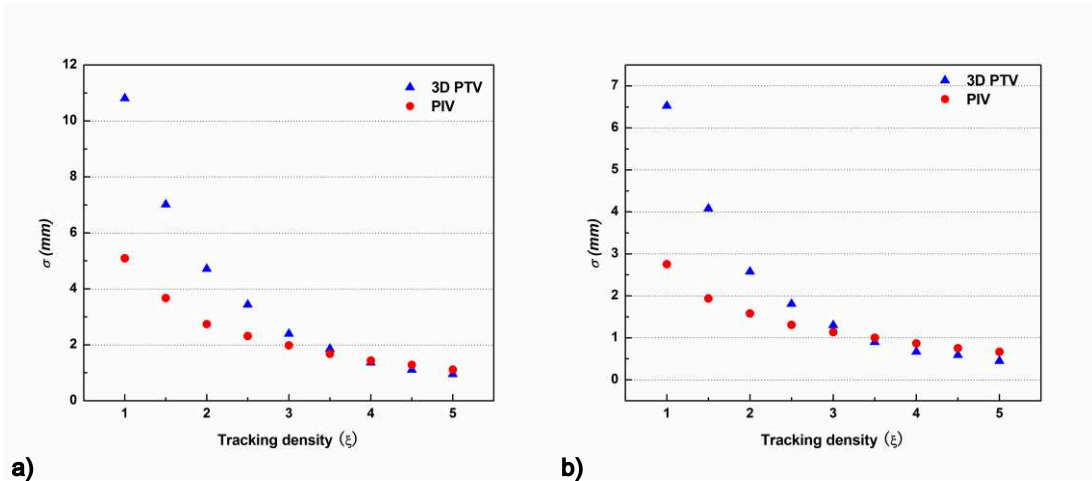


Figure 2-16: Random errors of 3D PTV and typical PIV methods on x-direction (a) and y-direction (b) under the condition of Kovaszny flow particle motion

2.4.4 Summary on numerical comparison of 3D PTV and typical PIV

Based on the bias and random errors shown from section 2.4.1 to section 2.4.3, it can be concluded that the tracking density has a significant influence on the measurement accuracy and precision. As the tracking density increases, the accuracy and precision of both 3D PTV and typical PIV measurements increase. Generally, when the tracking density is smaller than 2, the 3D PTV technique cannot provide reliable measurement results. However, when the tracking density is bigger than a value dependent on the flow characteristics, 3D PTV obtains better measurement accuracy and precision than typical PIV. Because the mean particle spacing of 3D PTV is usually larger than that of typical PIV, using a constant tracking density value to compare the two techniques means larger particle displacement for 3D PTV. Therefore, the results shown in 2.4.1 to 2.4.3 also indicate that 3D PTV technique has a better ability to measure larger displacement than typical PIV provided that the tracking density is appropriate.

3. Comparison of 3D PTV and typical PIV for experimental measurement

3.1 Experiment set-up

A cylindrical tailpipe equipped with a motored centrifugal fan at the back (see Figure 2-17) is used to generate the airflow velocity field. The air is first blown into a cylindrical chamber of 188 mm diameter and 200 mm length and in which are placed two grids. The central portion of the first grid comprises a round plate to break the incoming stream, thereby forcing the fluid to occupy the whole of the first chamber. The use of perforated gratings reduces the intensity of turbulence and helps eliminating possible non-uniformities of the flow [119, 120]. From the first chamber, the fluid passes through a bottleneck and exits through a cylindrical nozzle of diameter 68.6 mm. The effect of the contraction is also to reduce the intensity of turbulence of the flow and improve its homogeneity. The centrifugal fan is powered by an AC voltage that can be varied using a rheostat. Nozzle air velocity depends on the voltage applied on the fan engine terminals. The effective value of the voltage across the fan motor is measured by a digital voltmeter.

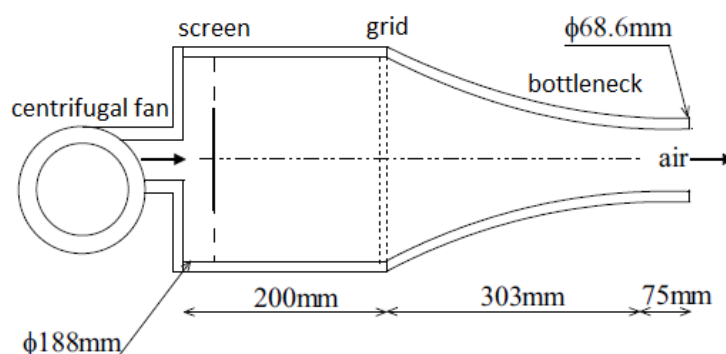


Figure 2- 17: Outline of the low-speed tailpipe.

PIV measurements are made using a Nd:Yag pulsed laser as the illumination system and incense particles with the average diameter of 1 μm are employed as the tracers. The set-up of the PIV measurement is shown in Figure 2-18. A small rectangular black piece of paper is placed above the first chamber of the tailpipe to serve as target for the laser sheet (see Figure 2-19). The PIV camera is equipped with a sensor of resolution 1370x1040 pixels. The time between two double recordings is 0.1s. The error on the velocity measurement at the tailpipe nozzle with the PIV system is $\pm 0.03\text{m/s}$ with an interval of confidence of 95% [120].

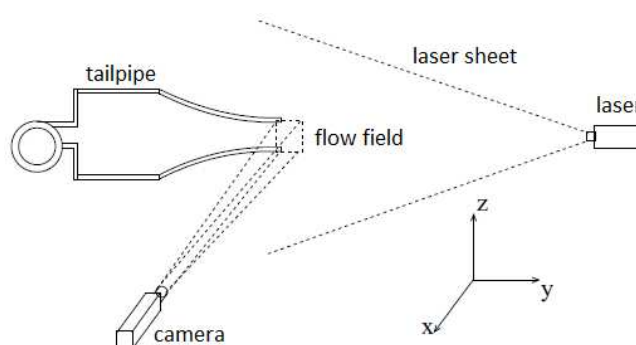


Figure 2-18: PIV measurement set-up

For PTV measurements, the illumination system is provided by six 1000W compact fluorescent BalcarQuadlite lamps which are separated from the measured airflow domain by a glass wall to prevent heating. Helium-filled soap bubbles with the average diameter of 2 mm instead of the incense particles are employed as tracers. The bubbles are generated from a commercial bubble generator by Sage Action inc [93]. In order to inject the tracers into the measured domain, a 1 cm hole is drilled on top of the second chamber and a pipe coming from the bubble generator is tied to the tailpipe as shown in Figure 2-19. For PIV measurements, a high particle concentration is usually needed in order to obtain a better result, thus incense particles are selected as the tracers. However, for PTV measurements, low particle concentration means more reliable results when the measured velocity is constant, because as the number of particles increases, the tracking density will decrease, so the measurement errors will increase significantly.

Three digital cameras Dalsa 4M60 with CMOS chip resolution set at 1024x1024 pixels are used as the image recording devices. The time between two recordings is 0.01s. The recording computers for PIV and PTV are placed outside the room also to prevent heating of the flow. In order to estimate the repeatability of the measurement by 3D PTV on the tailpipe, 10 measurements at constant input voltage of $U_{\text{eff}} = 43.7 \text{ V}$ are carried out, and a mean velocity of 0.656 m/s with an uncertainty of $\pm 0.012 \text{ m/s}$ is obtained. The uncertainty is taken as the maximum deviation from the mean measured value 0.656 m/s. This error is due to the fact that the exact measured point cannot be prescribed in 3D PTV.

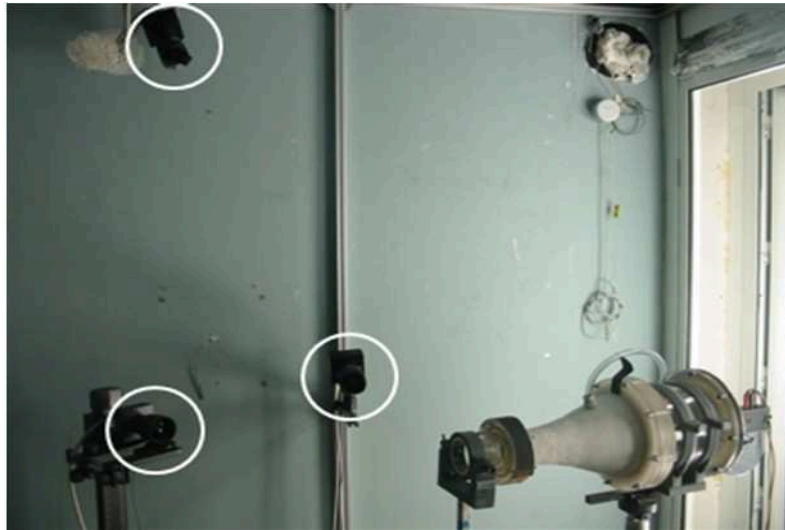


Figure 2-19: Low-speed tailpipe inside experimental room MINIBAT, Lyon, France. The position of the three PTV cameras is shown by white circles.

3.2 Results

Measurements are made at 5 mm from the tailpipe nozzle, close to its centerline, for speeds generated by the following voltages at the fan engine terminals: 18.4V, 35.6V, 43.7V, 53V, 62.1V, 72.2V, 82.4 V, which makes the airflow velocity ranging from 0.2 m/s to approximately 2m/s.

Figure 2-20 illustrates the results obtained by typical PIV and 3D PTV methods. Results of each method are represented with the corresponding bars of error. PIV was unable to correctly measure low speeds of the order of 0.24m/s ($U_{eff}= 18.4$ V). As the air velocity increases, there is a better agreement between PTV and PIV measurement.

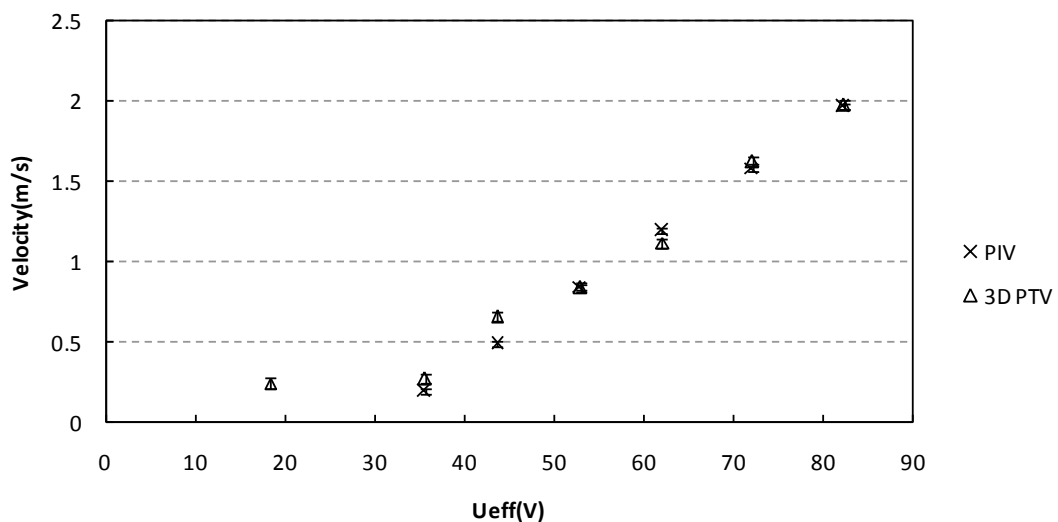


Figure 2-20: Comparison of velocity measurement results with PIV/PTV on a low-speed tailpipe

4. Conclusions

This article presents a comparative study of results from typical PIV and 3D PTV as a function of the tracking density index, using three numerically generated macro scale laminar flows, and one experimental low turbulence flow. The numerically generated flows are namely, a linear flow, a circular flow and a Kovasznay flow. Cross-correlation algorithm with FFT function and modified normalized cross-correlation algorithm are used as the core algorithm for typical PIV and 3D PTV respectively. The bias and random errors of all measurement results indicate that small tracking density has significant influence on the measurement accuracy and precision, and as the tracking density increases, the measurement accuracy and precision of both measurement methods increase. Results also show that, generally, 3D PTV cannot give a reliable result when the tracking density is smaller than 2. But 3D PTV shows a better measurement performance than typical PIV when the tracking density is bigger than 4. Moreover, 3D PTV has a better ability to measure larger displacement than PIV when the tracking density is suitable.

For the experimental comparative study, typical PIV and 3D PTV using a modified cross-correlation algorithm are used to measure several speeds on one direction of the airflow at the exit of a low-speed tailpipe. The results indicate that the difference between PIV and PTV becomes bigger as the air velocity decreases. These conclusions suggest that tracking density has direct and important influence on typical PIV and 3D PTV measurement results. Therefore, pre-evaluating an appropriate tracking density may have a significant impact on the measurement process.

Acknowledgements

This work was supported by a grant from the French Region Provence Alpes Côte d'Azur and by a funding from the French National Research Agency (ANR) through the FLUBAT project (ANR-12-VBDU-0010). The authors would also like to thank Prof. Frédéric Kuznik from the University of Lyon, France.

3 Comparaison numérique et expérimentale d'algorithmes complets de vélocimétrie 3D par suivi de particules (PTV) algorithmes pour l'étude des écoulements d'air intérieur

Résumé en français

Dans la chaîne de mesure 3D PTV, les performances des algorithmes de mesure 3D PTV ont une influence directe et forte sur les résultats de mesure finaux. Dans ce chapitre, les performances de sept algorithmes 3D PTV complets sont évaluées, afin de décider d'un programme approprié pour faire l'investigation expérimentale. Dans ces algorithmes, les méthodes de calibration à plusieurs caméras, le traitement d'image, la détection du centre des particules et la reconstruction en 3D sont tous identiques; par contre, quatre algorithmes de suivi temporel différents et deux types d'algorithmes de correspondance spatiale sont utilisés pour générer les différences entre ces sept algorithmes.

L'algorithme de suivi temporel I (Algorithme I) est proposé par Li et al. [81] Dans cet algorithme, le suivi se fait d'abord en 2D et il utilise une méthode de régression polynomiale quadratique pour prédire la position du centre de la région de recherche, comme illustré par l'Eq. (3-1).

$$x_{pre} = at^2 + bt + c \quad (3-1)$$

En outre, une fonction de coût est utilisée pour résoudre les conflits dans la zone de recherche, cf. l'Eq. (3-2) l'illustre.

$$\phi = \frac{\sqrt{\sum_{k=0}^3 |D_k - G\tau_k - H|^2}}{\sqrt{\sum_{k=0}^3 |D_k|^2}} \quad (3-2)$$

L'algorithme de suivi temporel II (Algorithme II) provient de celui proposé par Biwole [45], en utilisant la corrélation croisée normalisée rapide modifiée, cf. l'Eq. (3-3), pour le suivi temporel 2D. Dans cet algorithme, le motif recherché est constitué de chaque particule unique au lieu d'un groupe de particules comme dans la PIV traditionnelle. A la différence de la version originale, ici, les particules qui ne sont pas connectées à l'image précédente sont utilisés pour démarrer de nouvelles trajectoires.

$$\gamma(u, v) = \frac{\sum_{x,y} [f(x, y) - \bar{f}_{u,v}] [t(x-u, y-v) - \bar{t}]}{\sqrt{\sum_{x,y} [f(x, y) - \bar{f}_{u,v}]^2 \sum_{x,y} [t(x-u, y-v) - \bar{t}]^2}} \quad (3-3)$$

L'algorithme de suivi temporel III (Algorithme III) est basé sur l'algorithme présenté par Barker [49]. Cet algorithme effectue le suivi des particules dans l'espace 3D. Dans cet algorithme, la méthode du plus proche voisin est utilisée pour initialiser les trajectoires des particules entre les deux premiers cadres et une approximation de la vitesse au premier ordre est utilisée pour estimer la position de la particule dans la nouvelle image, cf. les Eqs. (3-4) et

(3-5). A la différence de l'algorithme original, la méthode de régression polynomiale est adoptée pour prédire la position du centre de la région de recherche sur l'image à $t+1$ quand une trajectoire ne parvient pas à trouver une particule candidate optimale pour l'image t .

$$x_{pre}^{t+1} = x^t + u^t \Delta T \quad (3-4)$$

$$u^t = \frac{x^t - x^{t-1}}{\Delta T} + O(\Delta T) \quad (3-5)$$

Le dernier algorithme de suivi temporel (Algorithme IV) est dérivé du troisième algorithme de suivi temporel. La seule différence est qu'il utilise la méthode de corrélation croisée modifiée au lieu de la méthode du plus proche voisin pour initialiser les trajectoires de particules entre les deux premières images.

Les deux méthodes de correspondance spatiale différentes utilisées ici ont été introduites dans le chapitre 2, cf. les Eqs. (2-1) à (2-5).

La Figure 3-1 représente le schéma des algorithmes complets de mesure 3D PTV testés.

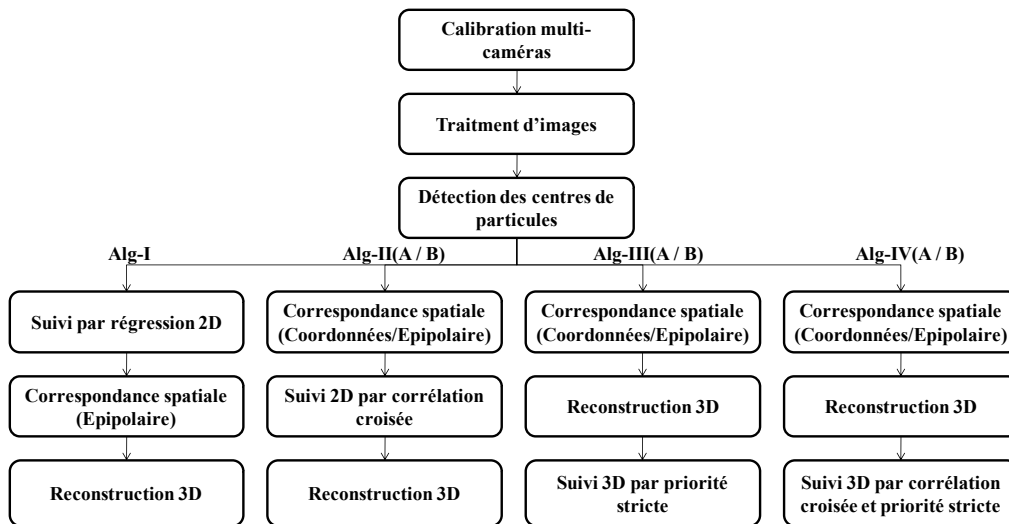


Figure 3-1: Le diagramme des sept algorithmes complets de suivi de particules en 3D comparés

L'évaluation a été faite numériquement sur deux types d'écoulements laminaires 3D macroscopiques, solutions connues de l'équation de Navier-Stokes, à savoir les écoulements de Kovaszny et Beltrami. La comparaison est basée sur l'exactitude, le nombre de trajectoires détectées, et la longueur maximale des trajectoires de chaque algorithme en fonction de la densité de suivi des particules et du nombre total d'images. Les résultats des tests numériques montrent que les performances de l'ensemble des algorithmes de mesure 3D PTV augmentent à mesure que la densité de suivi des particules augmente, à l'exception de l'algorithme de mesure I, qui présente une tendance inverse ce qui signifie que cet algorithme est mieux adapté au suivi de grands déplacements de particules, à espacement de particules constant. Quand le nombre d'images suivies augmente, les performances de tous les algorithmes de mesure sont clairement réduites, ce qui suggère qu'en divisant du nombre total d'images en des ensembles de plus petite taille et en réinitialisant le suivi sur chaque groupe, on peut améliorer la précision de tout algorithme de mesure 3D PTV. Les algorithmes

utilisant la contrainte épipolaire plutôt que la méthode de correspondance spatiale ont généralement de meilleures performances. Les résultats suggèrent également que les algorithmes ayant la capacité de fournir le plus de trajectoires de particules n'ont pas nécessairement la meilleure précision de suivi.

Les algorithmes de mesure qui ont de meilleures performances sont ensuite comparés expérimentalement sur un vrai écoulement d'air tridimensionnel dans une cavité cubique. Comme pour les résultats de l'étude numérique, c'est l'algorithme de mesure utilisant la correspondance spatiale épipolaire, puis une corrélation croisée avec suivi 2D et une reconstruction 3D (algorithme II(B)), qui donne la plus grande longueur de suivi de la trajectoire moyenne des particules parmi tous les algorithmes testés.

Les résultats de l'évaluation suggèrent que différents algorithmes de mesure présentent des avantages et des inconvénients différents, en fonction de l'application demandée, et que les algorithmes utilisant la contrainte épipolaire comme méthode de correspondance spatiale ont généralement de meilleures performances.

Ce chapitre est basé sur l'article de revue:

Sijie Fu, Pascal Henry Biwole, Christian Mathis, Philippe Maïssa. Numerical and experimental comparison of complete 3D Particle Tracking Velocimetry (PTV) algorithms for indoor airflow study. *Indoor and Built Environment*, *in press*, 2016.

Numerical and Experimental Comparison of Complete Three-dimensional Particle Tracking Velocimetry (PTV) algorithms for Indoor Airflow Study

Sijie Fu, Pascal Henry Biwole, Christian Mathis, Philippe Maïssa, 2016. Indoor and Built Environment, *in press*.

Abstract

The experimental data retrieved from three-dimensional Particle Tracking Velocimetry (3D PTV) are crucial for indoor environment engineering when designing ventilation strategies or monitoring airborne pollutants dispersion in inhabited spaces as well as in livestock compounds. The performance of the measurement algorithm, as the core part of the 3D PTV technology, has a strong influence on the final results. This study presents a method to select the better 3D PTV algorithm depending on the application targeted. This study first compared the performance of seven 3D PTV algorithms on two types of three-dimensional laminar macro scale flows of known Navier-Stokes solutions, namely the Kovasznay and Beltrami flows. The comparison was based on the accuracy, the measuring volume coverage, and the achievable trajectory length of each algorithm with respect to the particle tracking density and the total number of frames. Then, the measurement algorithms with better performances were further compared with the experimental measurement of real three-dimensional airflows in a cubic cavity. The results suggest that different measurement algorithms have different advantages and drawbacks depending on the application targeted, and that the algorithms using the epipolar constraint as the method of spatial matching generally perform better.

Keywords: 3D Particle Tracking Velocimetry (3D PTV), comparison, algorithm, tracking density

1. Introduction

With the development of computer technology, Computational Fluid Dynamics (CFD) has been widely applied to indoor airflow study. [11]. However, a reliable CFD simulation usually needs to be validated by abundant experiment data, and experiments are also indispensable to study and show qualitative and quantitative characteristics of indoor airflows. Therefore, many relevant experiments have been conducted using different modern measurement methods. However, it is not trivial to make reliable measurements when the airflow is unsteady and turbulent, and it is more difficult to do in a large, three-dimensional (3D) space, which is the general scale of indoor airflow.

Sun and Zhang [13] summarized main modern methods for airflow measurements. These methods can generally be divided into two types: point-wise technology and globe-wise technology. The point-wise technology, such as Hot-wire/film/sphere Anemometry (HWA/HFA/HSA), Ultrasonic Anemometry (UA) and Laser Doppler Anemometry (LDA), has been widely applied in airflow studies. However, the disadvantage of the point-wise technology is that the measurement tools are usually intrusive, which causes disturbance of the local airflow. The globe-wise technology, including Particle Image Velocimetry (PIV), Particle Streak Velocimetry (PSV) and Particle Tracking Velocimetry (PTV), which utilizes particle tracers and visualization technology, can effectively overcome the shortcomings of the point-wise technology. In recent years, the globe-wise technology, especially the PIV technology, has been extensively applied in airflow studies, with many available commercial PIV systems and open-source analysis software. Cao et al. [14] summarized typical PIV technology and main applications for the indoor airflow field.

However, typical PIV technology currently mainly deals with the two-dimensional measurement domain due to the limitations of lasers and particle tracers under common experimental conditions. Although the Tomographic PIV (TPIV) technology has been applied to capture the unsteady 3D flow structure of convective airflow, the measurement volume is still limited $0.69 \text{ m} \times 0.42 \text{ m} \times 0.24 \text{ m}$. [121]. Li et al. [122] put forward a method to employ PIV technology to measure high-resolution and large coverage airflow data, but the data were still collected in a 2D domain. Compared to the PIV technology, the PTV technology uses less particle tracers, as well as ordinary light sources, to conduct the measurements. Therefore, PTV is more advantageous than PIV to capture the structure of airflow in a large 3D space. In recent years, the PTV technology has been applied successfully in small scale cases. [e.g. 29-31]. Recently, researchers started studying the 3D PTV technology for large-scale airflow measurement, and several complete 3D PTV algorithms and relevant systems have been developed and successfully applied in airflow measurements. [e.g. 46, 69, 75, 118]. Fu et al. [104] reviewed the state-of-the-art PTV technology and its applications for indoor airflow fields.

The present paper evaluates the performance of seven complete 3D PTV algorithms with different core tracking schemes, using numerical methods and experimental tests with air as the working fluid. Most of the algorithms discussed have been employed for large scale indoor airflow study. This study is more focused on comprehensive comparisons.

2. Descriptions of the compared complete 3D particle tracking algorithms

In the PTV technology, as a Lagrangian measurement method, the fluid velocity \vec{v} is obtained through tracking the motion of each independent point (particle tracer), as a result of Eq. (3-6).

$$\vec{v}(x(T), T) = \frac{d\vec{x}}{dT} \quad (3-6)$$

Therefore, the independent point (particle tracer) trajectories can be monitored during the measurement process. More details on the principles of PTV technology can be found in the literature. [e.g. 28, 39].

A complete tracking algorithm for the 3D PTV generally consists of five main steps: multi-camera calibration, image processing, particle centre detection, 2D or 3D tracking and 3D reconstruction. Ouellette et al. [64] reviewed several common tracking algorithm schemes. Among these five main steps, the last three are generally defined as the tracking strategy. Through the function of tracking strategy, the particle trajectories and fluid velocities are finally obtained. The particle tracking strategies may be divided into two types as illustrated in Figure 3-2. The main difference between them is whether the particle temporal tracking is done in 2D (image) plane or 3D (object) domain. Spatial matching can be done before 2D temporal tracking when conducting the temporal tracking in 2D plane, as shown in the left part of Figure 3-2 shows. Besides, some hybrid tracking strategies using features from each type or combining Particle Streak Velocimetry (PSV) technology can be found in the literature. [e.g. 40, 46].

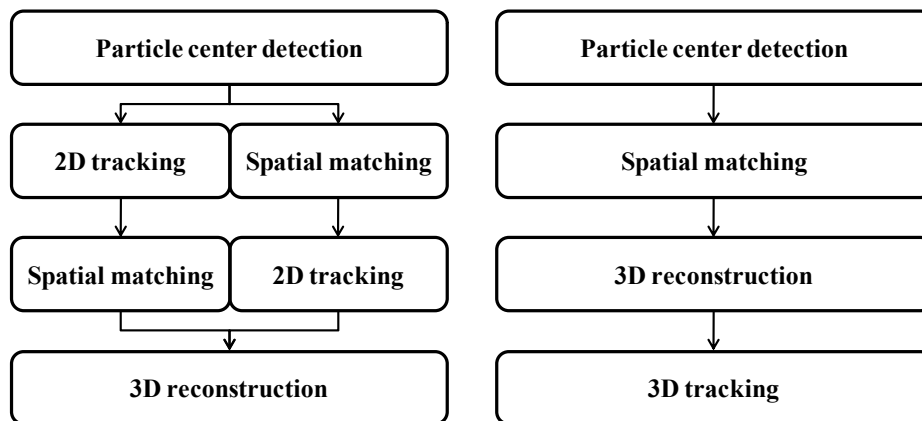


Figure 3-2: Flow chart of main particle tracking strategies

In this study, the performance of seven complete 3D particle tracking algorithms representing the two types of tracking strategies were compared using numerical simulation, and the algorithms with better performance were further applied in experimental tests for indoor airflow study. Two types of spatial matching algorithms and four different temporal tracking algorithms were used to generate the difference between these seven complete 3D particle tracking algorithms. The methods for multi-camera calibration, image processing,

particle centre detection and 3D reconstruction were the same for all algorithms.

2.1 Multi-camera calibration

In 3D PTV measurements, multi-camera calibration is indispensable to establish the mathematical relationship between each camera's 2D pixel (image) coordinates and a physical 3D reference frame. The intrinsic and extrinsic parameters of the cameras, including focal length, principal point, skew angle, distortion coefficients and rotation and translation matrices between each camera reference frame and the physical 3D reference frame, can be accessed through this step. Those calibration parameters are obtained through the minimization of the re-projection error between the known 3D coordinates of the calibration target, and the same coordinates calculated via a mathematical camera model. In this study, the calibration method proposed by Zhang [66] was employed. The calibration target should be large enough to allow the detection of its specific points by the cameras. A checkerboard calibration target consisting of $30\text{ mm} \times 30\text{ mm}$ squares, as shown in Figure 3-3, was used in this study to obtain the calibration parameters. This target can be moved so that each camera can view it from different angles, and the in-depth coordinate is derived from the in-plane coordinates by trihedral projection.



Figure 3-3: Calibration target

2.2 Image processing

The aim of image processing is to subtract the background and noise from the raw images so that the particle detection can be done as accurately as possible. Because this procedure highly depends on the contrast between the illuminated particles and the background, when the contrast of the background to the particle images is poor, a high pass filter may be applied by the use of a threshold value setting to zero all pixel values lower than the threshold. In order to eliminate the single-pixel noises, the erosion by structuring elements of the form $[1, 1]$ and $[1, 1]^T$ can also be used.

In this study, since synthetic images were employed in the numerical simulation, the image processing procedure would not be needed. For the experimental tests, the method introduced in Biwole et al. [118] was employed for image processing.

2.3 Particle center detection

For particle centre detection, although the Gaussian fitting and neural network methods may be more accurate than the weight average method [64], the former are usually computationally costly. Therefore, in this study, the weight averaged method was adopted to calculate particle centres because of its easy implementation, and its rapid and effective computation. [118]. Using the weight average method, the coordinates (x_c, y_c) of the centre of mass of each particle are given by Eq. (3-7) [64]:

$$x_c = \frac{\sum x_{cam} I(x_{cam}, y_{cam})}{\sum I(x_{cam}, y_{cam})}; \quad y_c = \frac{\sum y_{cam} I(x_{cam}, y_{cam})}{\sum I(x_{cam}, y_{cam})} \quad (3-7)$$

where (x_{cam}, y_{cam}) are the pixel coordinates of each pixel belonging to the particle and $I(x_{cam}, y_{cam})$ is the pixel luminance.

2.4 Spatial matching and 3D reconstruction

Spatial matching and 3D reconstruction are used to obtain the particle trajectories and fluid velocity in real 3D world view.

2.4.1 Spatial matching

The aim of spatial matching is to identify a particular particle or a particle trajectory among hundreds of similar particles in a measured area viewed by multiple cameras at the same time. This is a necessary step for 3D reconstruction. Two methods of spatial matching were used in this study. One was based on the comparison of particles' 3D coordinates calculated by two cameras at a time [45], hereafter denoted method "A", and the other used the epipolar constraint [117], hereafter denoted method "B".

2.4.1.1 Calculating the 3D coordinates (method A)

The principle of spatial matching by calculating the 3D coordinates is illustrated in Figure 3-4. The real world 3D coordinates of particles are calculated by triangulation using all particle centre pixel coordinates, hereafter called centroids, from a couple of cameras at a time. If the 3D coordinates from centroids (1, 3) are 'similar' to those calculated from another couple of centroids (1, 5), then centroids 3, 1 and 5 are images of the same particle. The minimum of Euclidian distance among every other 3D coordinates, as described in Eq. (3-8), is used as the similarity criterion.

$$\min_{i,j} (\|A_i - B_j\|) = \min_{i,j} (\sqrt{|x_a - x_b|^2 + |y_a - y_b|^2 + |z_a - z_b|^2}) \quad (3-8)$$

where $A_i(x_a, y_a, z_a)$ and $B_j(x_b, y_b, z_b)$ are two real world's coordinates, and $\|$ is the 2-norm. More details about this type of spatial matching can be found in Biwole et al. [27].

<i>Centroids in camera 2 view</i>	<i>Centroids in camera 1 view</i>	<i>Centroids in camera 3 view</i>
1	1	1
2	2	2
3	3	3
4	4	4
5	5	5

Figure 3-4: Illustration of the identification algorithm for spatial matching [123]

The main drawback of this method is that it requires the measuring volume to be seen by at least three cameras at the same time. When using this method for spatial matching, the remaining unmatched particles are usually discarded since those particles cannot be recorded by all three cameras. When used in this study, this method was followed by the next procedural method described in the following section in order to match more particles.

2.4.1.2 Using the epipolar constraint (method B)

The fundamental matrix of each pair of cameras i and j is first calculated as given by Eq. (3-9):

$$F_{ij} = [T_i - R_i \cdot R_j^T \cdot T_j]_{\times} R_i \cdot R_j^T \quad (3-9)$$

where T and R are, respectively, the 3×1 translation vector and the 3×3 rotation vector which transform camera i 3D coordinates system XX_{Ci} into the calibration target 3D coordinates system XX , as described in Eq. (3-10):

$$XX_{C_i} = R_i \cdot XX + T_i \quad (3-10)$$

Matrices R_i , R_j , T_i , and T_j are extrinsic parameters given by the multi-camera calibration step. The cross-product $[]_{\times}$ is defined by Eq. (3-11) as:

$$[u]_{\times} = \begin{pmatrix} 0 & -u_k & u_j \\ u_k & 0 & -u_i \\ -u_j & u_i & 0 \end{pmatrix} \quad (3-11)$$

Let (x_i, y_i) and (x_j, y_j) be the normalized pixel coordinates from each camera, t an instant time, and s a threshold value which was given the value 1 in numerical study. If (x_i, y_i) and (x_j, y_j) satisfy Eq. (3-12), it means that the particle is matched at this instant time.

$$[x_i^t \quad y_i^t \quad 1] F_{ij} \begin{bmatrix} x_j^t \\ y_j^t \\ 1 \end{bmatrix} < s \quad (3-12)$$

2.4.2 Three-dimensional reconstruction

3D reconstruction is the final step to find 3D coordinates of a point from multiple 2D views. The least squares method as described in the literature [118] was employed in this study. This method was proved to be more straightforward than the methods proposed by Bouguet [124] and Svoboda et al. [68], with similar precision [45]. The least square method does not need to choose a reference camera as in Bouguet's method, and is not limited to processing two cameras at a time [45].

2.5 Temporal tracking algorithms

Temporal tracking is the core part in the tracking algorithms; it directly indicates the correctness of the final results. In general, temporal tracking can be done in 2D image plane or in 3D object domain. In this study, four different temporal tracking algorithms associated to the 2D and the 3D tracking schemes were used.

Algorithm I: The first scheme is the algorithm proposed by Li et al. [81]. In this algorithm, the tracking is first done in 2D image plane and it utilizes a second-order polynomial regression method to predict the centre of search region, as given by Eq. (3-13) illustrates:

$$x_{pre} = at^2 + bt + c \quad (3-13)$$

where x_{pre} is the pixel coordinates vector at the instant time (frame) t . The 2×1 constant vectors a , b and c are acquired by least-square fitting. In order to solve the conflicts within the search area, a cost function, Eq. (3-14), is applied:

$$\phi = \frac{\sqrt{\sum_{k=0}^3 |D_k - G\tau_k - H|^2}}{\sqrt{\sum_{k=0}^3 |D_k|^2}} \quad (3-14)$$

where D_k is the previous linked trajectory displacement between frames k and $k+1$, τ_k is the middle times between frames k and $k+1$, and G and H are the 2×1 constant vectors resulting from the linear regression of order 1 fitting D_k over frames 0 to 3, as given by Eq. (3-15):

$$D_k \approx G\tau_k + H \quad (3-15)$$

Algorithm II: Proposed by Biwole [45], the second algorithm employed uses a modified fast normalized cross-correlation given by Eq. (3-16) [116], for 2D temporal tracking.

$$\gamma(u, v) = \frac{\sum_{x,y} [f(x, y) - \bar{f}_{u,v}] [t(x-u, y-v) - \bar{t}]}{\sqrt{\sum_{x,y} [f(x, y) - \bar{f}_{u,v}]^2 \sum_{x,y} [t(x-u, y-v) - \bar{t}]^2}} \quad (3-16)$$

where f is the research window, \bar{t} is the mean of the template (interrogation window) and $\bar{f}_{u,v}$ is the mean of $f(x, y)$ in the template region. Here, the searching pattern consists of

each single particle instead of a group of particles as in traditional PIV. When there is more than one correlation peak, a procedure by the Lagrangian extrapolation of an estimate position using the last two or three positions of the particle is applied, following the same form as Equation (8). The particles not linked to the previous frame are used to start new trajectories. When this algorithm was applied, spatial matching was done first, and then temporal tracking was conducted in the 2D image plane.

Algorithm III: The third temporal tracking algorithm conducts the particle tracking in 3D space, based on the algorithm proposed by Barker et al. [49]. This scheme, referred to as the "priority strict" scheme, uses the nearest neighbour method to initialize the particle trajectories between the first two frames, and estimates the particle's position in the new frame using an approximation of velocity through the first order backward difference scheme, as described by Eqs (3-17) and (3-18).

$$x_{pre}^{t+1} = x^t + u^t \Delta T \quad (3-17)$$

$$u^t = \frac{x^t - x^{t-1}}{\Delta T} + O(\Delta T) \quad (3-18)$$

where x_{pre}^{t+1} is the estimate particle's position and u^t its velocity at frame t . Then, a search radius based on the magnitude of velocity multiplied by the time step was calculated. Finally, a cost function minimizing of Eq. (3-19) was applied to find the matched tracked particle position x_{can} .

$$d = \left\| x_{can}^{t+1} - x_{pre}^{t+1} \right\|_2 \quad (3-19)$$

A "cross-gap" strategy was added to the algorithm proposed by Barker [49]. If no particle was found at time t , the polynomial regression method (Eq. (3-13)) was used to link the trajectory to a candidate at time $t+1$. The regression was based on the two or three previous particle positions, from time $t-3$ to $t-1$. If there are three continuous positions which have no optimal particle candidates, this trajectory would be stopped. The particles not linked to previous frames would be identified as new particles, and the nearest method was used to initialize them in the following temporal tracking.

Algorithm IV: The last temporal tracking algorithm is based on the second and the third temporal tracking algorithms. Most PTV algorithms use the nearest neighbour method to initialize the particle trajectory between the first two frames. Algorithm IV employs the modified cross-correlation method proposed by Biwole [45] to initialize the particle trajectory and compare the method performance with the nearest neighbour method. After trajectory initialization, the tracking is done by priority strict matching method.

2.6 Flow chart of the complete 3D particle tracking algorithms

Spatial matching methods A and B were successively used on each base temporal tracking algorithm to produce the seven complete 3D PTV algorithms comparison. The flow chart of these algorithms is presented in Figure 3-5.

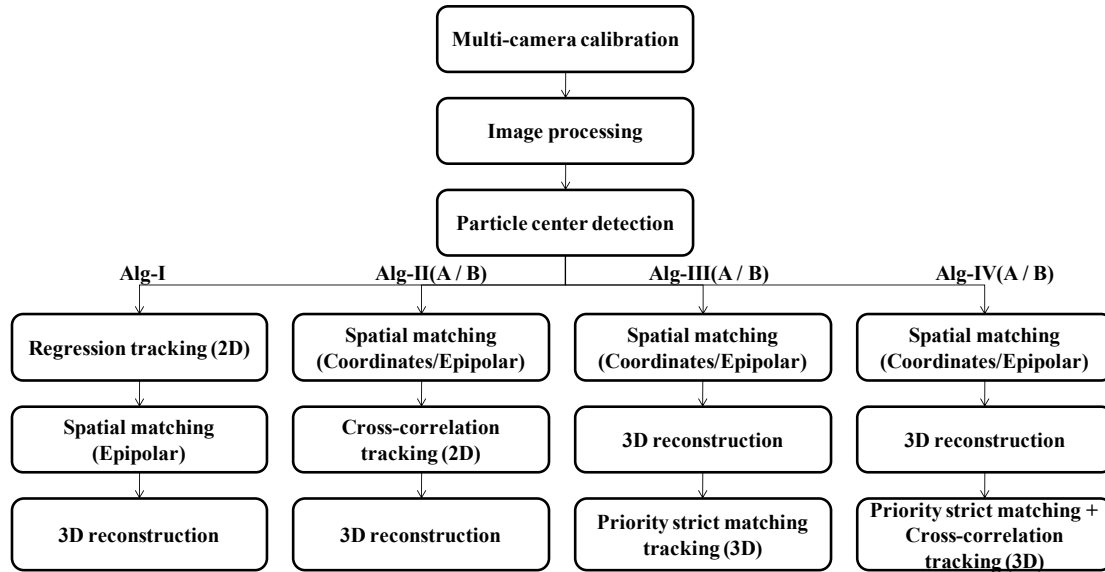


Figure 3-5: Flow chart of the seven complete 3D particle tracking algorithms compared

3. Numerical study

Numerical simulations have been largely employed to evaluate the performances of PTV algorithms [e.g. 46, 75, 81], since they have the advantage of reducing or eliminating the effects of unwanted parameters otherwise present in real experiments. Different synthetic particle images with systematic and precise parameter variations can be generated based on the requirements of the evaluation.

3.1 Synthetic images

In order to evaluate the performance of 3D PTV algorithms, the synthetic images should reflect the particle motion in real-world 3D coordinates. To produce the synthetic particle images used in this study, the multi-camera calibration parameters were first obtained using three real cameras and a real calibration target, based on the method proposed by Zhang [66]. The synthetic particles were generated in a virtual space of dimensions 1000 mm (X) x 1000 mm (Y) x 700 mm (Z), which was a scaled-down dimension of real environmental control chamber.

The camera calibration parameters consisted of intrinsic and extrinsic parameters. The intrinsic parameters were used to define the relationship between the camera's 3D coordinate system and the image pixels for every camera independently, while the extrinsic parameters were used to calculate the relationship between each camera's 3D coordinate system and the common 3D (real world) coordinate system defined by the calibration target. These parameters were employed to project the 3D coordinates of prescribed particles onto the synthetic images. The calibration parameters used are given in the Appendix.

To increase the testing difficulty, three-dimensional coordinates (x, y, z) of a prescribed number of particles, $N_p = 800$, were randomly generated in the three-dimensional virtual volume. Two analytical solutions for incompressible Navier-Stokes equations were applied to

simulate a two dimensional and a three dimensional particle motion in the synthetic images. One is the two dimensional Kovasznay flow [113], where the velocity field is defined by Eq. (3-20) as:

$$\begin{cases} v_x = 1 - \exp(\lambda x) \cos(2\pi y), v_y = \frac{\lambda}{2\pi} \exp(\lambda x) \sin(2\pi y) \\ \lambda = Re/2 - (Re^2/4 + 4\pi^2)^{0.5} \end{cases} \quad (3-20)$$

Here, the Reynolds number Re was set to 40. This analytical solution was originally for a two-dimensional flow field. Because of 3D PTV testing requirements with the need of creating a flow that could fill the whole measuring volume, the initial particle positions were extended to three-dimensional space, with the assumption of zero motion in z-direction.

The other simulated flow is the Beltrami flow [125], which is fully three dimensional. Here, the velocity field is defined by Eq. (3-21) as:

$$\begin{cases} v_x = -a(e^{ax} \sin(ay + dz) + e^{az} \cos(ax + dy)) e^{-d^2vt} \\ v_y = -a(e^{ay} \sin(az + dx) + e^{ax} \cos(ay + dz)) e^{-d^2vt} \\ v_z = -a(e^{az} \sin(ax + dy) + e^{ay} \cos(az + dx)) e^{-d^2vt} \end{cases} \quad (3-21)$$

In this study, $a = \pi/4$, $d = \pi/2$, $v = 0.025$ and $t = 0$. Based on the defined velocity fields, some particles may go out of the prescribed volume. Every time it happens, new particles were added with random positions so that the total number of particles in each synthetic image was 800, which also made the tracking density always the same. Because Equations (15) and (16) are expressed in dimensionless form, special ratios were applied on the original coordinates so that most of particles can stay inside the measuring volume as the tracking density varies. Figure 3-6 shows the schematic of the two types of particle motions. Figure 3-7 gives an example of synthetic images with the Beltrami flow solution from one camera's view.

The final synthetic images were generated using the custom codes written in the MATLAB[®], which were based on the principles described above.

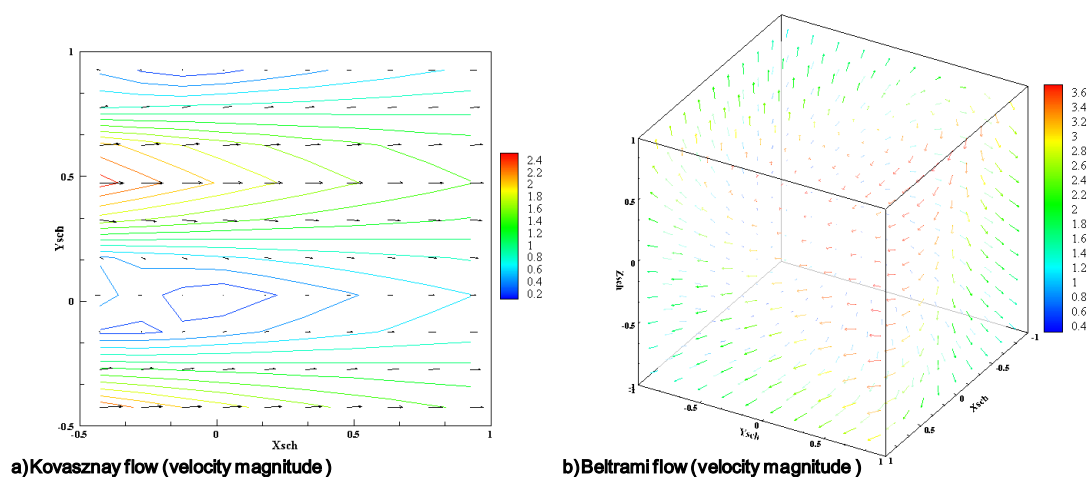


Figure 3-6: The schematic of the two types of particle motions

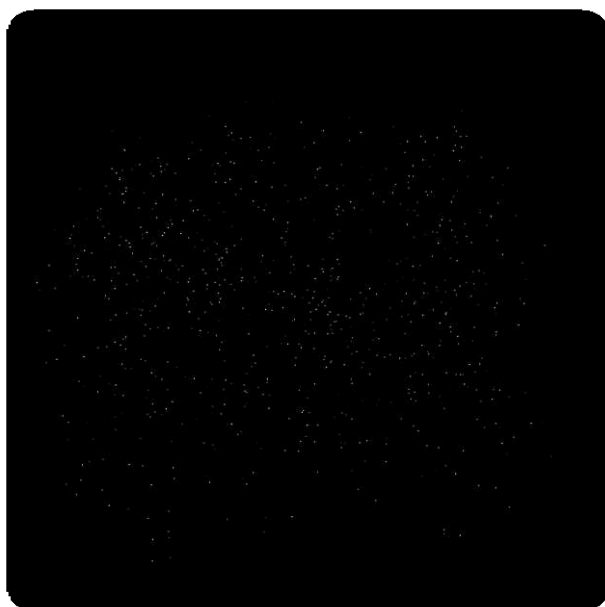


Figure 3-7: An example of synthetic images with Beltrami flow solution from one camera's view

3.2 Results

The performances of the seven complete 3D PTV algorithms were evaluated using two indexes: the "correct tracking ratio (γ_{3D})" [81] and the "total tracking ratio (E_{3D})" [37]. The correct tracking ratio, γ_{3D} , is the number of 3D tracked positions which are identical to input 3D particle positions divided by the total number of tracked positions. The total tracking ratio, E_{3D} , is the number of correctly tracked 3D positions divided by the total number of input 3D positions. Because the tracked particle trajectories have different lengths, the total number of tracked particle positions and input particle positions were used to calculate γ_{3D} and E_{3D} . Rations γ_{3D} and E_{3D} were used to investigate the tracking density and number of tracked frames, which are two important parameters for 3D PTV performance assessment. In addition, the average trajectory length for all correctly tracked particles ($L_{correct}$) was calculated.

3.2.1 The performance based on the tracking density

The “tracking density” index, hereafter noted ξ , is defined as the ratio of the mean particle spacing in a nearest neighbour sense to the mean displacement of particles between two consecutive frames. This index reflects the tracking difficulty; the bigger its value, the easier the tracking. In this study, the performances of the seven complete 3D PTV algorithms on five different tracking densities were investigated with the tracking density varied from 5 to 15. Ten triplets (one image per camera) of time synchronous synthetic images were used as a set to conduct the investigation.

Figures 3-8(a) and 3-8(b) show γ_{3D} and E_{3D} , respectively, for each 3D PTV algorithm on the condition of predefined Kovaszny flow, with no particle motion in z-direction. The algorithm I showed the best γ_{3D} , meaning that it provided the best tracking accuracy. This algorithm also seemed more robust against tracking density variations since its γ_{3D} varied only slightly with respect to ξ . Algorithm III (B) was the second best in terms of γ_{3D} . The γ_{3D} values of other algorithms increased with ξ , meaning that those algorithms would be more accurate for applications with large ξ .

Algorithm III (B) yielded the best E_{3D} among all algorithms, and its E_{3D} value stayed nearly stable as the tracking density varied. It means that this algorithm had a better “coverage” of the measuring volume since more particles trajectories were correctly tracked over ten frames. Other algorithms showed an increased E_{3D} as the tracking density increased, except for algorithm I. The E_{3D} of algorithm I declined correspondingly as the tracking density is increased, meaning that algorithm I can better track larger particle displacement at constant particle spacing. The γ_{3D} and E_{3D} of algorithms III (A) and IV (A) decreased when the tracking density varied from 12.5 to 15, suggesting that these two algorithms were not suitable for tracking very small particle displacements. Generally, the algorithms using the epipolar constraint for spatial matching gave better γ_{3D} and E_{3D} .

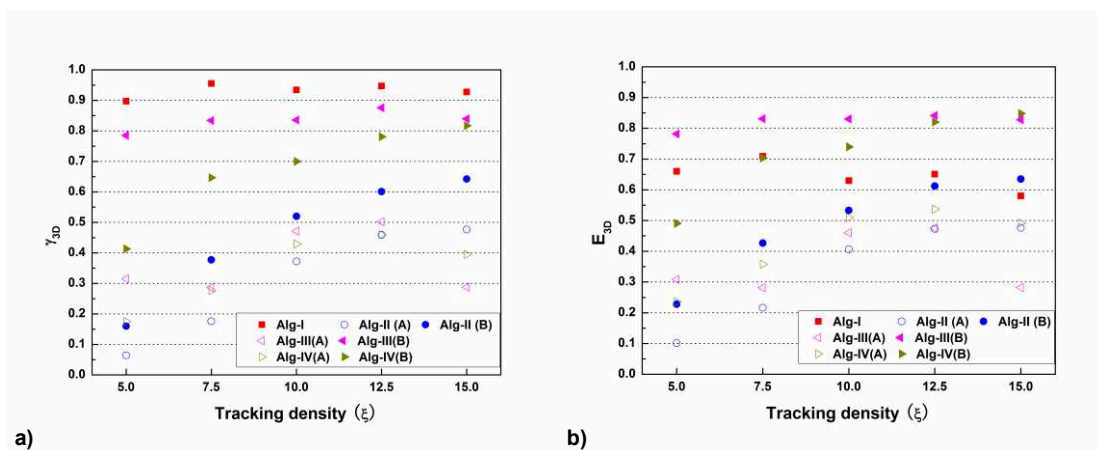


Figure 3-8: γ_{3D} (a) and E_{3D} (b) of different 3D PTV algorithms performing on Kovaszny flow motion with respect to the tracking density

The γ_{3D} and E_{3D} of the seven complete 3D PTV algorithms on the condition of predefined

Beltrami flow motion, which has particle motion in all three directions, are shown in Figure 3-9. The results were similar to those for the Kovaszny flow motion.

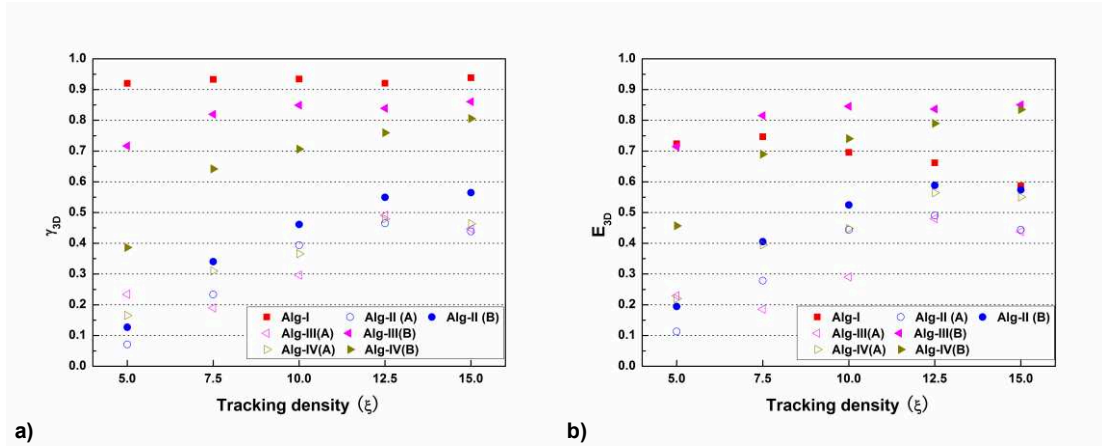


Figure 3-9: γ_{3D} (a) and E_{3D} (b) of different 3D PTV algorithms performing on Beltrami flow motion with respect to the tracking density

Figures 3-10(a) and 3-10(b) show the average trajectory length for all correctly tracked particles, $L_{correct}$, for the two predefined conditions when the tracking density varied. For all tracking densities, algorithm II (A) had always the best $L_{correct}$, meaning that it had the best ability to provide longer particle trajectory regardless of its "coverage" capability. Algorithm IV (A) always gave the worst $L_{correct}$. The $L_{correct}$ of algorithm I always exceeded 8 since at least 6 frames were needed to validate the spatial matching of a trajectory (performed as in Equation (7)), as explained in Biwole et al. [118]. Here again, the algorithms using the epipolar constraint as the method of spatial matching generally yielded better $L_{correct}$.

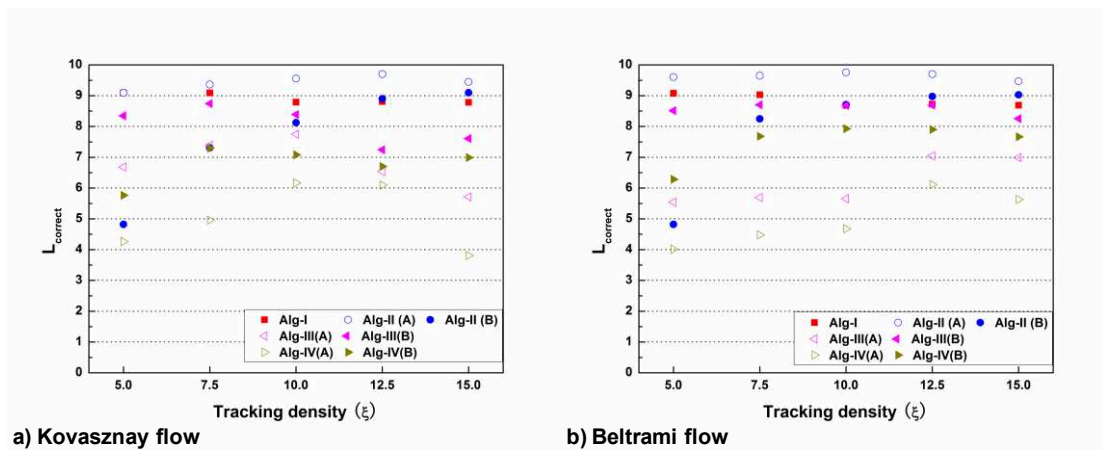


Figure 3-10: $L_{correct}$ of different 3D PTV algorithms performing on Kovaszny flow motion (a) and Beltrami flow motion (b) with respect to the tracking density

3.2.2 The performance based on the number of frames

As a Lagrangian measurement method, the main characteristic of 3D PTV is its ability to

provide particle trajectories. Therefore, the total number of frames also has an influence on the performance of the algorithms. In this study, the performance of different algorithms was investigated using 60 synthetic images as a set, and the tracking density was set to 10.

For the two predefined fluid motion conditions, Figures 3-11 and 3-12 show γ_{3D} and E_{3D} for the seven complete 3D PTV algorithms with respect to the number of frames. The results clearly indicate that the γ_{3D} and E_{3D} of all algorithms decreased as the number of frames increased. For the condition of Kovaszny flow motion, algorithms III (B) and IV (B) showed better γ_{3D} and E_{3D} than others; their γ_{3D} and E_{3D} were always greater than 0.5 as the number of tracked frames increased. For the Beltrami flow motion, algorithms I, III (B) and IV (B) showed better performances than others. Among these three algorithms, algorithm III (B) had the largest decrease for γ_{3D} and E_{3D} as the number of tracked frame increased, meaning that algorithm III (B) was less suited for longer trajectories. The results suggest that, whatever the algorithm, the number of tracked frame should be limited in order to obtain accurate results. It also clearly suggests that reinitializing the tracking after a limited and predefined number of frames may improve the accuracy of any 3D PTV algorithm.

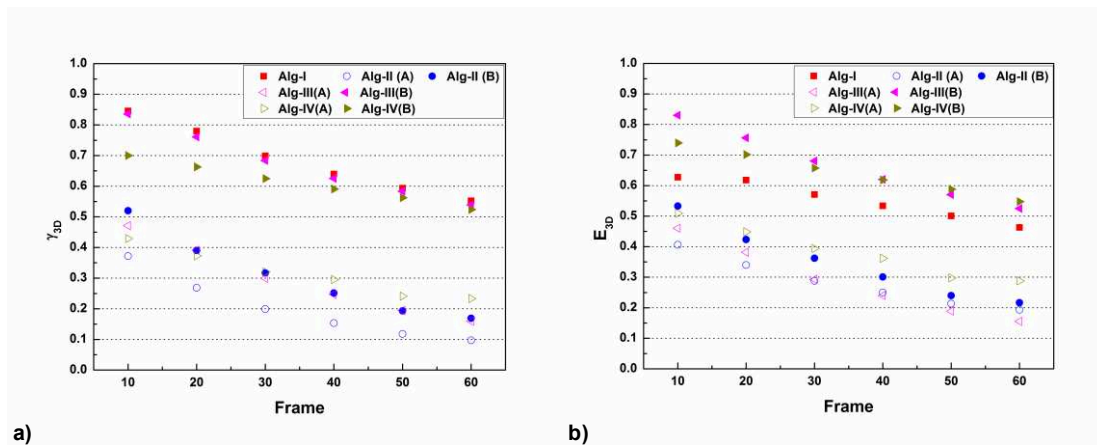


Figure 3-11: γ_{3D} (a) and E_{3D} (b) of different algorithms performing on Kovaszny flow motion with respect to the number of tracked frames

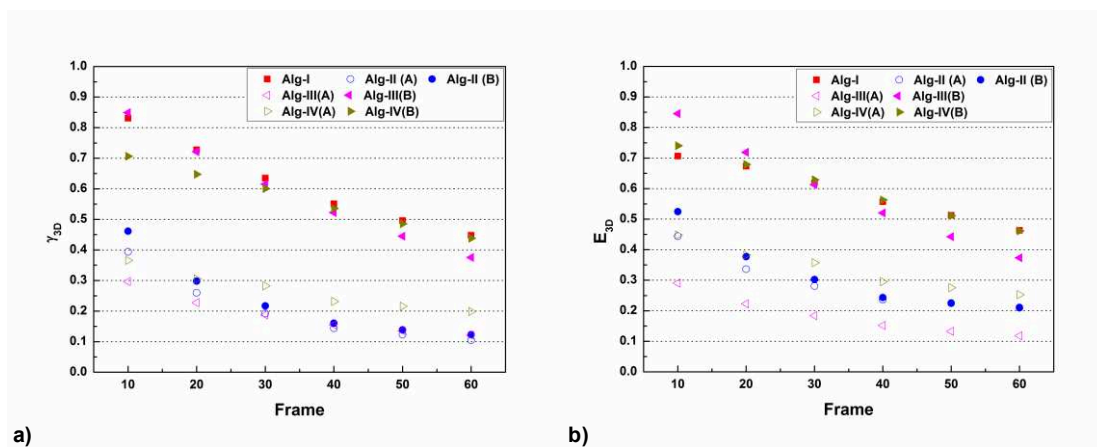


Figure 3-12: γ_{3D} (a) and E_{3D} (b) of different algorithms performing on Beltrami flow motion with respect to the number of tracked frames

Figures 3-13(a) and 3-13(b) show the L_{correct} of the different algorithms for the two predefined conditions with respect to the number of frames. Among all algorithms, algorithm II (A) always gave the best L_{correct} , which is consistent with the result found regarding the same algorithm. Note that, although the L_{correct} increased as the tracked frame increased, the performance of all algorithms actually decreased, as shown by the results of γ_{3D} and E_{3D} .

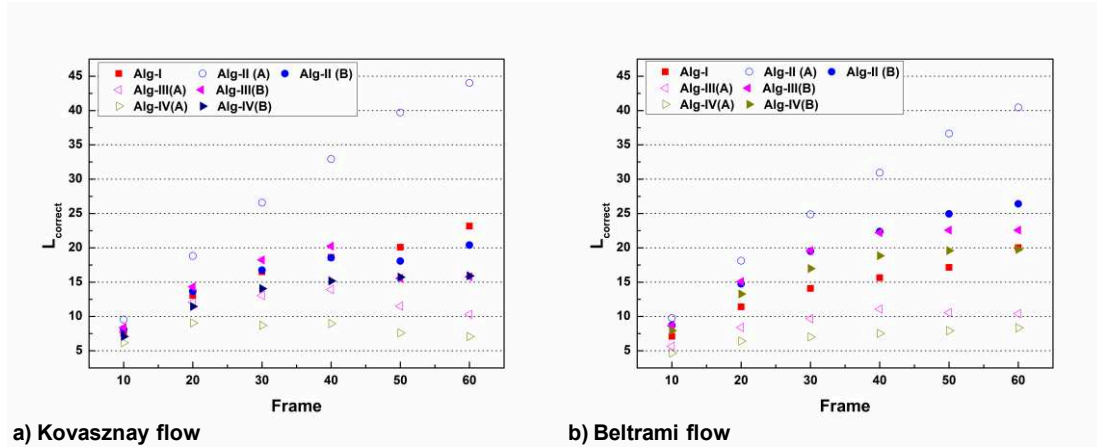


Figure 3-13: L_{correct} of different 3D PTV algorithms performing on Kovaszny flow motion (a) and Beltrami flow motion (b) with respect to the tracked frame

3.2.3 Summary

From the results obtained in numerical analysis, we can conclude that the performance of all algorithms presented in this paper is significantly affected by the tracking density and number of tracked frames. For the tracking density, the algorithms generally have better performance as the tracking density increases, except algorithm I. Algorithm I has better robustness against the variations of tracking density. For the number of tracked frames, the performance of all algorithms decreases as the number of tracking frames increases. Algorithm II (A) has a better ability to provide long particle trajectories, but would not guarantee a good tracking accuracy and "coverage" of the measuring volume. When the epipolar constraint is applied for spatial matching, the algorithms generally show better performance.

3.2.4 Further experimental tests of airflow using Plexiglas cuboid cavity

Based on the results presented in numerical part, algorithms I, II (B), III (B) and IV (B) were further evaluated in experimental tests for indoor airflow, due to their relative better performances.

The test facility was a Plexiglas cuboid cavity of dimensions 1.013 m (L) \times 1.013 m (W) \times 0.73 m (H). A forced airflow was injected into the test facility from a hole of diameter 0.073 m onto the centre of the upper plate (ceiling) using a thermally insulated ventilation pipe. The average velocity of inlet air was 0.51 m/s, and the air temperature difference between the inlet and inside test facility was less than 1°C. The average temperature of the test facility stayed

around 22°C. The 3D PTV measurement system included three Dalsa 4M60 cameras set at 2048×2048 pixels resolution and 30 fps (frames per second) each. The exposure time of the complementary metal–oxide–semiconductor (CMOS) chip was set at 1.5 ms on each camera. Each camera was equipped with a 15 mm Canon lens with a f/4.8 aperture. Illumination was provided by two 1000 W compact fluorescent Balcar Quadlite lamps. Helium-filled soap bubbles [93] were selected as the particle tracers, and were injected into the test facility from a secondary hole in the air inlet pipe. The camera calibration target consisted of a planar checkerboard composed of black and white 30 mm squares. The checkerboard had 13 horizontal squares and 8 vertical squares as shown in Figure 3-3. Figure 3-14 shows the experimental mock-up, and Figure 3-15 shows the experimental test cavity and generation machine for particle tracers.

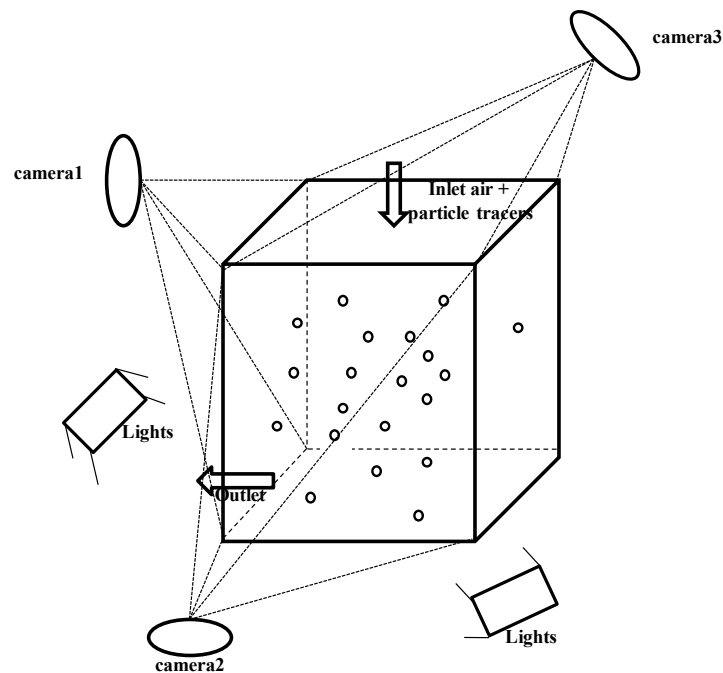
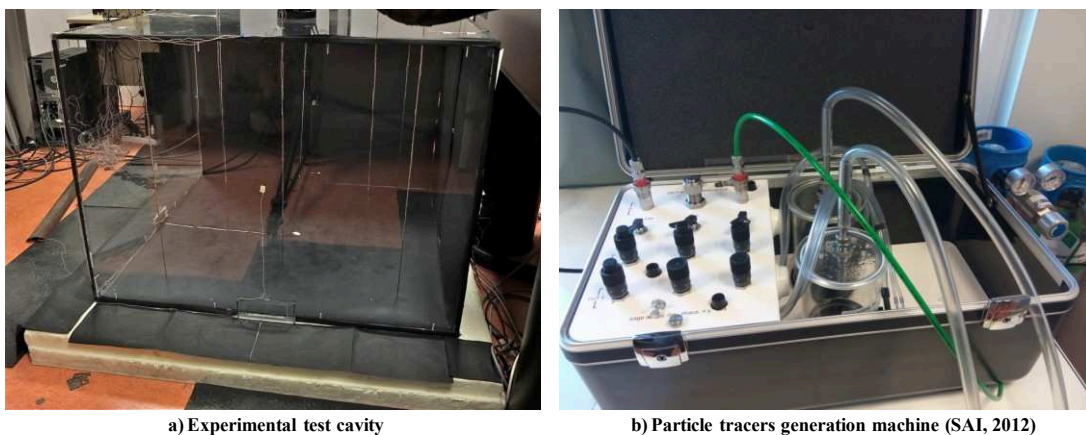


Figure 3-14: The mock-up of experimental set-up



a) Experimental test cavity

b) Particle tracers generation machine (SAI, 2012)

Figure 3-15: The relevant facility of experimental set-up

The merger of the particle tracers into the main flow of the inlet air could affect the airflow velocity. In order to eliminate this effect, the measurement started at least 30 seconds after the

particle generation was stopped. The recording time was 1s and, thus, 30 images were recorded in the measurement process and further analyzed. In order to obtain more particle trajectories, the number of positions needed to match two trajectories (Equation (7)) was set to 2 for algorithm I. The tracking densities calculated for each camera based on the first two frames are listed in Table 3-1. Because algorithm II (B) was applied to initialize the first two frames of algorithm IV (B), algorithms IV (B) and II (B) have the same tracking density.

Table 3-1: Tracking density calculated for each camera with respect to four tracking algorithms

	Alg-I	Alg-II(B)	Alg-III(B)	Alg-IV(B)
Camera 1	9.44	8.17	10.10	8.17
Camera 2	8.01	5.62	8.44	5.62
Camera 3	8.50	5.91	19.10	5.91

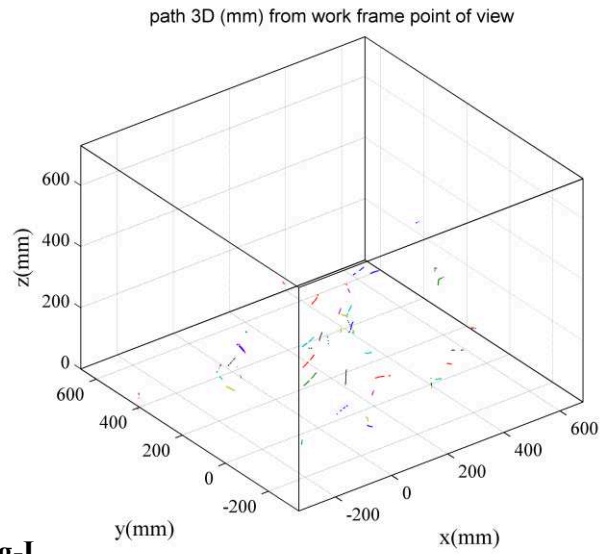
The magnitude of the measured average velocity is defined as the average of all particle velocity magnitude throughout the recording time and the measured magnitudes for the four algorithms are shown in Table 3-2. Table 3-3 shows the average values of the tracked particle trajectory length (minimum length is 2) using the four algorithms. As suggested by the numerical study, the experiment confirmed that PTV algorithm II (B) can track longer particle trajectories than other algorithms, regardless of its tracking accuracy and coverage. Figure 3-16 shows the particle trajectories for the four algorithms with the length of 30 for algorithm II(B) and 10 for other three algorithms.

Table 3-2: Measured average velocity magnitude for the four algorithms evaluated (m/s)

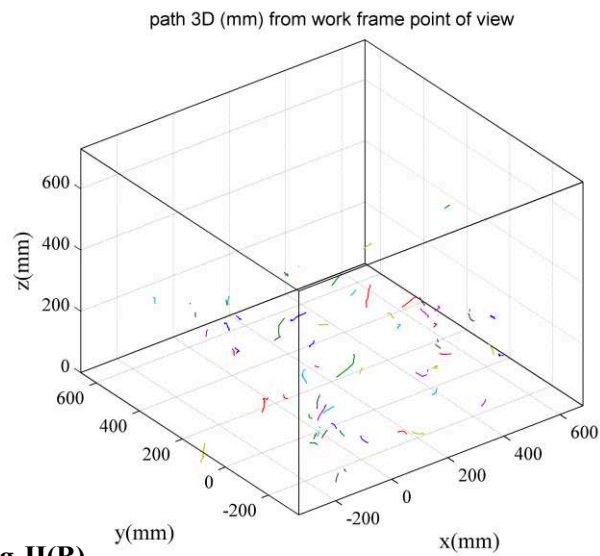
Alg-I	Alg-II(B)	Alg-III(B)	Alg-IV(B)
0.059 m/s	0.050 m/s	0.061 m/s	0.064 m/s

Table 3-3: Average length of tracked particle trajectory (number of linked frames)

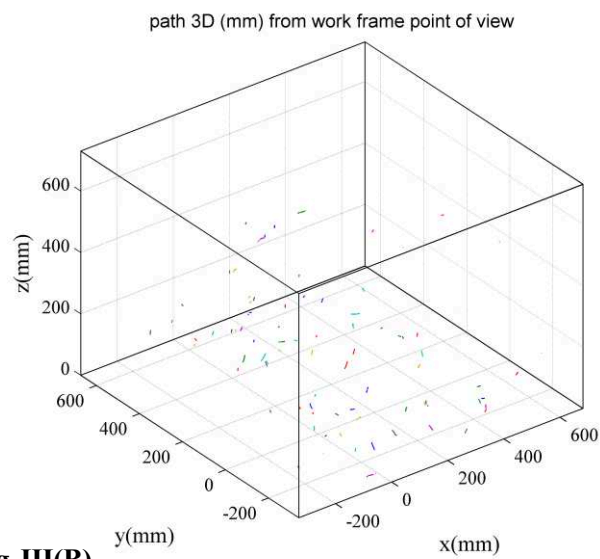
Alg-I	Alg-II(B)	Alg-III(B)	Alg-IV(B)
4.19	21.61	3.10	2.39



a)Alg-I



b)Alg-II(B)



c)Alg-III(B)

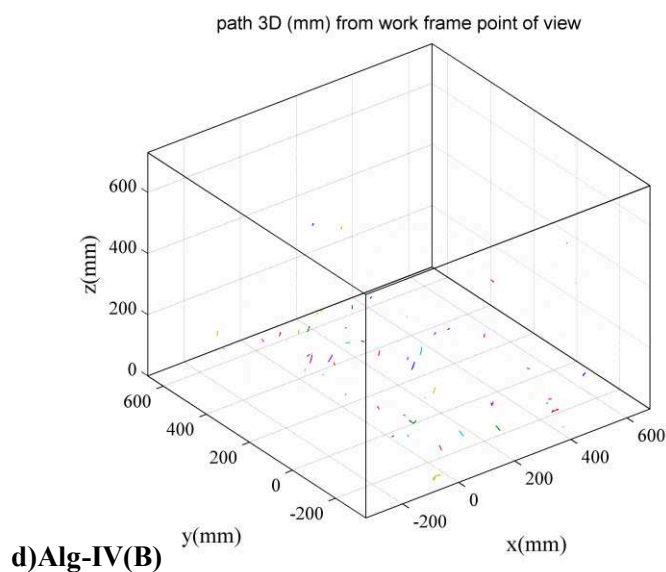


Figure 3-16: The particle trajectories which the length is bigger than 10 using four algorithms

4. Discussions

This study focuses on the performance evaluation of complete 3D PTV measurement algorithms for macro laminar flows. The authors believe that the results presented here can be extended to the low speed, weak turbulent airflows which could be developed in the main central area of most rooms, away from walls and ventilations nozzles. The conclusions can also be extended to natural and mixed convection indoor airflows provided that the pressure gradients remain small.

Based on the performances of the algorithms, our suggestions on selecting the most suitable 3D PTV measurement algorithm are as follows. For local airflow, the modified cross correlation algorithm may be the better choice because it can generate longer trajectories and has better accuracy for small scale domain; therefore, more details of the airflow structure can be shown. For global airflow, the polynomial regression algorithm may be a better choice due to its good accuracy for the large scale domain along with its better space coverage. In any case, the tracking density index should be evaluated prior to choosing the appropriate tracking algorithm. It is also noted that all tested algorithms give good results provided that the tracking density index is suitable.

The results presented in this paper are also dependent on the type of tracers used. While our numerical results are not affected since synthetic particles are used, the ability of different algorithms to accurately detect the particle centres is of great importance in real experimental environment. This effect was not tested here since all methods tested used helium filled bubbles as tracer particles and the same particle centre calculation method was used.

5. Conclusions

A comparative study of results with seven different complete 3D PTV measurement

algorithms, using numerical and experimental data, has been presented. In the numerical analysis, two types of flow based on the analytic solution of incompressible Navier-Stokes equation were generated. The resulting algorithms' accuracy, measuring volume coverage, and achievable trajectory length with respect to particle tracking density and number of frames have been shown and discussed. The results from the numerical tests show that the performance of all 3D PTV algorithms increases as the particle tracking density increases, except for the measurement algorithm I, which exhibits the opposite trend, meaning that this algorithm is best suited to track larger particle displacements at constant particle spacing.

As the number of tracked frames increases, the performance of all measurement algorithms is clearly decreased; suggesting that dividing the total number of frames into sets of smaller number of frames and reinitializing the tracking on each set may improve the accuracy of any 3D PTV algorithm. The algorithms employing the epipolar constraint as the spatial matching method generally have better performance. Besides, the results also suggest that the algorithms with the ability to provide longer particle trajectory have not necessarily the better tracking accuracy.

The four measurement algorithms showing the better performances in the numerical analysis have been used for experimental evaluation. Similar to the results of the numerical study, the measurement algorithm using epipolar spatial matching, then cross-correlation 2D tracking and 3D reconstruction (algorithm II (B)) give the longest average tracked length of particle trajectory among all four algorithms.

Acknowledgment

This work was supported by a grant from the French Region Provence Alpes Côte d'Azur and by funding from the French National Research Agency (ANR) through the FLUBAT project (ANR-12-VBDU-0010). The authors would like to thank Prof. Yuanhui Zhang from the University of Illinois at Urbana-Champaign, USA, for providing the source code of Algorithm I.

Appendix

Table 3-4: Calibration parameters of camera 1

Intrinsic parameters				
Focal length	Principal point	Skew	Distortion	Pixel error
			[0.56581	
[3254.20221	[984.75249	0.00000	-2.96001	[0.43443
3370.98143]	1395.93332]		0.09557	1.03488]
			-0.00211	
			0.00000]	
Extrinsic parameters				
Translation vector	Rotation vector	Rotation matrix(3 × 3)		Pixel error
		[0.99882 -0.02554		
		-0.04127;		
[-172.91993	[2.27495	-0.04798 -0.64719		[0.29193
102.52103	-0.05078	-0.76082;		0.64159]
2248.63226]	-0.03353]	-0.00728 0.76190		
		-0.64765]		

Table 3-5: Calibration parameters of camera 2

Intrinsic parameters				
Focal length	Principal point	Skew	Distortion	Pixel error
			[-0.09699	
[3114.66790	[1109.73767	0.00000	6.15835	[0.39295
3093.18640]	1112.65138]		0.01521	0.33173]
			0.00999	
			0.00000]	
Extrinsic parameters				
Translation vector	Rotation vector	Rotation matrix(3 × 3)		Pixel error
		[0.09371 0.99424		
		0.05206;		
[-265.25152	[1.34453	0.17185 0.03535		[0.33910
229.43067	1.27893	-0.98449;		0.58164]
2227.47717]	-1.01846]	-0.98066 0.10120		
		-0.16754]		

Table 3-6: Calibration parameters of camera 3

Intrinsic parameters				
Focal length	Principal point	Skew	Distortion	Pixel error
[3040.44157 3079.42068]	[1015.75894 1125.23763]	0.00000	[0.00000 2.74497 0.02272 -0.00564 0.00000]	[0.42857 0.36945]
Extrinsic parameters				
Translation vector	Rotation vector	Rotation matrix(3 × 3)	Pixel error	
[2.42120 37.89761 2313.60707]	[-2.04240 2.02127 -0.07052]	[0.02737 -0.97513 0.21995; -0.98809 0.00695 0.15374; -0.15145 -0.22153 -0.96332]	[0.34408 0.40585]	

4 Etude expérimentale d'écoulements d'air intérieur par vélocimétrie par suivi 3D de particules (PTV)

Résumé en français

Les performances des systèmes de ventilation et de distribution d'air ont une influence directe sur le confort thermique, l'efficacité énergétique et la durabilité des bâtiments modernes. Par conséquent, le développement et l'évaluation des systèmes de ventilation et de distribution d'air est toujours un sujet important pour les chercheurs et ingénieurs en CVC (Chauffage, Ventilation et Climatisation). A l'heure actuelle, parmi les méthodes d'évaluation des performances des systèmes CVC, les méthodes CFD (Computational Fluid Dynamics) sont les plus appliquées, avec environ 70% des études réalisées, en raison de leur caractère relativement facile d'accès et peu onéreux. Mais, une simulation CFD fiable doit généralement être validée par des données expérimentales abondantes. Par conséquent, la mesure expérimentale tient encore un rôle important pour l'étude et la compréhension des écoulements d'air intérieur. Par la mesure expérimentale, les caractéristiques de l'air intérieur peuvent être mieux comprises.

Dans des études précédentes, la mesure expérimentale des écoulements d'air intérieur emploie généralement des technologies donnant une information locale, telles que les sondes à fil/film/sphère chaude ou l'anémométrie Laser Doppler (LDA). En plus d'être locales, ces méthodes sont généralement intrusives, ce qui peut perturber l'écoulement d'air local. La vélocimétrie par images de particules (PIV), a été largement appliquée pour l'étude de l'air intérieur en tant que méthode globale, cependant, en raison des limites de l'éclairage laser et des traceurs, le domaine de mesure est généralement bidimensionnel ou tridimensionnel à petite échelle, et les trajectoires des écoulements d'air ne peuvent pas être donnés. Ce n'est donc pas nécessairement le choix optimal pour la mesure dans les bâtiments réels.

Dans ce chapitre, la technologie 3D PTV est employée comme outil de mesure de vitesses et trajectoires d'écoulement d'air intérieur générés par la méthode de ventilation par mélange, méthode la plus appliquée en ventilation mécanique. Les mesures expérimentales sont faites pour des jets isothermes, anisothermes, et en présence d'une source de chaleur. Pendant le processus de mesure, sur la base des analyses présentées dans les chapitres précédents, deux stratégies de mesure 3D PTV sont utilisées, à savoir le suivi temporel par régression polynômiale et le suivi temporel par corrélation croisée modifiée. Les principales expressions de ces deux méthodes sont représentées par les équations (4-1) et (4-2) respectivement.

$$x_{pre} = at^2 + bt + c \quad (4-1)$$

Où x_{pre} est le vecteur des coordonnées pixel à l'instant (image) t . Les vecteurs (2×1) constants a , b et c sont acquis par ajustement en utilisant la technique des moindres carrés.

$$\gamma(u, v) = \frac{\sum_{x,y} [f(x, y) - \bar{f}_{u,v}] [t(x-u, y-v) - \bar{t}]}{\sqrt{\sum_{x,y} [f(x, y) - \bar{f}_{u,v}]^2 \sum_{x,y} [t(x-u, y-v) - \bar{t}]^2}} \quad (4-2)$$

Où f est la fenêtre de recherche, \bar{t} est la luminance moyenne du motif (fenêtre d'interrogation) et $\bar{f}_{u,v}$ est la valeur moyenne de $f(x, y)$ dans la région sous le motif. Ici, l'objet consiste en chaque particule unique au lieu d'un groupe de particules comme c'est le cas pour la PIV traditionnelle.

Grâce aux mesures expérimentales, les trajectoires d'écoulement d'air sont obtenues, ce qui permet de refléter la structure de l'écoulement d'air d'un point de vue tridimensionnel. De plus, les informations de vitesse peuvent ensuite être déduites des trajectoires. Afin de générer un benchmark de données expérimentales pour la validation et le développement des modèles CFD, une méthode illustrée Figure 4-1 est proposée et appliquée pour traiter les résultats de mesure obtenus. Par ailleurs, des thermocouples sont employés simultanément comme outils de mesure des températures d'air intérieur pour les jets en condition anisothermes et en présence d'une source de chaleur.

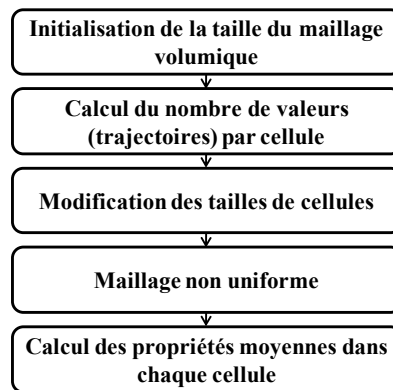


Figure 4-1: Organigramme du post-traitement des résultats de mesure 3D PTV

Ce chapitre est basé sur le preprint:

Sijie Fu, Pascal Henry Biwolé, Christian Mathis. Experimental investigation of indoor airflow distribution using 3D Particle Tracking Velocimetry (PTV).

Experimental Investigation of Indoor Airflow Distribution using 3D Particle Tracking Velocimetry (PTV) Technology

Sijie Fu, Pascal Henry Biwole, Christian Mathis, 2016, *preprint*.

Abstract

Experimental measurement is still indispensable in indoor airflow study, since it can not only help understanding the characteristics of indoor airflow better, but also provide experimental data for validating and developing Computation Fluid Dynamics (CFD) models. In previous studies, numerous experimental measurements have been done with point-wise technology or Particle Image Velocimetry technology, however, the information obtained is usually point-wise or limited to a small volume, due to the limitations of these measurement tools. 3D Particle Tracking Velocimetry technology can overcome these drawbacks, and get three-dimensional information in relatively larger domain scales. Therefore, in this study, 3D PTV technology is employed for measuring the airflow velocity information. Simultaneously, thermocouples are used to measure the airflow temperature. The indoor airflow generated by a mixing ventilation method is investigated under isothermal condition, non-isothermal condition and with an internal heat source. The results give the airflow trajectories with respect to the different conditions. Besides, a method is put forward to process the experimental results, and is used to generate experimental data benchmark for validating and developing CFD models.

Keywords: Experimental measurement, indoor airflow, 3D PTV, trajectories, velocity, temperature, heat source

1. Introduction

The performances of ventilation and air distribution systems have direct influence on the thermal comfort, energy efficiency and sustainability of modern buildings. Developing and evaluating ventilation and air distribution systems is always an important issue for HVAC (Heating, ventilation and Air Conditioning) researchers and engineers. Eight main ventilation systems have been applied in modern buildings, including mixing ventilation (MV), displacement ventilation (DV), personalized ventilation (PV), hybrid air distribution (HAD), stratum ventilation (SV), protected occupied zone ventilation (POV), local exhaust ventilation (LEV), and piston ventilation (PiV). Cao et al. [126] carefully reviewed the performances of these systems. Among these, mixing ventilation and displacement ventilation [15, 16] are the most commonly applied. In contrast to displacement ventilation, mixing ventilation doesn't rely on the presence of internal heat sources to ventilate the space, and therefore can also be used in, but not limited to, isothermal cases. Moreover, mixing ventilation can be characterized by relatively uniform distributions. Therefore, mixing ventilation is continuously being studied and developed [e.g. 127-132].

For evaluating the performance of different ventilation and air distribution systems, many methods have been proposed and used. Chen [11] summarized the general ventilation performance assessment methods, including analytical models, empirical models, reduced-scale experiments, full-scale experiments, multi-zone network models, zonal models and Computational Fluid Dynamics (CFD). Among these methods, CFD is the most applied method, which accounts for about 70% of the available literature, due to its relative low cost and easy access characteristics. However, a reliable CFD simulation usually needs abundant experimental data to be validated, and therefore, reduced-scale and full-scale experiments still play an important role in the indoor airflow study. To conduct these experiments, many modern measurement methods for indoor airflow have been developed and used, Sun and Zhang [13] summarized these methods. Generally, these methods can be divided into point-wise technology, such as Hot wire/film anemometry (HWA/HFA), Laser Doppler anemometry (LDA), and global-wise technology, including Particle Image Velocimetry (PIV), Particle Streak Velocimetry (PSV), and Particle Tracking Velocimetry (PTV). In previous studies, point-wise technology was the most applied measurement method. In recent years, PIV technology has been applied in indoor airflow study, due to its commercial availability. Cao et al. [14] gave a detailed review of PIV technology and applications for indoor airflow field. However, PIV measurement usually needs laser as the illumination device, and therefore the measurement domains are usually two-dimensional or small-scale three-dimensional. More, as a Eulerian measurement method, it cannot provide the particle trajectories to reflect the Lagrangian characteristics of airflow movement. Compared to PIV technology, PTV technology overcomes these drawbacks, and is more suited to conduct large-scale three-dimensional measurements. Hence, it has been more and more applied in indoor airflow study. Fu et al. [104] gave a review concerning PTV technology and applications for indoor airflow field.

In previous studies, the applications of PTV technology for indoor airflow field was more

focused on the verification of PTV measurement algorithms [e.g. 27, 49, 67], and was seldom used to investigate the characteristics of indoor airflow in a systematic way. In this paper, 3D PTV technology is employed as the velocity measurement tool to investigate the characteristics of indoor airflow from the three-dimensional and Lagrangian perspective. Through the application of 3D PTV technology, air (particle) trajectories and three-dimensional velocity information are provided, which can make the indoor airflow better understood. The investigated airflow is generated by the method of mixing ventilation, and the airflow is measured under three conditions: (i) isothermal condition: there is no difference of temperature between the inlet airflow and the outlet airflow; (ii) non-isothermal condition: there is positive difference of temperature between the inlet and outlet airflow; (iii) heat source condition: a heat generator is installed inside the test cavity to generate heat. The details of the experimental facility, boundary conditions and procedure are introduced in section 2; the experimental results are shown and analyzed in section 3; the last section sums up the relevant conclusions.

2. Experimental facility, condition and procedure

2.1 Experimental facility

The experimental facility consists of four parts: the inlet air control system, the test cavity, and the facilities for measuring the air temperature and velocity. The inlet air control system is composed of a fan and a thermal resistance, which power output is controlled by a Selectronic SL-1731SB multi-entry variable voltage (0-30V) and current (0-3A) unit. The controlled inlet air temperature and velocity are measured as described in section 2.2.

The test cavity is of dimension 1013 mm (Length/x-direction) \times 1013 mm (Width/y-direction) \times 730 mm (Height/z-direction), and is made of plexiglass. The air inlet is a round hole of diameter of 73 mm, set in the center of the cavity ceiling, and the air outlet is a rectangular hole of dimension of 56 mm (L/x-direction) \times 40 mm (H/z-direction), set on the lower part of a cavity wall along with x-direction. A heat source is positioned on the lower part of the wall opposite the outlet hole. The heat source is made of a thermal resistance attached to an aluminum plate of dimension 315 mm \times 315 mm. The thermal resistance power is also controlled by the variable voltage and current controller. The schematic of experimental facility is shown in Figure 4-2.

The temperature measuring system consists of 32 Class one T-type thermocouples of precision $\pm 0.5^\circ\text{C}$, which are distributed inside the cavity and the plates of the test cavity, as shown in Figure 4-3. In this study, 3D PTV system is employed as the velocity measuring system. The hardware of this system includes three Dalsa 4M60 cameras set at 2048×2048 pixels as the image recording devices. Each camera is equipped with a 15 mm Canon lens with a 4.8 aperture. Two 1000 W compact fluorescent BalcarQuadlite lamps are used as the illumination system during the measurement process. The particle tracers are Helium-filled soap bubbles (HFSB) [93], and are injected into the test facility from the air inlet pipe along with the injected forced airflow. In order to reduce the airflow turbulence at the inlet, a set of

drinking pipes forms a cylinder, and is inserted in the main ventilation pipe just before the injection of tracers.

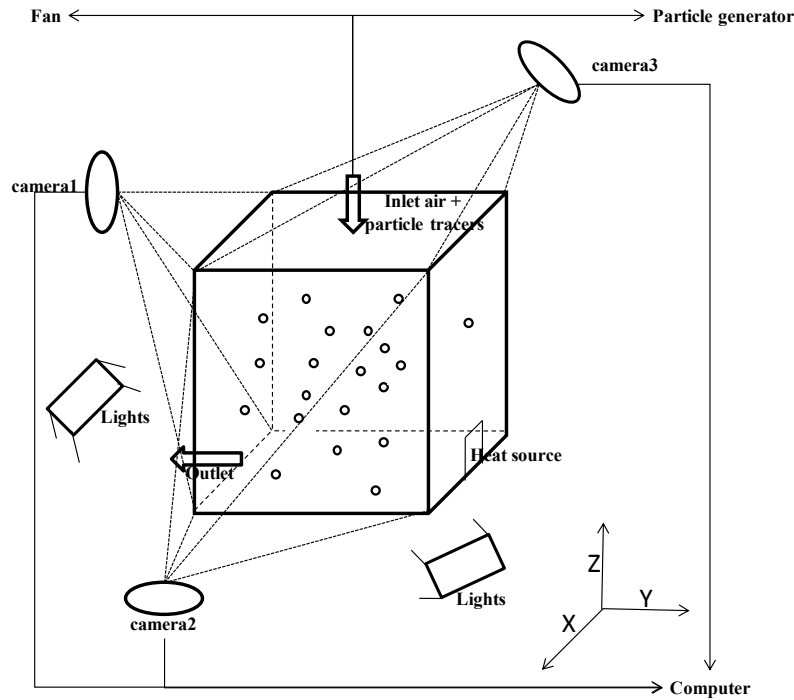


Figure 4-2: The schematic of experimental facility

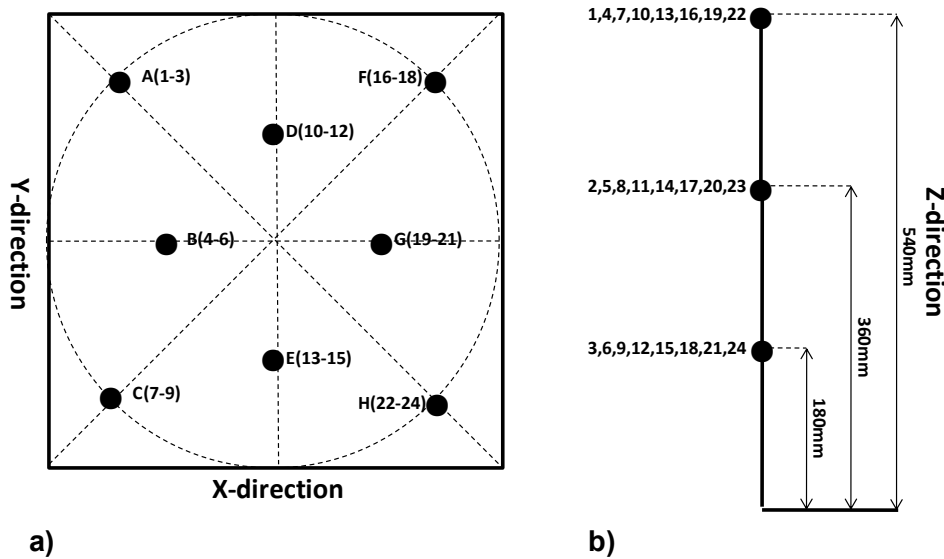


Figure 4-3: The distributions of thermocouples inside test cavity

2.2 Experimental condition

In this study, the characteristics of indoor airflow generated through the mixing ventilation method are investigated. One of the main objectives of this investigation is to provide experimental benchmark data for validating and developing CFD models.

The experimental investigations are conducted under three conditions: isothermal condition,

non-isothermal condition and internal heat source condition.

The isothermal condition means that there is no temperature difference between the inlet air and outlet air. In real measurements, the air temperature difference is controlled to remain less than 1°C. Five cases with different average inlet air velocities as listed in Table 4-1 are measured. The air velocity at the cavity inlet and outlet were measured by the use of a Testo 425 hot wire velocimeter of precision $\pm 0.03 \text{ m/s} + 5\%$ of reading value.

Table 4-1: Inlet air velocity under isothermal condition

Case 1	Case 2	Case 3	Case 4	Case 5
0.52 m/s	0.96 m/s	1.48 m/s	1.89 m/s	2.36 m/s

For non-isothermal condition, heating mode is investigated, which means that the temperature of supply air is higher than that of the cavity. Generally, in heating ventilation, the temperature difference of supply air to room air is typically not higher than 10°C. Here, six cases are measured, and the detailed information on inlet air velocity (V_{in}) and the temperature difference of supply air to cavity air (ΔT) is listed in Table 4-2.

Table 4-2: Inlet air velocity and over-temperature of supply air to cavity air under non-isothermal condition

	Case 1	Case 2	Case 3	Case 4	Case 5	Case 6
ΔT	2.10°C	3.71°C	5.61°C	7.17°C	8.39°C	10.04°C
V_{in}	1.47 m/s	1.47 m/s	1.47 m/s	1.47 m/s	1.46 m/s	1.46 m/s

Besides the isothermal and non-isothermal conditions, the third condition is a heat source condition, where a thermal resistance is installed opposite of the outlet inside the test cavity as the heat source. Here, three cases corresponding to different heat power generation are measured. The information on average inlet airflow velocity (V_{in}) and heat power (P) is listed in Table 4-3.

Table 4-3: Inlet air velocity and heat power under heat source condition

	Case 1	Case 2	Case 3
V_{in}	1.47 m/s	1.46 m/s	1.47 m/s
P	1.490 W	3.984 W	7.216 W

2.3 Experimental procedure

The air velocity inside the cavity is measured through 3D PTV technology, and during the process of flow recording, the air temperature is recorded by the thermocouples described in 2.1. In order to reduce the effect of the velocity due to particle seeding, the recording begins at least 30s after the valve of bubble generation has been closed. For each case as described in section 2.2, two sets of independent measurements are conducted and the final results are the average value from these two sets of measurements. For each independent measurement, the

recording time is 60s. In order to improve the particle image quality, the frame per second (FPS) of the cameras is set based on the inlet air velocity. For the non-thermal condition and internal heat source condition, the cameras are set as 30 fps. For isothermal condition, the cameras are set as 10 fps (case 1), 30 fps (case 2, case 3) and 60 fps (case4, case5) respectively.

The flow chart of our 3D PTV procedure is shown in Figure 4-4. In this study, the cameras were calibrated from a planar calibration target, which is shown in Figure 4-5. The calibration algorithm [66] is used to calculate the focal length, the principle point position, and the distortion coefficients that minimize the reconstruction error in the 3D positions of detected particles.

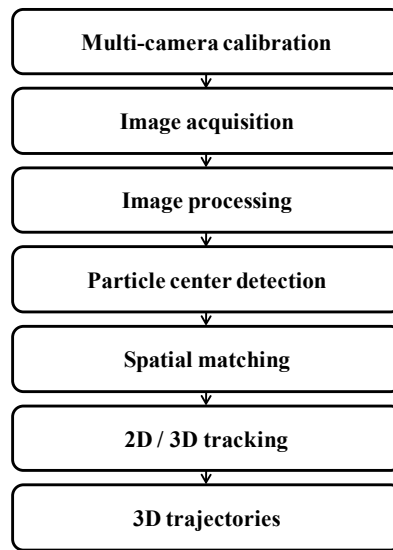


Figure 4-4: Flow chart of 3D PTV measurement



Figure 4-5: Camera calibration target

The method introduced by Biwole [45] is used to do image processing. To minimize the effect of irregular bubble pixel shape in camera images, a weighted-average method based on the light intensity is used to determine the coordinate of bubbles centroid, as Eq.(4-3) shows, where (x_{cam}, y_{cam}) are the pixel coordinates of each pixel belonging to the particle and $I(x_{cam}, y_{cam})$ is the pixel luminance. This method has the characteristics of easy implementation, rapid and effective computation [27].

$$x_c = \frac{\sum x_{cam} I(x_{cam}, y_{cam})}{\sum I(x_{cam}, y_{cam})}; \quad y_c = \frac{\sum y_{cam} I(x_{cam}, y_{cam})}{\sum I(x_{cam}, y_{cam})} \quad (4-3)$$

Two different temporal tracking strategies are used jointly in this study based on their performances [123]. When the number of detected particles is relatively high, the polynomial temporal tracking algorithm proposed by Li et al. [81] is employed (referred to as algorithm A in the following). As the number of detected particles decreases to less than 175 for three views, the modified cross-correlation temporal tracking algorithm (referred to as algorithm B in the following) proposed by Biwole [45], is used.

The main expression for the polynomial temporal tracking algorithm A is given in Eq.(4-4), where x_{pre} is the pixel coordinates vector at the instant time (frame) t , and 2×1 constant vectors a , b and c are acquired by least-squares fitting.

$$x_{pre} = at^2 + bt + c \quad (4-4)$$

Eq.(4-5) is the main expression for the modified cross-correlation temporal tracking algorithm B, where f is the research window, \bar{t} is the mean of the template (interrogation window) and $\bar{f}_{u,v}$ is the mean of $f(x, y)$ in the template region. Here, the searching pattern consists of each single particle instead of a group of particles as in traditional PIV.

$$\gamma(u, v) = \frac{\sum_{x,y} [f(x, y) - \bar{f}_{u,v}] [t(x-u, y-v) - \bar{t}]}{\sqrt{\sum_{x,y} [f(x, y) - \bar{f}_{u,v}]^2 \sum_{x,y} [t(x-u, y-v) - \bar{t}]^2}} \quad (4-5)$$

More details about these temporal tracking algorithms can be found in previous literature [45, 81, 123].

The method using the epipolar constraint is used for spatial matching, as expressed in Eq. (4-6). Let (x_i, y_i) and (x_j, y_j) be the normalized pixel coordinates from each camera, t an instant time, and s a threshold value which is given the value 2 in this study. If (x_i, y_i) and (x_j, y_j) satisfy Eq. (4-6), it means that the particle is matched at that instant time. The least squares method as described in the literature [27] is employed to achieve the 3D reconstruction. More details about spatial matching and 3D reconstruction can be found in previous literature [e.g. 27].

$$\begin{bmatrix} x_i^t & y_i^t & 1 \end{bmatrix} F_{ij} \begin{bmatrix} x_j^t \\ y_j^t \\ 1 \end{bmatrix} < s \quad (4-6)$$

Because the performance of 3D PTV measurement decreases as the tracked frame increases [123], in this study, the tracked frame number is set at 10. In order to get long trajectories when necessary, a strategy is put forward to link the trajectories in every tracked set. This strategy uses the last frame in previous tracked set as the starting frame in next tracked set. Therefore, the particle trajectories can be linked easily, by comparing the particle coordinates in last frame and starting frame in two consecutive tracked set.

3. Experimental results

In this section, the experimental results are shown, including the particle trajectories, measured air velocity and air temperature. In most existing papers, the results are processed by interpolation to get uniform experimental data [e.g. 44, 133]. In this study, a different method is put forward to process the experimental results. This method is based on the number of velocity information in particle trajectories crossing the different areas inside the cavity. First, the whole volume is divided into uniformly sized cell, then, the number of velocity information in particle trajectories per cell is calculated. Based on the calculated number of velocity information, the cell size is modified. If the number of velocity information in one cell is less than a constant value, this cell will be combined with adjacent cell. Oppositely, the cell will be divided into smaller size cells as long as the velocity information exceeds a certain constant value. Therefore, non-uniform size cells are generated. Finally, the average properties value are calculated in each cell, an example is as Eq. (4-7), where \bar{u} is the calculated average value, u_i is the value in this cell, N is the number of values.

$$\bar{u} = \frac{\sum_{i=1}^N u_i}{N} \quad (4-7)$$

In this study, the minimum number of velocity information per cell is set as 20, and the theoretical number of velocity information is set as 50. The flow chart of the method is illustrated in Figure 4-6.

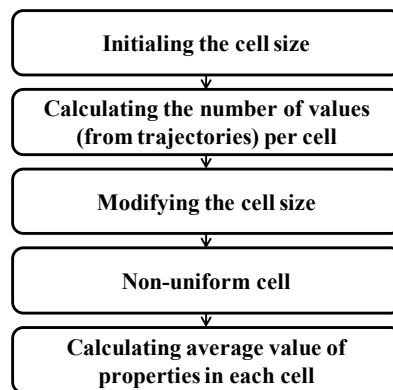


Figure 4-6: Flow chart of processing the results

3.1 Isothermal condition

3.1.1 Trajectories

In order to make the airflow trajectories be as clear as possible in the figures, about only 5%-10% of the detected trajectories are shown (it also applies in sections 3.2 and 3.3). The trajectories measured with respect to case 1 to case 5 are shown from Figure 4-7(a) to Figure

4-7(e). These trajectories reflect the airflow structure. The trajectories measured for all cases are generally similar. A circle structure can be detected in the bottom right part of the cavity, along with X-direction. For case 1, because the average inlet velocity is only 0.52 m/s, the airflow is diffused weakly, with the incoming air staying in the lower part of the cavity. Therefore, trajectories are mainly detected in that part of the cavity. The figures also indicate that the disorder of the airflow structure will increase as the inlet velocity increases.

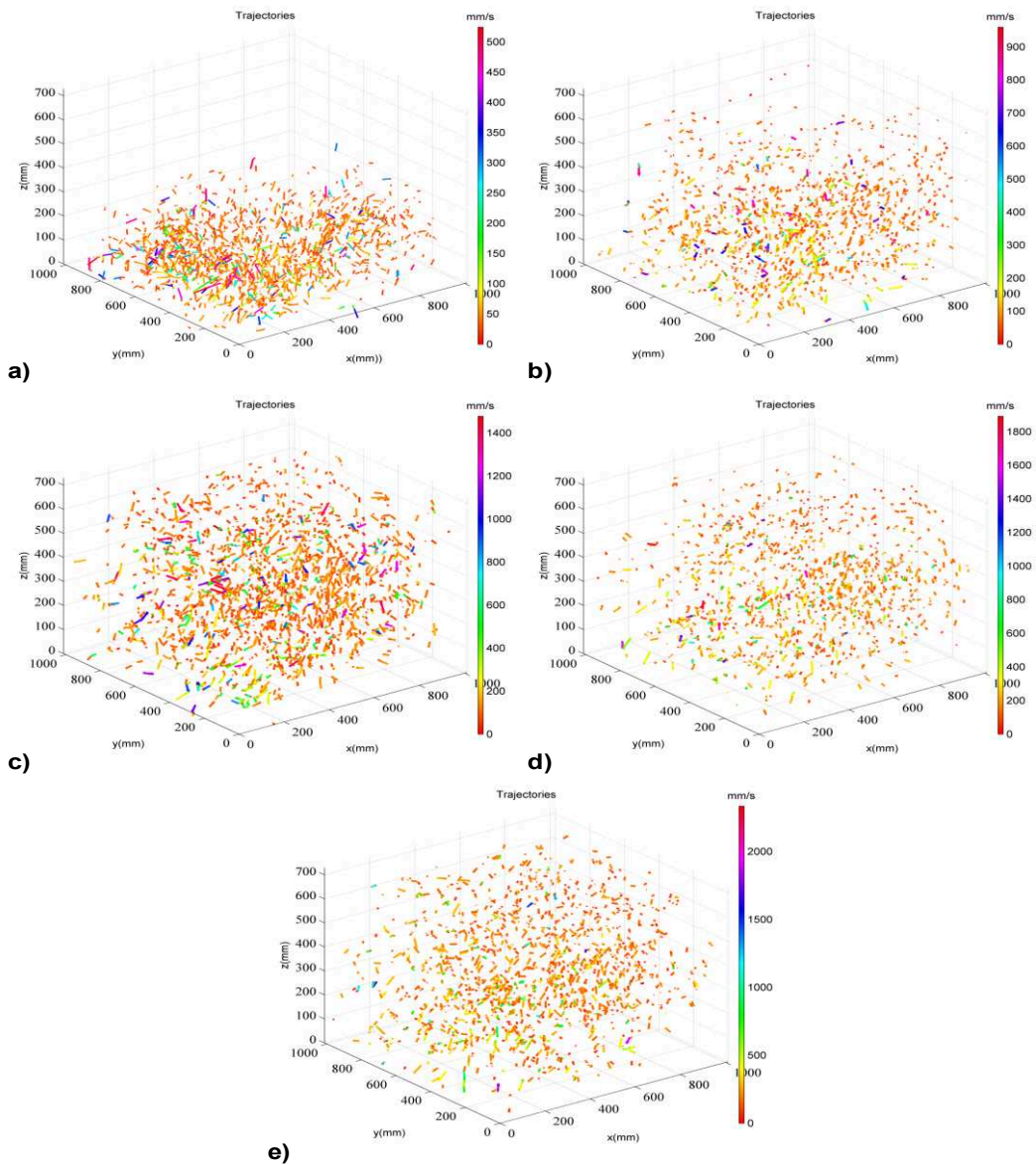


Figure 4-7: The trajectories with respect to all cases under isothermal condition

3.1.2 Velocity information

The calculated velocity magnitude contours with respect to case 1 to case 5 are shown from Figure 4-8(a) to Figure 4-8(e). For each figure, the velocity magnitude at five planes ($X=506.5$ mm, $Y=506.5$ mm, $Z=180$ mm, $Z=360$ mm, $Z=540$ mm) are shown. It should be noted that the velocity magnitude at these planes actually reflects the values which are in the nearest calculated cell, the same as in the conditions of non-isothermal and heat source. The

figure shows that the airflow velocity is relative high around the region of outlet for all cases. The probability density functions (PDF) of velocity at the X-direction, Y-direction and W-direction (u , v , w) with respect to case 1 to case 5 are shown from Figure 4-9(a) to Figure 4-9(e). The figure indicates that the velocity in Z-direction accounts for most part in the total velocity magnitude for all cases.

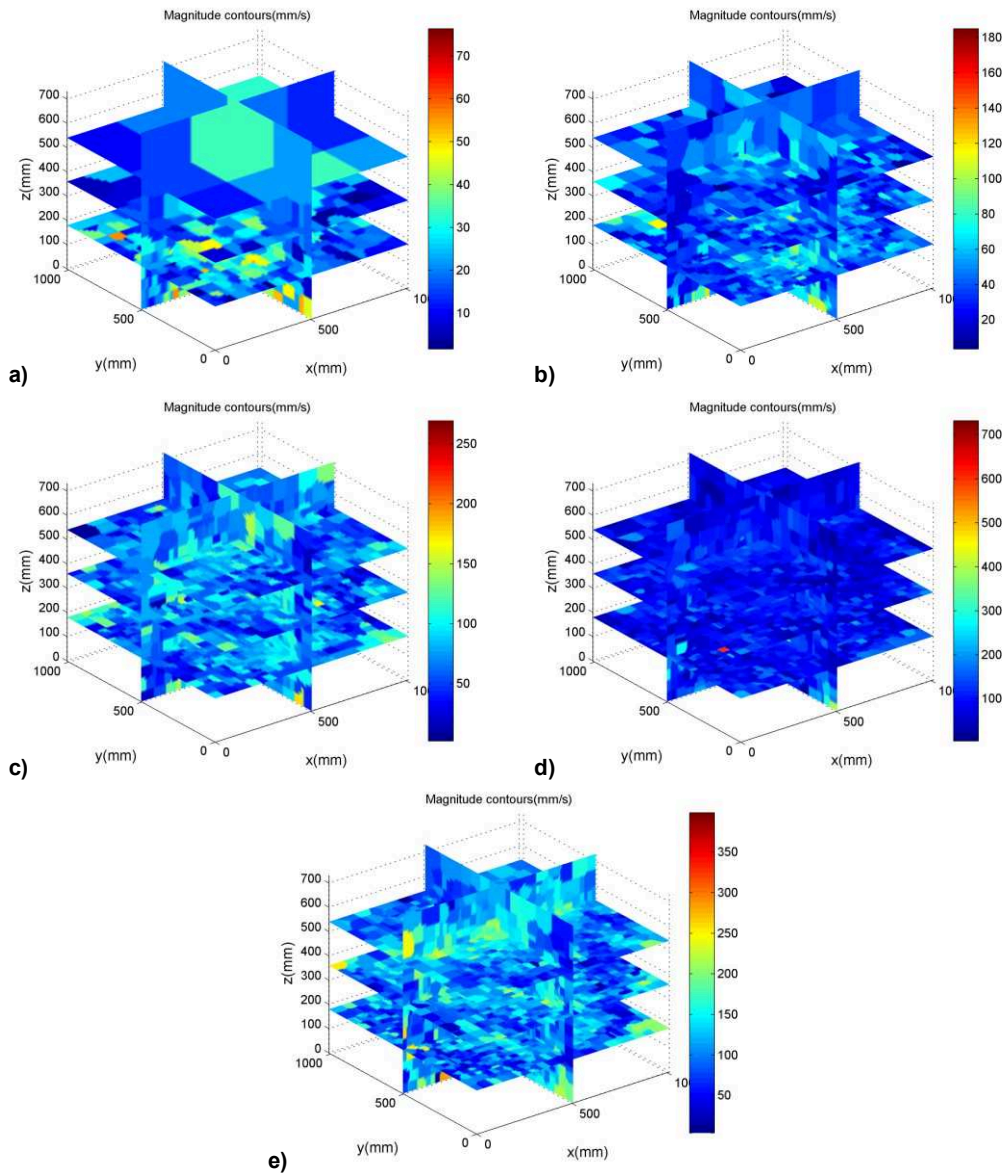


Figure 4-8: Velocity magnitude contours with respect to all cases under isothermal condition

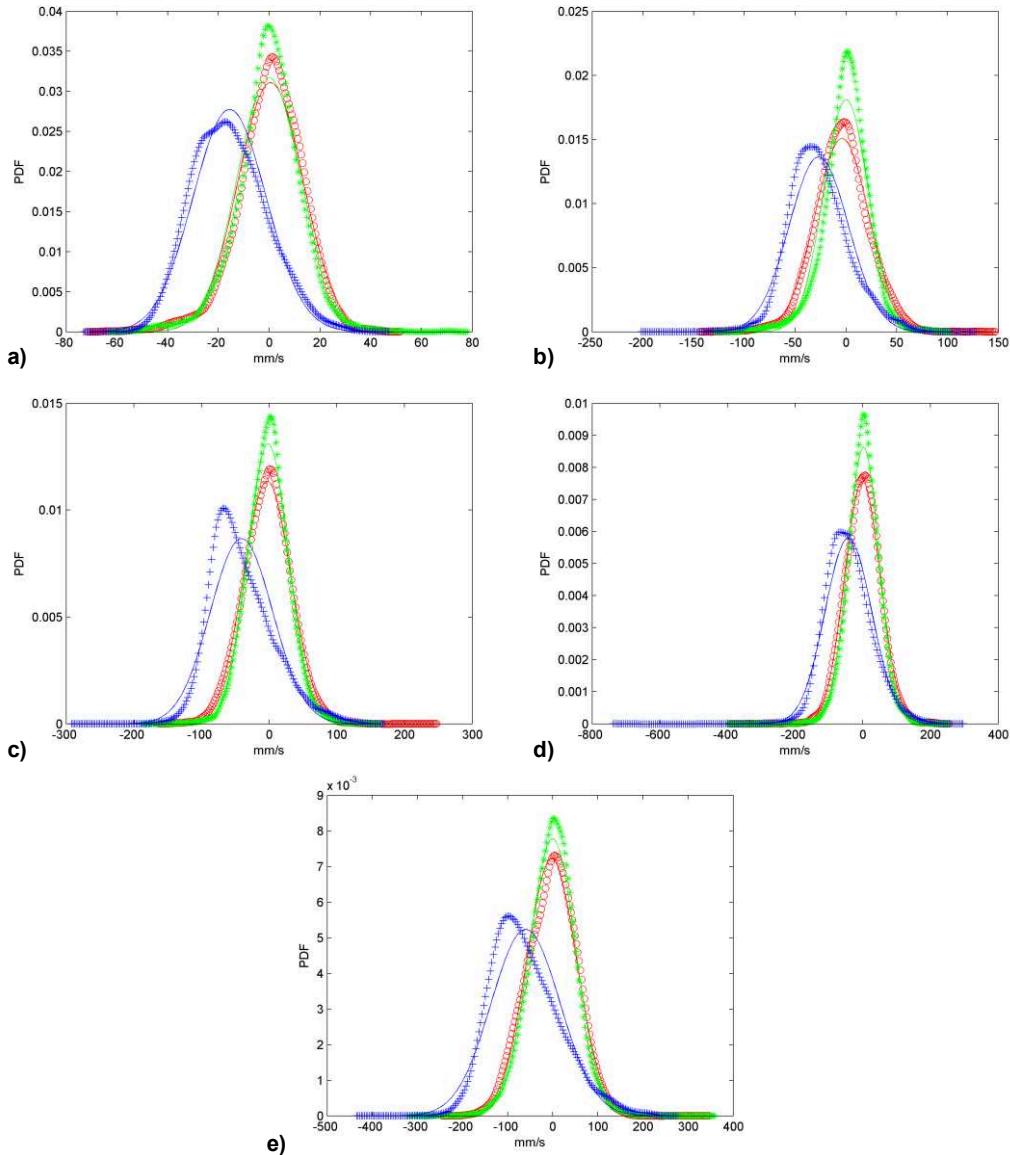


Figure 4-9: PDF of u , v , w with respect to all cases under isothermal condition (u : red, v : green, w : blue, the solid line is the Gaussian fit)

3.2 Non-isothermal condition

3.2.1 Trajectories

In order to make the trajectories be shown with respect to the planes on which are mounted the thermocouples that measure the airflow temperature, the trajectories are shown in three sets. The trajectories measured in the volume $0\text{mm} < Z \leq 270\text{mm}$ with respect to cases 1 to case 6 are shown from Figure 4-10(a) to Figure 4-10(f) respectively. Similar to the isothermal condition, a circle structure can be detected in the bottom right part of the cavity, along with X-direction, which is more visible in case 6. The trajectories measured in the volume $270\text{mm} < Z \leq 540\text{mm}$ with respect to cases 1 to case 6 are shown from Figure 4-11(a) to Figure 4-11(f). In this region, the airflow mainly shows a straight structure. The trajectories

measured in the volume $540\text{mm} < Z < 730\text{mm}$ with respect to cases 1 to case 6 are shown from Figure 4-12(a) to Figure 4-12(f). In this region, a circle structure directing to the inlet can be detected in the right part of the cavity, along the X-direction.

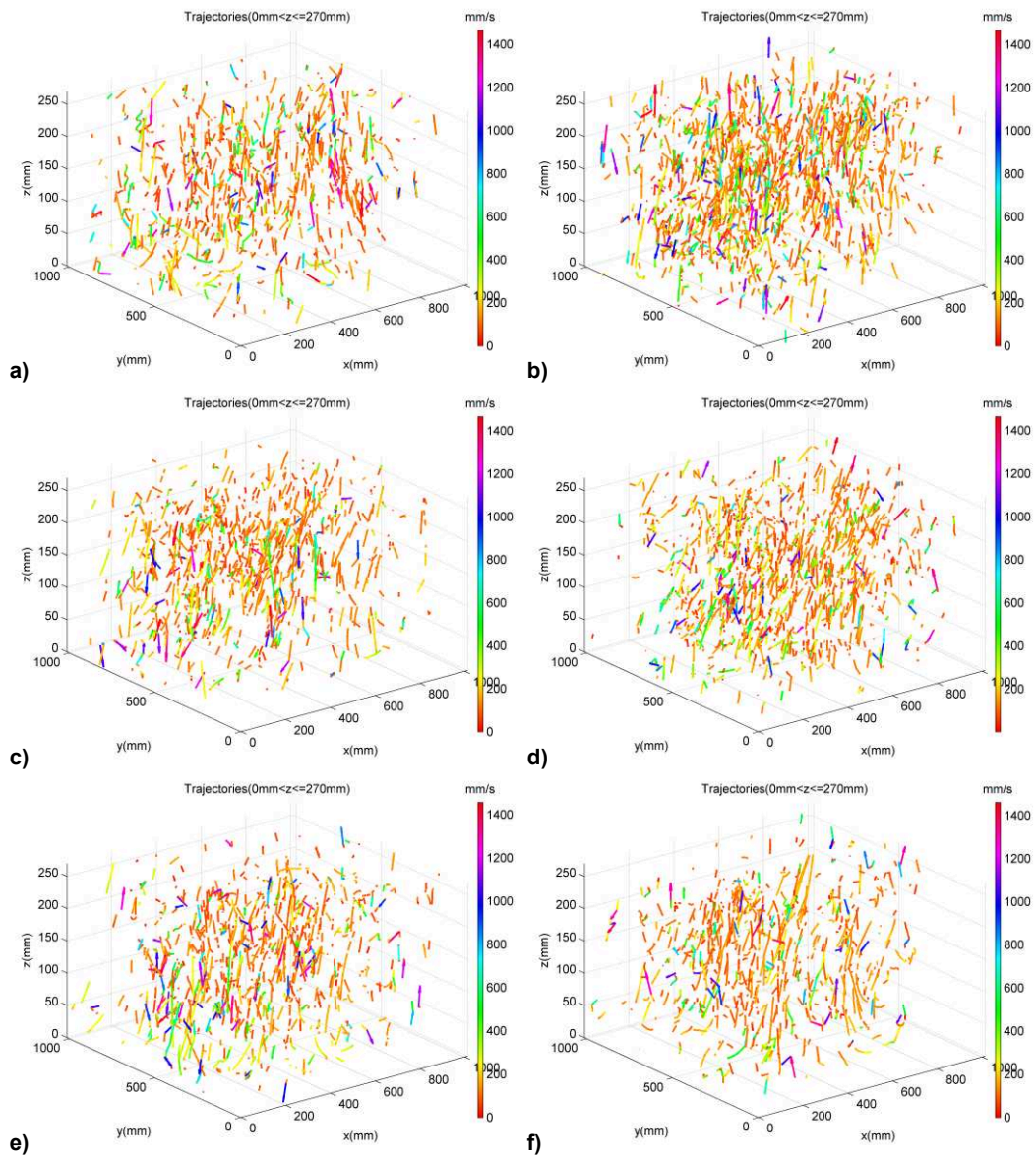


Figure 4-10: The trajectories with respect to all cases under non-isothermal condition. Volume $0\text{mm} < Z <= 270\text{mm}$.

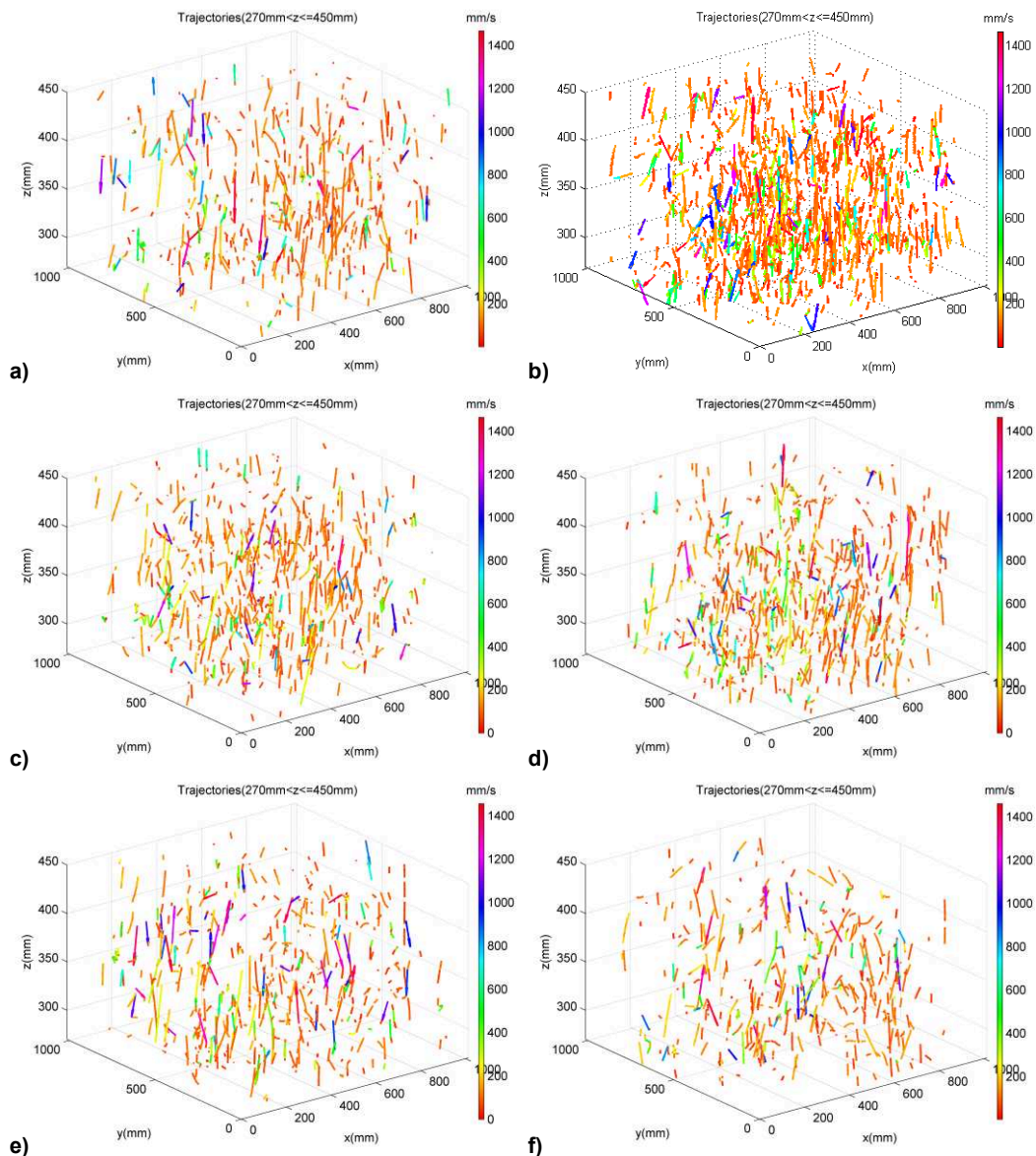


Figure 4-11: The trajectories with respect to all cases under non-isothermal condition. Volume $270\text{mm} < Z \leq 540\text{mm}$.

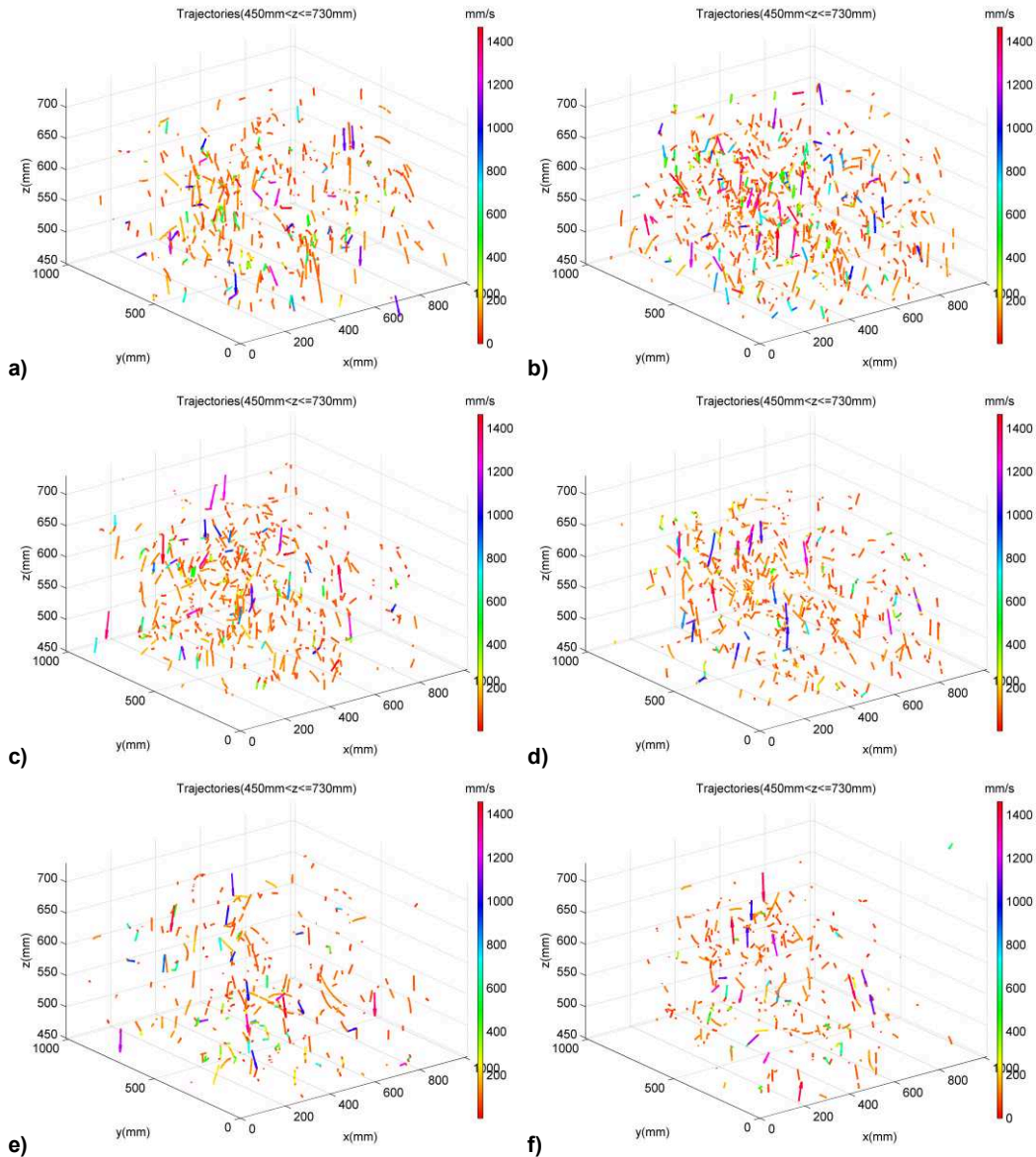


Figure 4-12: The trajectories with respect to all cases under non-isothermal condition. Volume $540\text{mm} < Z < 730\text{mm}$.

3.2.2 Velocity and temperature information

The calculated velocity magnitude contours with respect to case 1 to case 6 are shown from Figure 4-13(a) to Figure 4-13(f). For each figure, the velocity magnitude at five planes ($X=506.5\text{ mm}$, $Y=506.5\text{ mm}$, $Z=180\text{ mm}$, $Z=360\text{ mm}$, $Z=540\text{ mm}$) are shown. Despite the temperature difference varies, the velocity magnitude around the outlet is relative high than near regions. The PDF of velocity at the X-direction, Y-direction and W-direction (u , v , w) with respect to case 1 to case 6 are shown from Figure 4-14(a) to Figure 4-14(f). The figure indicates that the accounting part of the velocity in Z-direction for the total velocity magnitude will decrease as the air temperature difference between the inlet and the cavity increases. Figure 4-15 shows the average temperature difference between the air inlet and measured points for all cases under the non-isothermal condition. The figure shows that the

heat from the inlet airflow is homogeneously transferred to every area of the cavity, but the temperature difference fluctuations will increase as the air temperature difference between the inlet and the cavity increases.

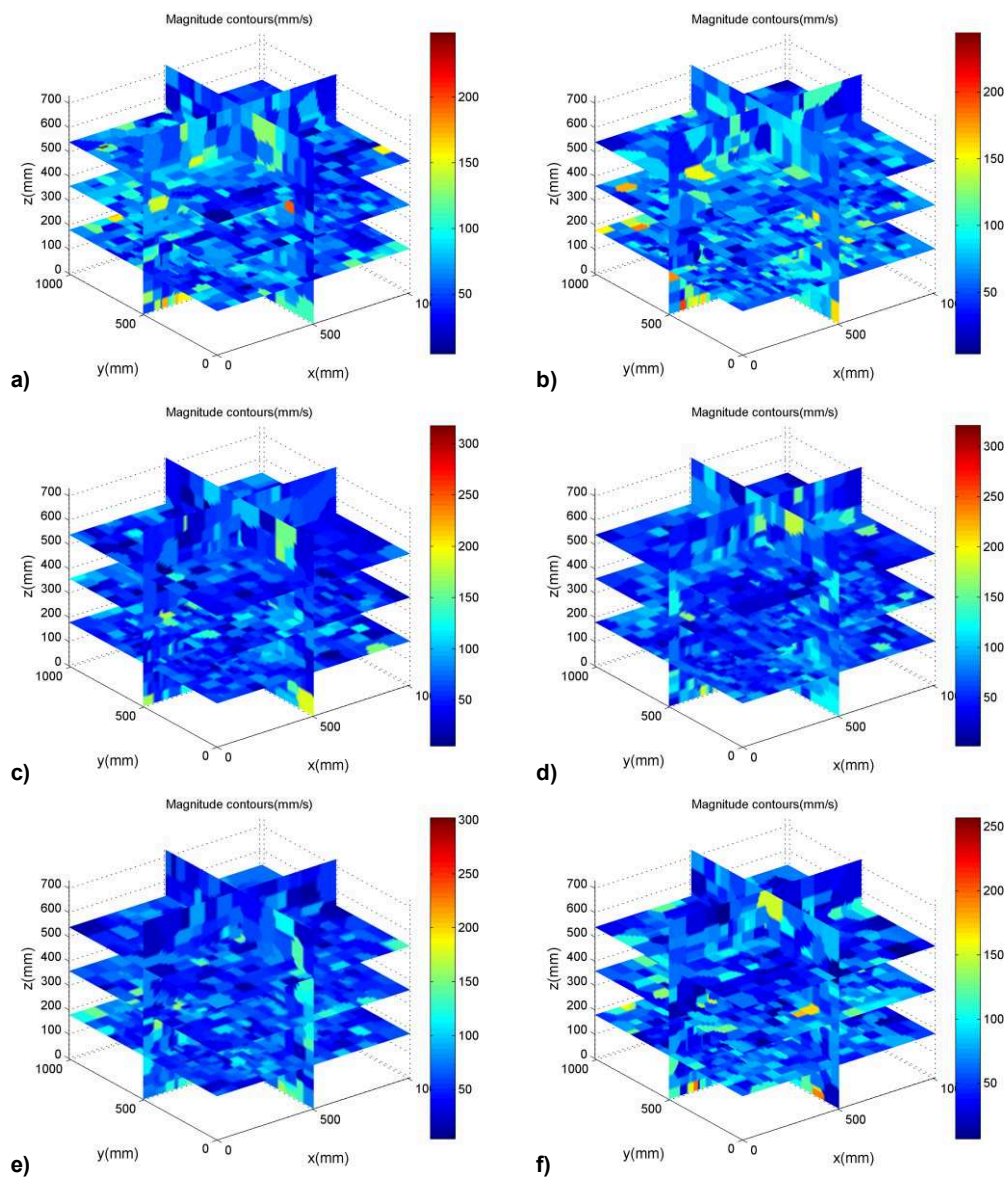


Figure 4-13: Velocity magnitude contours with respect to all cases under non-isothermal condition

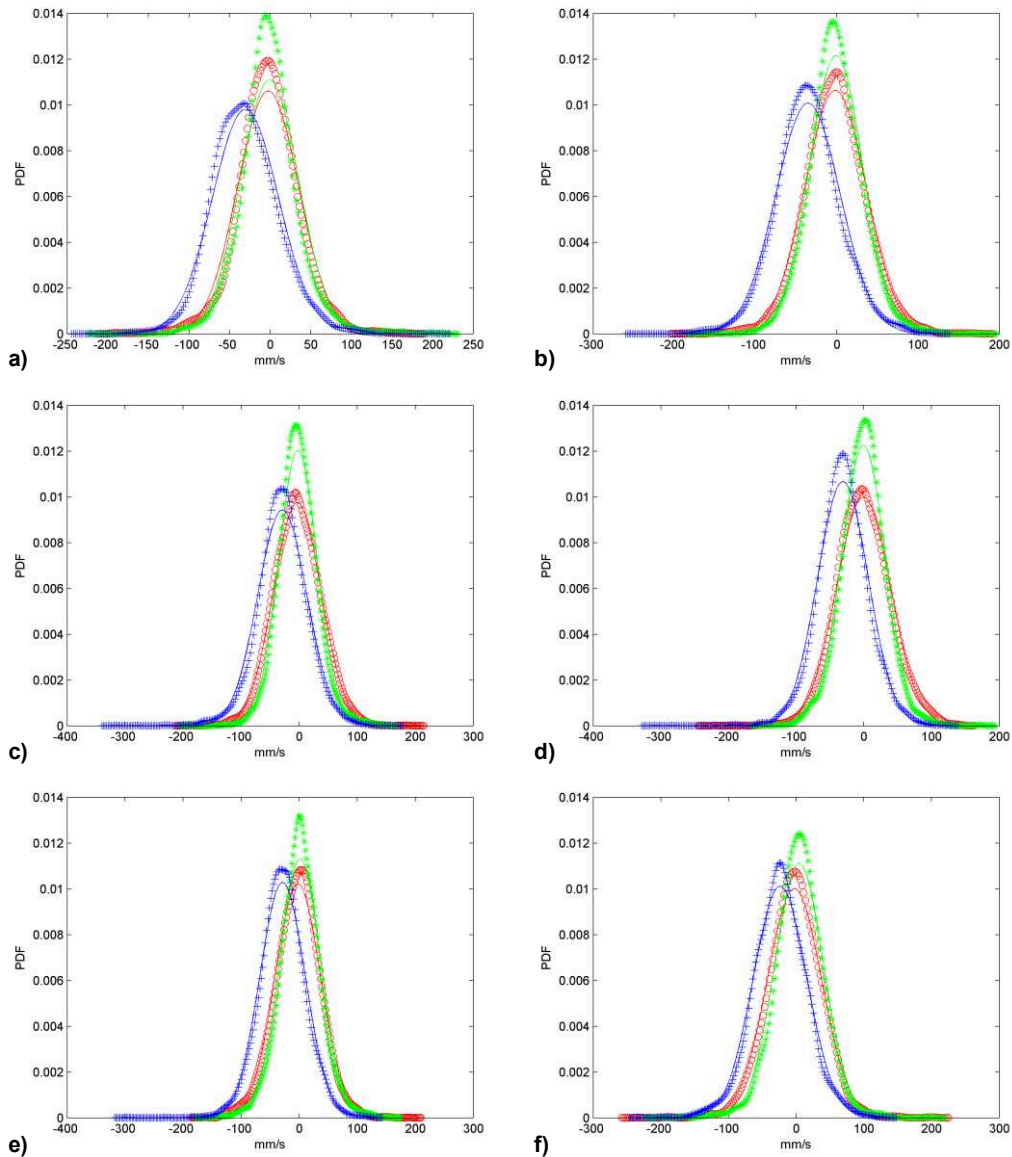


Figure 4-14: PDF of u , v , w with respect to all cases under non-isothermal condition (u : red, v : green, w : blue, the solid line is the Gaussian fit)

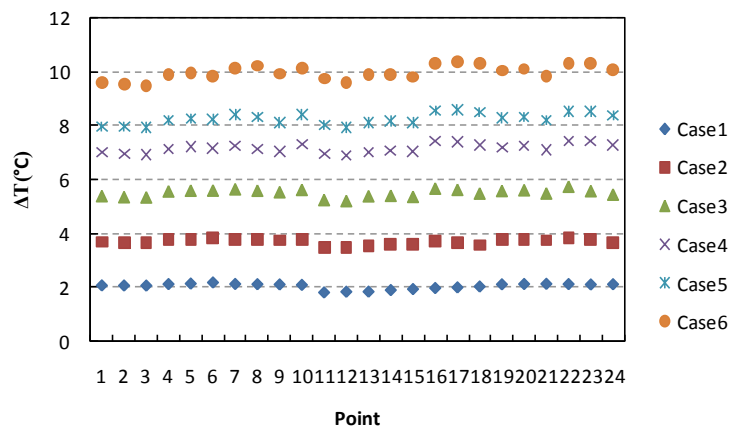


Figure 4-15: The average temperature difference between the air inlet and measured points, with respect to all cases under the non-isothermal condition

3.3 Heat source condition

3.3.1 Trajectories

The trajectories measured with respect to cases 1 to case 3 are shown from Figure 4-16(a) to Figure 4-16(c) respectively. Only the trajectories at the region $Y > 506.5$ mm are shown on the figures, in order to reflect the airflow structure as clearly as possible near the heat source. A circle structure can be detected in the bottom left part of the cavity along with Y-direction.

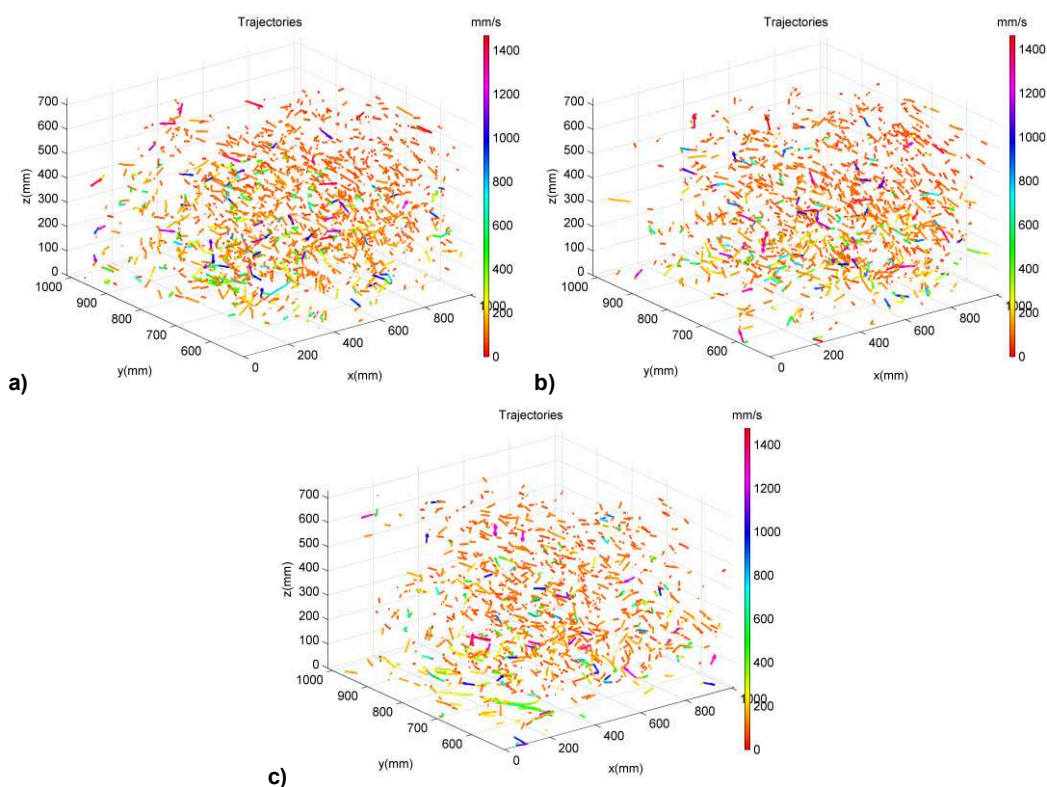


Figure 4-16: The trajectories with respect to all cases under heat source condition. Volume $Y > 506.5$ mm.

3.3.2 Velocity and temperature information

The calculated velocity magnitude contours with respect to case 1 to case 6 are shown from Figure 4-17(a) to Figure 4-17(c) respectively. For each figure, the velocity magnitude at five planes ($X=506.5$ mm, $Y=506.5$ mm, $Z=180$ mm, $Z=360$ mm, $Z=540$ mm) is shown. Despite the variations of the heat source power, the velocity magnitude around the outlet is relative higher than nearby areas. The PDFs of velocity at the X-direction, Y-direction and W-direction (u , v , w) with respect to case 1 to case 3 are shown from Figure 4-18(a) to Figure 4-18(c). The figure indicates that the PDF distribution of velocity in Z-direction is more

similar as the PDF distributions of velocity in X and Y directions as the power of heat source increases. Simultaneously, the large velocity is detected. Figure 4-19 shows the average temperature difference between the air inlet and measured points for all cases under the heat source condition. As the power of heat source increases, the temperature difference between the air inlet and measured points will decrease. The figure also indicates that the heat source has more influence on the airflow above it, because the temperature difference between the air inlet and these measured points (10-12 and 13-15) is relatively small.

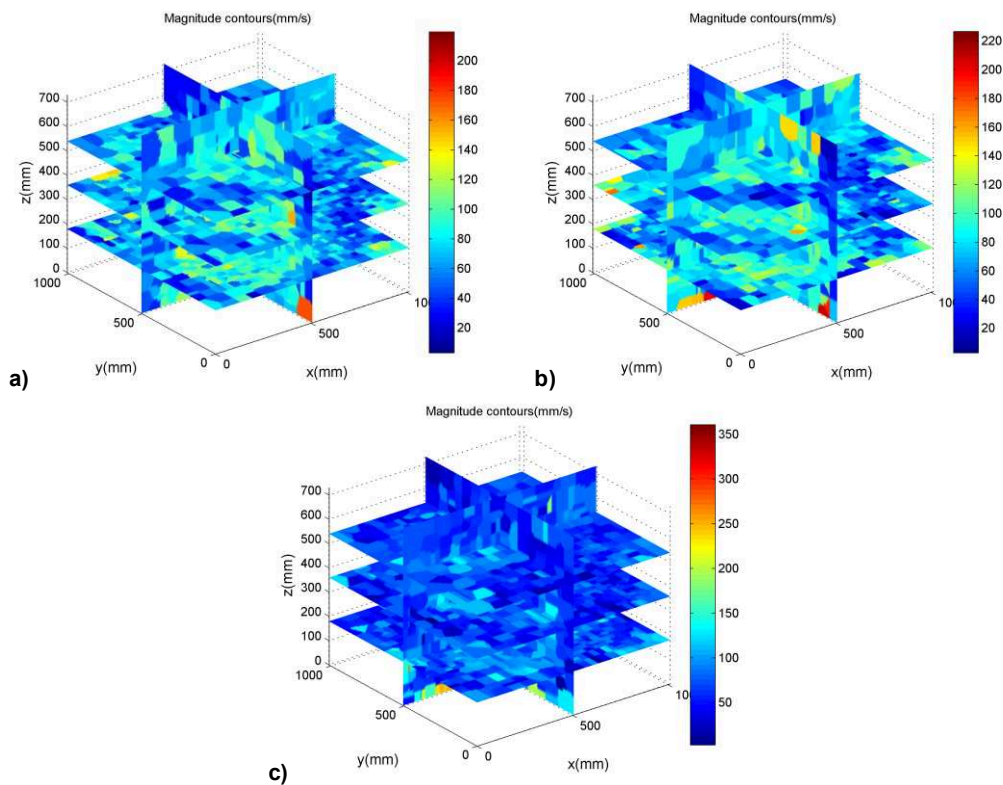


Figure 4-17: Velocity magnitude contours with respect to all cases under heat source condition

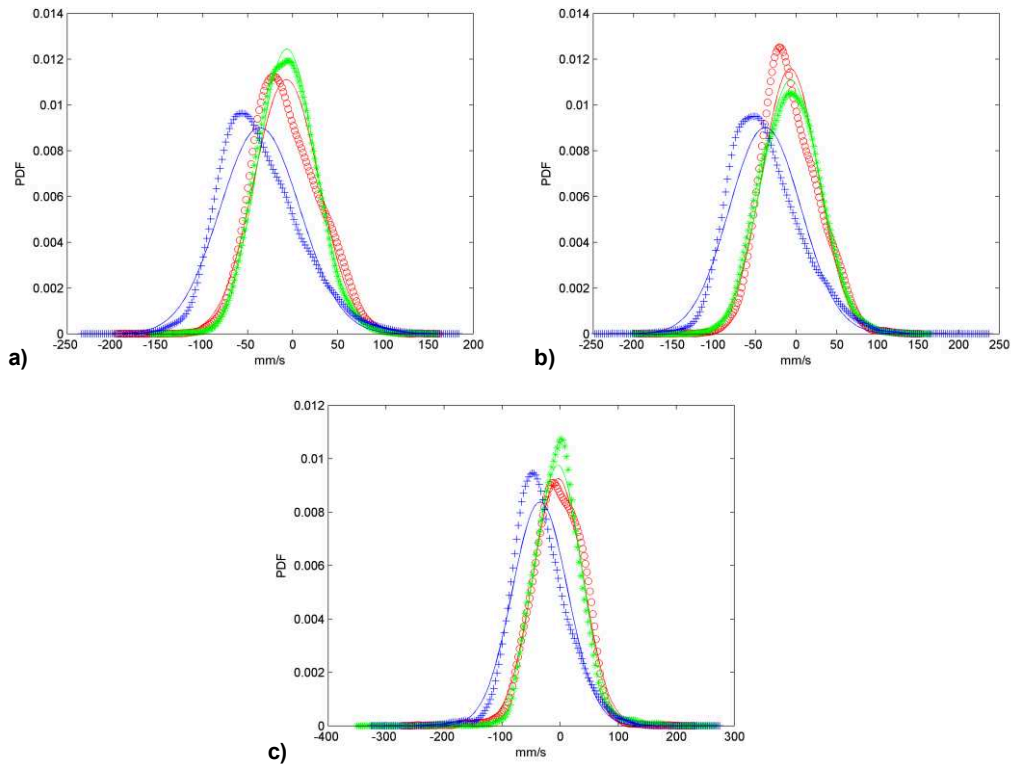


Figure 4-18: PDF of u , v , w with respect to all cases under heat source condition (u : red, v : green, w : blue, the solid line is the Gaussian fit)

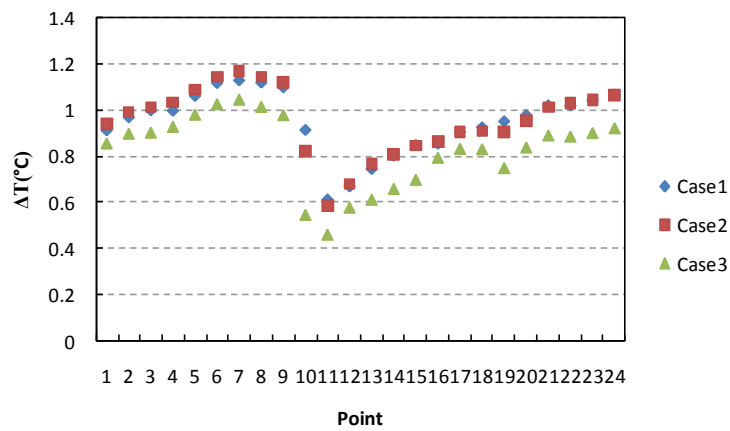


Figure 4-19: The average temperature difference between the air inlet and measured points with respect to all cases under heat source condition

3.4 Supplement

The detailed calculated average velocity information for areas close to the selected Z planes (180mm/360mm/540mm) with respect to case 3 under isothermal condition, case 3 and case 4 under non-isothermal condition and case 2 under heat source condition are listed in Appendix.

4. Conclusions

This article presents an investigation of indoor airflow distribution generated by mixing ventilation method. 3D PTV technology is employed as the velocity measurement tools to obtain the airflow trajectories and relevant velocity information. Simultaneously, thermocouples are used to measure the airflow temperature. The investigation is conducted with respect to three conditions: isothermal-condition, non-isothermal condition and heat source condition. The three-dimensional airflow structure is shown through the airflow trajectories measured. Furthermore, the airflow velocity information is calculated based on the new proposed method, instead of the interpolation. The obtained and processed experimental data is given to serve as benchmark for validating and developing CFD models for indoor airflow study.

Acknowledgment

This work was supported by a grant from the French Region Provence Alpes Côte d'Azur and by a funding from the French National Research Agency (ANR) through the FLUBAT project.

Appendix

Table 4-4: Average velocity information for areas close to the selected Z planes with respect to case 3 under isothermal condition

x (mm)	y (mm)	z (mm)	u (mm/s)	v (mm/s)	w (mm/s)	Magnitude(mm/s)
395.703	205.766	536.094	-7.527	26.683	-74.795	79.768
490.672	174.109	536.094	3.981	-33.050	-38.946	51.234
546.070	174.109	536.094	8.850	24.418	-90.753	94.396
553.984	142.453	536.094	12.318	-1.312	-106.237	106.956
561.898	174.109	536.094	-0.881	5.275	-60.118	60.355
585.641	205.766	536.094	32.407	18.767	-113.615	119.628
300.734	395.703	353.594	7.700	47.521	-112.803	122.646
332.391	269.078	353.594	17.720	19.230	-0.993	26.168
332.391	300.734	353.594	-38.296	13.201	-71.907	82.532
364.047	364.047	353.594	14.431	6.094	-54.593	56.795
364.047	395.703	353.594	15.313	-4.090	-55.994	58.194
395.703	300.734	353.594	55.895	-13.964	-44.772	72.964
395.703	332.391	353.594	-12.221	-11.355	-84.456	86.088
395.703	364.047	353.594	29.148	-14.279	-62.353	70.295
395.703	395.703	353.594	39.496	-2.670	-68.194	78.851
427.359	364.047	353.594	-1.091	-13.012	-73.213	74.368
427.359	427.359	353.594	18.134	-0.368	-93.885	95.621
459.016	237.422	353.594	19.280	0.351	-93.598	95.564
459.016	300.734	353.594	3.862	-14.938	-85.968	87.342
459.016	395.703	353.594	15.064	8.213	-77.290	79.171
522.328	332.391	353.594	24.182	37.479	-94.472	104.472
546.070	205.766	353.594	4.161	7.539	-87.864	88.285
553.984	300.734	353.594	22.247	19.296	-83.601	88.636
553.984	332.391	353.594	0.964	25.842	-91.647	95.225
553.984	364.047	353.594	-20.296	1.018	-86.978	89.321
561.898	205.766	353.594	11.276	8.851	-95.575	96.644
585.641	174.109	353.594	-4.284	9.708	-125.834	126.281
585.641	237.422	353.594	61.775	30.639	-78.284	104.324
585.641	300.734	353.594	5.312	-9.081	-92.076	92.675
585.641	364.047	353.594	-12.641	10.895	-78.108	79.871
585.641	427.359	353.594	-16.448	26.109	-96.816	101.614
617.297	205.766	353.594	4.970	-20.516	-89.722	92.172
617.297	237.422	353.594	-14.760	-15.770	-106.000	108.178
617.297	269.078	353.594	9.172	10.892	-104.195	105.164
617.297	300.734	353.594	-6.956	29.895	-98.072	102.763
617.297	332.391	353.594	21.295	23.666	-83.521	89.382

617.297	364.047	353.594	31.737	6.393	-104.161	109.076
617.297	427.359	353.594	9.434	9.354	-92.046	93.000
648.953	142.453	353.594	52.303	-20.928	-151.846	161.960
648.953	174.109	353.594	22.138	3.546	-119.008	121.102
648.953	205.766	353.594	-1.386	0.613	-81.332	81.346
648.953	237.422	353.594	8.535	2.551	-90.372	90.810
648.953	332.391	353.594	5.686	-10.355	-58.785	59.961
648.953	427.359	353.594	25.407	15.970	-74.119	79.964
648.953	459.016	353.594	-37.441	23.333	-87.047	97.589
648.953	490.672	353.594	-40.455	-7.637	-39.351	56.951
680.609	174.109	353.594	43.473	-40.086	-63.645	86.876
680.609	237.422	353.594	9.020	-7.745	-55.492	56.751
680.609	490.672	353.594	-16.789	1.280	-81.494	83.216
712.266	205.766	353.594	-72.310	-30.649	-71.110	105.947
712.266	269.078	353.594	-12.815	-12.718	-36.601	40.812
743.922	269.078	353.594	-24.665	-3.628	-35.132	43.079
743.922	300.734	353.594	-37.606	37.147	-60.857	80.608
743.922	332.391	353.594	-61.760	12.530	-64.539	90.203
743.922	364.047	353.594	2.763	4.006	-78.206	78.357
743.922	395.703	353.594	-46.010	5.524	-86.079	97.760
775.578	205.766	353.594	-15.230	-19.910	-32.235	40.834
775.578	237.422	353.594	-8.756	0.913	3.988	9.665
807.234	269.078	353.594	-15.456	4.374	-48.150	50.759
838.891	332.391	353.594	-0.256	26.125	-59.460	64.947
269.078	459.016	171.094	-38.126	8.740	-109.578	116.350
269.078	712.266	171.094	-50.193	-15.581	-116.963	128.228
300.734	237.422	171.094	-23.994	-47.202	-66.364	84.899
300.734	269.078	171.094	-12.916	3.203	-89.591	90.574
300.734	300.734	171.094	-18.609	3.822	-79.563	81.799
332.391	142.453	171.094	-26.151	-31.482	-67.805	79.199
332.391	174.109	171.094	-28.189	-31.051	-50.556	65.686
332.391	205.766	171.094	-22.281	-47.078	-65.532	83.709
332.391	237.422	171.094	-10.606	-26.338	-57.336	63.981
364.047	205.766	171.094	-16.219	-15.386	-71.890	75.286
395.703	142.453	171.094	-28.197	-46.320	-85.032	100.852
395.703	205.766	171.094	-20.804	-34.423	-60.768	72.873
395.703	269.078	171.094	-27.568	-12.556	-73.539	79.534
395.703	617.297	171.094	-15.719	5.856	-46.362	49.303
459.016	205.766	171.094	-34.521	11.883	-81.925	89.692
459.016	269.078	171.094	-8.737	-2.884	-83.169	83.676
459.016	300.734	171.094	-45.406	-20.444	-72.392	87.865

490.672	142.453	171.094	-7.091	-32.959	-98.400	104.015
522.328	174.109	171.094	9.541	-14.629	-95.204	96.792
522.328	269.078	171.094	-13.727	-31.056	-53.977	63.769
522.328	617.297	171.094	7.424	-4.647	-81.551	82.020
553.984	205.766	171.094	-0.074	15.435	-111.368	112.432
585.641	205.766	171.094	-1.110	-6.019	-66.083	66.366
585.641	237.422	171.094	5.964	39.997	-81.349	90.846
585.641	617.297	171.094	-26.958	18.178	-75.350	82.066
617.297	617.297	171.094	-23.254	-21.241	-62.394	69.893
617.297	775.578	171.094	-23.026	78.290	-6.628	81.875
648.953	142.453	171.094	-0.262	-16.642	-93.390	94.861
648.953	174.109	171.094	27.700	12.333	-120.936	124.680
648.953	237.422	171.094	15.728	-10.527	-71.339	73.807
680.609	174.109	171.094	30.709	5.560	-100.584	105.314
680.609	205.766	171.094	25.980	5.566	-77.175	81.620
680.609	395.703	171.094	-31.635	-41.232	-67.344	85.065
680.609	617.297	171.094	-12.070	37.517	-108.325	115.272
680.609	807.234	171.094	11.359	25.330	4.677	28.151
704.352	205.766	171.094	35.387	19.016	-86.457	95.335
712.266	585.641	171.094	0.753	45.053	-87.681	98.582
720.180	205.766	171.094	37.770	-9.261	-47.919	61.713
743.922	205.766	171.094	52.644	7.930	-79.371	95.572
775.578	205.766	171.094	35.720	2.911	-70.626	79.199
775.578	585.641	171.094	-8.640	24.738	-45.464	52.475
838.891	395.703	171.094	-68.563	-1.323	-30.605	75.096

Table 4-5: Average velocity information for areas close to the selected Z planes with respect to case 3 under non-isothermal condition

x (mm)	y (mm)	z (mm)	u (mm/s)	v (mm/s)	w (mm/s)	Magnitude(mm/s)
142.453	221.594	524.688	50.369	-12.403	-18.694	55.139
158.281	158.281	524.688	16.604	0.100	43.356	46.426
158.281	728.094	524.688	35.884	-32.752	-32.891	58.670
158.281	791.406	524.688	6.868	1.339	-7.307	10.117
158.281	664.781	524.688	45.994	-50.758	24.915	72.887
174.109	221.594	524.688	-16.019	40.555	5.776	43.985
205.766	585.641	524.688	-16.519	44.916	-73.459	87.673
205.766	617.297	524.688	64.081	-35.921	-11.025	74.285
205.766	664.781	524.688	50.934	-64.962	-5.605	82.739
205.766	791.406	524.688	45.961	-46.571	-44.800	79.299
221.594	31.656	524.688	18.924	28.116	19.926	39.315
221.594	94.969	524.688	4.335	9.512	10.518	14.829

221.594	221.594	524.688	20.393	19.291	-38.736	47.838
221.594	474.844	524.688	20.106	-43.593	-55.595	73.453
221.594	538.156	524.688	80.429	3.995	-15.216	81.953
221.594	854.719	524.688	69.270	-93.294	-29.230	119.819
237.422	601.469	524.688	44.777	0.264	-30.607	54.239
237.422	664.781	524.688	66.790	-26.376	17.957	74.020
237.422	791.406	524.688	78.776	-2.366	25.584	82.860
269.078	664.781	524.688	49.825	-17.179	25.941	58.742
269.078	728.094	524.688	12.602	5.460	19.773	24.074
269.078	791.406	524.688	13.457	-48.916	-23.714	56.002
284.906	474.844	524.688	29.192	-9.303	-49.016	57.804
284.906	854.719	524.688	17.455	-15.725	6.347	24.336
284.906	918.031	524.688	37.676	-11.172	-27.115	47.745
284.906	31.656	524.688	-4.877	13.432	-37.145	39.799
284.906	601.469	524.688	36.612	-13.560	-6.958	39.658
300.734	664.781	524.688	-9.509	-21.590	-17.618	29.443
300.734	728.094	524.688	54.344	-41.079	6.220	68.406
300.734	791.406	524.688	88.695	-46.183	1.447	100.009
332.391	538.156	524.688	-19.513	-66.488	-43.629	81.883
332.391	664.781	524.688	32.168	-31.096	-28.417	53.002
332.391	728.094	524.688	47.216	-49.829	27.704	74.026
332.391	791.406	524.688	19.255	-19.745	-37.110	46.236
348.219	31.656	524.688	-17.568	14.940	-20.766	31.033
348.219	221.594	524.688	2.466	-17.530	-32.166	36.715
348.219	284.906	524.688	-26.656	-3.357	-53.966	60.284
348.219	474.844	524.688	49.493	-10.792	-35.147	61.655
348.219	601.469	524.688	8.003	-45.921	-17.258	49.705
348.219	854.719	524.688	43.362	14.330	-43.475	63.053
348.219	918.031	524.688	62.022	1.746	-16.523	64.209
364.047	538.156	524.688	47.238	38.059	-53.963	81.191
364.047	664.781	524.688	42.211	-36.164	-10.078	56.490
364.047	728.094	524.688	3.474	-26.075	6.677	27.140
364.047	791.406	524.688	68.339	-20.724	37.941	80.865
395.703	538.156	524.688	30.348	-56.972	-73.535	97.848
395.703	601.469	524.688	19.844	-15.917	-39.748	47.192
395.703	728.094	524.688	-15.546	-31.307	7.460	35.741
395.703	791.406	524.688	25.773	-2.647	23.283	34.834
395.703	918.031	524.688	71.048	-10.376	-66.036	97.551
411.531	158.281	524.688	-74.119	-2.481	-13.431	75.367
411.531	221.594	524.688	-58.753	-25.123	-38.942	74.830
411.531	474.844	524.688	47.332	17.578	-15.986	52.961

411.531	664.781	524.688	11.511	-1.944	-15.285	19.233
411.531	854.719	524.688	14.493	23.929	-28.720	40.093
427.359	538.156	524.688	11.962	-23.341	-68.824	73.653
427.359	601.469	524.688	69.919	-22.776	6.509	73.823
427.359	728.094	524.688	-81.734	-11.035	7.553	82.821
427.359	791.406	524.688	-1.063	17.666	-12.393	21.606
427.359	918.031	524.688	28.190	15.759	-17.175	36.579
459.016	221.594	524.688	-0.141	21.971	-53.207	57.565
474.844	158.281	524.688	27.627	-7.216	-48.793	56.534
474.844	601.469	524.688	2.193	-2.773	-40.506	40.660
474.844	664.781	524.688	9.642	17.158	-25.358	32.099
474.844	981.344	524.688	71.590	-21.360	-27.369	79.564
474.844	918.031	524.688	-7.328	17.125	-9.387	20.858
490.672	221.594	524.688	-0.312	-16.721	-60.156	62.437
538.156	94.969	524.688	-12.670	-38.684	-32.748	52.244
538.156	221.594	524.688	46.688	-40.690	-85.594	105.650
538.156	411.531	524.688	37.541	32.722	-23.919	55.246
538.156	538.156	524.688	-8.943	0.849	-112.489	112.847
538.156	601.469	524.688	25.463	-42.846	-26.402	56.402
538.156	728.094	524.688	27.746	9.051	20.739	35.803
538.156	791.406	524.688	-10.587	-25.386	-35.198	44.671
585.641	474.844	524.688	-14.503	3.418	-47.437	49.722
601.469	284.906	524.688	-38.240	-34.324	-62.529	80.934
601.469	411.531	524.688	19.538	20.350	-57.486	64.035
601.469	538.156	524.688	17.371	12.007	-39.878	45.124
601.469	601.469	524.688	-29.813	9.492	-2.898	31.421
601.469	664.781	524.688	11.964	1.522	-146.429	146.925
601.469	728.094	524.688	-51.018	-14.894	-43.931	68.954
601.469	791.406	524.688	36.758	-64.397	-17.902	76.280
601.469	918.031	524.688	39.338	-10.435	-34.787	53.539
617.297	474.844	524.688	-28.398	39.398	-42.986	64.857
648.953	728.094	524.688	-34.455	-9.993	-20.239	41.191
664.781	284.906	524.688	54.217	29.560	-63.151	88.325
664.781	601.469	524.688	7.115	-20.964	18.324	28.738
664.781	664.781	524.688	-6.386	-14.405	5.884	16.820
680.609	728.094	524.688	-1.539	-25.040	-33.176	41.594
728.094	348.219	524.688	29.099	7.971	34.774	46.038
728.094	411.531	524.688	39.783	52.383	-67.808	94.470
728.094	474.844	524.688	8.455	10.146	-71.683	72.890
728.094	854.719	524.688	-20.558	-32.613	-23.702	45.255
791.406	728.094	524.688	21.246	-39.598	-42.029	61.529

918.031	158.281	524.688	-15.819	-9.629	-23.842	30.189
553.984	364.047	353.594	35.125	15.422	-59.394	70.705
174.109	712.266	171.094	3.321	23.700	-28.375	37.119
427.359	680.609	171.094	-64.122	-36.805	-68.814	101.003
459.016	680.609	171.094	-39.566	-35.923	-53.136	75.362
553.984	585.641	171.094	-11.592	13.633	-101.960	103.519

Table 4-6: Average velocity information for areas close to the selected Z planes with respect to case 4 under non-isothermal condition

x (mm)	y (mm)	z (mm)	u (mm/s)	v (mm/s)	w (mm/s)	Magnitude(mm/s)
94.969	158.281	524.688	2.419	38.331	4.252	38.642
158.281	31.656	524.688	-10.243	19.313	12.652	25.258
158.281	94.969	524.688	-20.413	16.911	8.579	27.861
158.281	158.281	524.688	26.568	29.259	-34.078	52.185
158.281	221.594	524.688	13.933	10.563	8.119	19.277
158.281	474.844	524.688	45.971	-17.688	-91.036	103.507
205.766	158.281	524.688	33.580	3.994	-14.363	36.741
205.766	221.594	524.688	11.280	-2.090	-30.655	32.731
221.594	31.656	524.688	11.199	-18.612	-23.462	31.974
221.594	94.969	524.688	15.357	-12.562	-11.022	22.697
221.594	284.906	524.688	11.468	-18.090	-23.256	31.616
221.594	474.844	524.688	12.924	81.708	-6.940	83.014
221.594	538.156	524.688	-1.925	-17.553	-51.878	54.801
221.594	728.094	524.688	72.553	-8.016	-0.933	73.001
221.594	791.406	524.688	5.841	-12.304	-21.520	25.468
237.422	142.453	524.688	-21.585	27.592	-31.931	47.401
237.422	174.109	524.688	40.219	31.304	23.320	56.048
237.422	221.594	524.688	106.968	19.218	-14.337	109.623
269.078	158.281	524.688	13.577	5.568	-34.664	37.642
269.078	205.766	524.688	24.118	20.919	-25.699	40.985
269.078	237.422	524.688	-24.833	17.411	-32.456	44.421
269.078	474.844	524.688	-15.721	-71.465	-61.387	95.513
269.078	585.641	524.688	14.595	-23.239	-40.429	48.863
269.078	617.297	524.688	0.959	-34.545	-20.303	40.081
284.906	284.906	524.688	19.321	12.539	-37.758	44.229
284.906	411.531	524.688	70.889	-22.745	-49.050	89.154
284.906	538.156	524.688	-16.947	-22.805	-62.129	68.318
284.906	664.781	524.688	40.946	-33.047	-7.577	53.161
284.906	728.094	524.688	22.986	-22.344	-76.827	83.246
284.906	791.406	524.688	39.341	-17.264	-3.955	43.144
284.906	31.656	524.688	7.451	7.554	-5.143	11.791

284.906	94.969	524.688	29.251	2.965	-16.701	33.814
300.734	142.453	524.688	-10.435	-16.213	-31.311	36.771
300.734	174.109	524.688	-5.367	19.842	-1.683	20.623
300.734	221.594	524.688	9.179	-25.908	39.837	48.399
300.734	474.844	524.688	26.383	-77.478	-23.124	85.051
300.734	601.469	524.688	24.655	-83.249	3.567	86.896
332.391	158.281	524.688	8.760	-13.556	-43.813	46.691
332.391	601.469	524.688	7.309	-20.442	-80.921	83.783
348.219	31.656	524.688	12.297	4.425	-21.986	25.578
348.219	94.969	524.688	-48.976	58.558	-15.117	77.822
348.219	221.594	524.688	71.193	-56.476	-33.126	96.723
348.219	348.219	524.688	38.226	26.439	-36.075	58.836
348.219	474.844	524.688	44.665	-15.224	0.742	47.194
348.219	538.156	524.688	70.280	21.192	-48.004	87.708
348.219	664.781	524.688	-71.246	1.559	7.493	71.656
348.219	918.031	524.688	55.376	4.563	-44.953	71.471
364.047	158.281	524.688	-24.281	2.561	-34.811	42.520
364.047	601.469	524.688	37.953	-21.667	-68.368	81.143
395.703	221.594	524.688	45.648	31.494	-21.583	59.510
395.703	474.844	524.688	16.058	-0.131	-58.850	61.002
411.531	94.969	524.688	8.047	12.702	-8.035	17.049
411.531	158.281	524.688	27.308	-4.955	-30.791	41.453
411.531	348.219	524.688	8.066	0.243	-29.751	30.826
411.531	411.531	524.688	32.877	43.111	-5.461	54.491
411.531	538.156	524.688	85.154	-28.149	-19.423	91.765
411.531	601.469	524.688	-22.025	-49.411	-13.764	55.821
411.531	728.094	524.688	-0.843	-13.017	-2.359	13.256
411.531	854.719	524.688	14.868	2.116	-16.054	21.983
411.531	981.344	524.688	-18.946	6.446	-92.804	94.938
411.531	918.031	524.688	53.440	-3.476	-11.547	54.783
427.359	221.594	524.688	9.393	3.769	-4.893	11.242
427.359	474.844	524.688	45.199	-3.973	-38.063	59.225
459.016	174.109	524.688	-39.118	-6.160	-14.833	42.287
459.016	221.594	524.688	33.113	-33.352	-28.298	54.860
474.844	854.719	524.688	-118.870	15.422	-42.668	127.233
474.844	158.281	524.688	8.529	11.154	-12.739	18.958
490.672	221.594	524.688	15.355	22.305	-57.928	63.945
522.328	221.594	524.688	0.002	-22.964	-52.353	57.168
538.156	94.969	524.688	-28.935	-6.960	-68.050	74.273
538.156	284.906	524.688	113.331	11.139	-16.211	115.025
538.156	474.844	524.688	33.903	76.360	-101.499	131.462

538.156	538.156	524.688	1.984	-30.256	-63.116	70.021
538.156	601.469	524.688	1.399	0.542	16.818	16.885
538.156	854.719	524.688	1.035	-28.594	-2.846	28.754
538.156	158.281	524.688	18.079	23.063	-23.301	37.439
538.156	791.406	524.688	44.177	39.642	-34.502	68.655
553.984	221.594	524.688	56.444	-16.987	-69.055	90.791
585.641	158.281	524.688	78.181	-29.866	-37.869	91.860
585.641	221.594	524.688	-28.753	-30.533	-20.606	46.729
585.641	411.531	524.688	29.407	63.858	-14.594	71.803
585.641	538.156	524.688	6.025	11.880	-30.382	33.173
601.469	31.656	524.688	-56.452	-5.864	-66.390	87.344
601.469	94.969	524.688	21.067	0.561	24.406	32.246
601.469	284.906	524.688	29.213	35.048	-17.956	49.032
601.469	664.781	524.688	-7.422	-29.530	3.880	30.695
601.469	728.094	524.688	17.200	-15.052	-4.465	23.288
601.469	791.406	524.688	-13.730	-25.803	-26.971	39.772
601.469	854.719	524.688	28.978	0.242	-25.552	38.635
601.469	474.844	524.688	39.864	43.006	-46.943	75.115
601.469	601.469	524.688	-1.800	7.258	19.154	20.563
617.297	158.281	524.688	43.580	-39.376	-18.017	61.436
617.297	221.594	524.688	51.126	-15.779	-41.547	67.742
617.297	411.531	524.688	8.528	10.078	-10.630	16.950
617.297	538.156	524.688	42.937	-7.494	-61.077	75.034
648.953	221.594	524.688	-8.912	23.045	-37.195	44.654
664.781	158.281	524.688	-21.200	-16.662	-34.223	43.570
664.781	284.906	524.688	-4.598	1.612	-23.484	23.984
664.781	474.844	524.688	10.306	24.933	-16.658	31.707
664.781	538.156	524.688	-7.231	16.394	-34.639	38.999
664.781	791.406	524.688	-34.954	11.642	-31.776	48.652
664.781	411.531	524.688	-47.616	36.887	0.317	60.234
680.609	221.594	524.688	-35.839	-26.499	-58.932	73.889
712.266	94.969	524.688	15.483	-10.249	-83.305	85.349
728.094	158.281	524.688	-18.742	4.489	-24.495	31.168
728.094	221.594	524.688	20.958	3.495	-44.827	49.607
728.094	348.219	524.688	11.769	-41.520	-35.884	56.126
728.094	411.531	524.688	21.140	2.370	-39.732	45.068
728.094	474.844	524.688	69.533	-40.627	-17.949	82.507
728.094	854.719	524.688	37.673	-29.542	-16.769	50.726
743.922	94.969	524.688	15.083	-3.103	-19.333	24.717
791.406	94.969	524.688	-0.150	-6.531	-39.616	40.151
791.406	158.281	524.688	10.565	3.870	-12.525	16.837

791.406	221.594	524.688	13.470	27.763	-23.724	38.924
791.406	348.219	524.688	46.072	18.821	-27.089	56.663
791.406	411.531	524.688	35.357	-4.717	-52.563	63.524
791.406	474.844	524.688	-44.451	-31.901	-81.934	98.523
854.719	158.281	524.688	25.732	-32.646	-10.925	42.980
854.719	221.594	524.688	28.798	1.810	-40.662	49.860
854.719	284.906	524.688	5.488	-0.683	-35.163	35.596
918.031	158.281	524.688	0.423	-46.151	-31.279	55.754
918.031	348.219	524.688	94.152	-54.136	-111.802	155.868
205.766	364.047	353.594	40.224	16.281	-59.709	73.812
205.766	427.359	353.594	-9.343	-15.933	-51.497	54.709
205.766	459.016	353.594	-28.759	-12.267	-57.159	65.151
237.422	427.359	353.594	22.536	3.734	-48.285	53.416
395.703	459.016	353.594	-39.006	-3.083	-26.884	47.473
174.109	205.766	171.094	-28.660	1.439	-40.940	49.996
174.109	269.078	171.094	-7.646	49.531	-19.512	53.782
174.109	364.047	171.094	-1.054	20.007	-26.663	33.351
174.109	395.703	171.094	-18.712	-25.370	-59.567	67.395
205.766	395.703	171.094	-18.132	-3.871	-48.660	52.072
364.047	205.766	171.094	-19.086	11.457	-70.003	73.457

Table 4-7: Average velocity information for areas close to the selected Z planes with respect to case 2 under heat source condition

x (mm)	y (mm)	z (mm)	u (mm/s)	v (mm/s)	w (mm/s)	Magnitude(mm/s)
300.734	648.953	536.094	16.040	-43.833	-53.415	70.935
364.047	617.297	536.094	4.201	-29.981	-43.615	53.092
395.703	648.953	536.094	11.363	-68.596	-96.717	119.117
427.359	680.609	536.094	23.969	-43.106	40.034	63.525
617.297	553.984	536.094	-12.050	-67.652	-51.553	85.905
648.953	427.359	536.094	-4.729	10.986	-95.439	96.185
680.609	553.984	536.094	12.951	-19.101	-10.184	25.225
680.609	617.297	536.094	-8.090	-43.064	-56.474	71.479
680.609	680.609	536.094	-26.378	-47.089	-16.534	56.449
712.266	490.672	536.094	-10.218	-45.985	-44.568	64.849
712.266	553.984	536.094	-12.747	-41.084	-29.719	52.284
712.266	743.922	536.094	-57.823	-24.270	-10.095	63.517
712.266	838.891	536.094	-27.805	-48.343	31.390	63.996
743.922	743.922	536.094	-76.060	-40.347	-9.417	86.612
743.922	775.578	536.094	-16.763	-30.067	-16.813	38.310
775.578	522.328	536.094	-22.310	-34.409	-49.133	63.998
807.234	648.953	536.094	-39.069	-29.686	14.531	51.174

807.234	680.609	536.094	-35.596	-37.254	15.307	53.752
807.234	775.578	536.094	-7.932	-40.745	-3.225	41.635
830.977	617.297	536.094	-25.731	-73.137	4.774	77.678
838.891	553.984	536.094	-33.337	-27.053	-11.715	44.502
838.891	585.641	536.094	-14.816	-48.734	-19.414	54.511
846.805	617.297	536.094	9.500	-41.129	-42.634	59.996
870.547	648.953	536.094	-37.057	-51.079	-19.445	66.033
870.547	743.922	536.094	-13.665	-44.102	-5.254	46.468
870.547	807.234	536.094	-31.455	-52.331	14.865	62.841
300.734	870.547	353.594	49.299	-25.007	19.975	58.777
332.391	870.547	353.594	40.696	-35.703	45.640	70.808
364.047	617.297	353.594	51.311	-15.435	-64.768	84.059
395.703	269.078	353.594	-22.686	15.350	-108.050	111.468
395.703	617.297	353.594	7.371	-55.702	-76.060	94.563
395.703	680.609	353.594	27.999	-35.771	-74.009	86.838
427.359	585.641	353.594	32.354	-42.511	-79.573	95.843
427.359	680.609	353.594	10.849	-10.848	-63.926	65.741
459.016	870.547	353.594	26.269	-18.669	28.996	43.352
490.672	838.891	353.594	-30.694	3.492	-18.763	36.144
553.984	142.453	353.594	-22.782	-41.046	-43.783	64.194
553.984	838.891	353.594	9.078	1.006	-30.420	31.762
585.641	617.297	353.594	-30.220	-28.910	-69.089	80.761
585.641	680.609	353.594	-40.523	-17.792	-0.491	44.260
585.641	838.891	353.594	16.689	25.681	34.195	45.906
617.297	300.734	353.594	18.046	11.149	-103.244	105.401
617.297	459.016	353.594	-21.505	-27.217	-72.937	80.765
617.297	648.953	353.594	-13.739	-3.840	-76.787	78.101
617.297	680.609	353.594	-32.702	-22.328	-61.006	72.730
617.297	807.234	353.594	-7.887	-16.481	-6.709	19.464
648.953	79.141	353.594	0.483	22.619	-26.242	34.648
648.953	237.422	353.594	3.497	-25.691	-59.648	65.039
648.953	395.703	353.594	-2.876	-7.532	-81.769	82.165
648.953	427.359	353.594	1.195	-21.730	-83.557	86.344
648.953	680.609	353.594	-16.593	4.167	-28.238	33.016
648.953	775.578	353.594	-51.304	21.364	-53.528	77.161
648.953	838.891	353.594	-18.328	23.486	-51.595	59.578
680.609	174.109	353.594	-26.957	-35.292	-73.315	85.716
680.609	395.703	353.594	4.382	16.311	-39.207	42.691
680.609	680.609	353.594	-1.885	-32.140	-15.910	35.912
680.609	775.578	353.594	-59.919	0.923	-21.011	63.503
704.352	427.359	353.594	-3.913	0.070	-51.953	52.101

712.266	395.703	353.594	-12.725	-7.951	-53.921	55.970
712.266	807.234	353.594	-39.841	-22.025	23.191	51.091
720.180	427.359	353.594	-33.488	12.490	-37.564	51.851
743.922	174.109	353.594	-35.313	-34.915	-32.089	59.125
743.922	300.734	353.594	-31.749	-2.243	-68.558	75.586
743.922	332.391	353.594	-7.260	38.411	-78.475	87.672
743.922	395.703	353.594	-11.524	-4.397	-79.219	80.173
743.922	427.359	353.594	-17.342	19.490	-50.697	57.016
743.922	459.016	353.594	-25.592	21.252	-72.585	79.845
743.922	490.672	353.594	-25.543	34.583	-101.115	109.876
743.922	648.953	353.594	-39.706	-25.189	-42.986	63.709
743.922	712.266	353.594	-25.093	-5.114	-42.111	49.286
775.578	364.047	353.594	-34.452	-0.551	-79.203	86.374
775.578	427.359	353.594	-13.902	-2.053	-56.606	58.324
775.578	459.016	353.594	-22.465	-0.685	-87.171	90.021
775.578	585.641	353.594	-23.481	-14.381	-80.466	85.047
775.578	648.953	353.594	-55.939	9.892	-55.561	79.461
807.234	269.078	353.594	-37.684	11.167	-8.768	40.269
807.234	332.391	353.594	-6.448	-25.742	-56.725	62.625
807.234	427.359	353.594	-22.757	14.325	-85.943	90.052
807.234	459.016	353.594	-4.366	-16.020	-90.568	92.077
807.234	617.297	353.594	-44.866	0.619	-57.907	73.256
807.234	712.266	353.594	-43.074	-29.983	-20.303	56.272
838.891	364.047	353.594	-40.304	-13.237	-49.341	65.070
838.891	395.703	353.594	-24.114	-6.139	-60.490	65.408
838.891	427.359	353.594	-33.277	22.115	-57.960	70.397
838.891	459.016	353.594	-59.940	16.881	-77.497	99.416
838.891	522.328	353.594	-12.665	-8.737	-71.493	73.130
870.547	459.016	353.594	-2.156	-26.962	-69.996	75.040
870.547	743.922	353.594	-29.401	-22.615	2.764	37.195
902.203	743.922	353.594	-35.427	-20.237	-3.910	40.987
933.859	395.703	353.594	-5.128	-21.686	-43.047	48.473
237.422	332.391	171.094	-83.069	37.231	-88.636	127.055
300.734	395.703	171.094	-12.411	17.438	-62.957	66.496
332.391	585.641	171.094	5.419	6.405	-58.996	59.590
332.391	617.297	171.094	34.695	16.989	-96.512	103.956
332.391	838.891	171.094	-34.335	-1.156	-21.158	40.347
364.047	712.266	171.094	18.099	-9.981	-68.820	71.857
427.359	617.297	171.094	20.764	-0.425	-109.113	111.072
427.359	648.953	171.094	23.689	3.555	-62.734	67.152
427.359	712.266	171.094	34.922	-7.254	-51.299	62.480

459.016	680.609	171.094	20.431	11.194	-63.758	67.881
522.328	712.266	171.094	15.675	13.901	-66.732	69.943
553.984	237.422	171.094	-29.587	-10.790	-91.053	96.346
553.984	680.609	171.094	0.092	59.503	-68.009	90.365
553.984	712.266	171.094	9.529	-2.969	-65.278	66.036
585.641	142.453	171.094	34.425	7.906	-83.499	90.663
585.641	174.109	171.094	12.622	-13.711	-43.926	47.715
585.641	617.297	171.094	-22.721	-12.519	-72.494	76.996
585.641	648.953	171.094	-34.341	-7.465	-61.455	70.794
585.641	680.609	171.094	-32.973	41.224	-35.590	63.666
585.641	712.266	171.094	-20.215	34.083	-39.275	55.793
585.641	838.891	171.094	38.968	33.010	-34.687	61.736
617.297	553.984	171.094	-40.793	10.184	-92.443	101.555
617.297	775.578	171.094	-36.978	37.274	-36.959	64.208
617.297	712.266	171.094	-19.541	15.492	-50.035	55.904
648.953	142.453	171.094	0.743	-22.154	-94.409	96.976
648.953	459.016	171.094	-30.838	-0.015	-60.440	67.852
648.953	522.328	171.094	-34.318	13.578	-93.207	100.248
648.953	585.641	171.094	-6.977	19.509	-77.697	80.412
648.953	617.297	171.094	-46.881	28.899	-40.629	68.437
648.953	680.609	171.094	-35.221	2.812	-54.239	64.732
648.953	743.922	171.094	-55.836	35.325	-22.613	69.835
672.695	617.297	171.094	-10.080	34.566	-59.490	69.538
672.695	648.953	171.094	-29.440	29.025	-32.885	52.826
672.695	712.266	171.094	0.938	21.266	-32.881	39.170
680.609	174.109	171.094	-2.298	-31.368	-70.416	77.121
680.609	459.016	171.094	-34.317	36.548	-107.290	118.425
680.609	490.672	171.094	-25.776	52.728	-86.244	104.320
680.609	522.328	171.094	-22.930	23.645	-99.034	104.367
680.609	585.641	171.094	-20.776	4.683	-51.908	56.107
680.609	680.609	171.094	-40.067	52.157	-65.475	92.805
680.609	743.922	171.094	-1.833	68.222	4.515	68.395
688.523	617.297	171.094	-52.708	33.956	-89.019	108.883
688.523	648.953	171.094	-36.451	18.237	-42.500	58.886
688.523	712.266	171.094	4.420	42.179	-35.418	55.254
712.266	142.453	171.094	41.366	-11.278	-88.170	98.043
712.266	459.016	171.094	-20.061	14.334	-96.725	99.818
712.266	490.672	171.094	-27.976	40.097	-113.873	123.925
712.266	522.328	171.094	-29.841	19.384	-65.912	74.904
712.266	553.984	171.094	-20.731	62.768	-54.210	85.489
712.266	585.641	171.094	-46.758	33.947	-80.545	99.127

712.266	648.953	171.094	-81.715	17.942	-69.743	108.919
712.266	617.297	171.094	-26.347	27.750	-48.342	61.654
712.266	680.609	171.094	-40.367	4.663	-86.550	95.615
736.008	553.984	171.094	-0.904	12.501	-75.182	76.220
736.008	648.953	171.094	-28.111	18.275	-92.256	98.160
743.922	395.703	171.094	-26.973	36.272	-104.288	113.662
743.922	427.359	171.094	-14.560	27.199	-77.816	83.708
743.922	459.016	171.094	-29.044	34.989	-100.291	110.119
743.922	490.672	171.094	-33.382	31.569	-89.265	100.395
743.922	585.641	171.094	-47.062	39.945	-78.469	99.839
743.922	617.297	171.094	-43.053	24.576	-93.439	105.775
743.922	712.266	171.094	-3.192	-1.156	-43.171	43.304
743.922	775.578	171.094	-40.553	-22.619	-18.355	49.931
751.836	553.984	171.094	-21.594	44.276	-81.655	95.363
751.836	648.953	171.094	-30.127	27.231	-49.535	64.054
775.578	395.703	171.094	-40.940	2.615	-68.107	79.508
775.578	553.984	171.094	-58.630	24.002	-95.699	114.768
775.578	680.609	171.094	1.680	51.396	-54.904	75.225
775.578	743.922	171.094	-22.825	-1.540	-75.982	79.351
807.234	205.766	171.094	36.257	38.965	-74.779	91.787
807.234	395.703	171.094	1.701	34.453	-82.734	89.637
807.234	522.328	171.094	-46.346	51.533	-51.592	86.402
807.234	585.641	171.094	-51.402	22.249	-46.681	72.913
807.234	743.922	171.094	-41.371	10.734	-73.740	85.231
838.891	585.641	171.094	4.565	-43.543	-46.428	63.815
838.891	680.609	171.094	-24.900	-0.316	-29.409	38.535
838.891	743.922	171.094	-37.618	-10.908	-54.182	66.857
838.891	775.578	171.094	-77.657	39.673	-72.507	113.410
902.203	743.922	171.094	-19.755	37.679	-4.054	42.737

Conclusions and perspectives

L'objectif de cette thèse est de promouvoir les applications de la technologie 3D PTV pour l'étude d'écoulement d'air intérieur; donc quatre principaux travaux de recherche sont faits dans la thèse. Tout d'abord, la technologie PTV typique et ses principales applications antérieures pour les champs d'écoulement d'air intérieur sont examinées. Grâce à cet examen, l'équipement et les méthodes de PTV typique pour les applications d'écoulement d'air intérieur sont introduits systématiquement, y compris le système d'éclairage, les particules de traceurs, l'appareil d'enregistrement d'image et les algorithmes de suivi. En outre, les limitations et les développements futurs de la technologie PTV pour les champs d'écoulement d'air intérieur sont discutés. Cet examen montre comment l'information d'écoulement turbulent quantitative et détaillée obtenue par mesure PTV est critique pour l'analyse des propriétés de turbulence et le développement de simulations numériques. Il suggère également que les procédures PTV conviviales et les algorithmes de suivi rapides sont les deux affaires importantes pour le développement futur de la technologie PTV pour les champs d'écoulement d'air intérieur.

La deuxième partie de cette thèse évalue les performances de mesure des algorithmes 3D PTV et des algorithmes de PIV typiques. Tout différemment des études antérieures, l'évaluation se fait du point de vue de la densité de suivi, l'indice qui reflète la difficulté du suivi. Les performances de mesure d'un algorithme de corrélation croisée typique de la 2D PIV et d'un algorithme de corrélation croisée modifié de la 3D PTV sont comparés numériquement et expérimentalement. Les résultats numériques suggèrent que la densité de suivi a une influence directe et importante sur des résultats de mesure en PIV typique et en 3D PTV. Lorsque la densité de suivi est inférieure à 2, la PTV ne peut généralement pas donner de résultats fiables. Mais quand la densité de suivi augmente, la 3D PTV a une précision similaire, et une meilleure capacité à mesurer les déplacements que la 2D PIV typique. Par conséquent, la pré-évaluation d'une densité de suivi appropriée peut avoir un impact significatif sur le processus de mesure.

La troisième partie vise à comparer les performances de plusieurs algorithmes complets de mesure 3D PTV, afin de décider de l'algorithme optimal à utiliser pour la recherche expérimentale, en ce qui concerne les caractéristiques d'écoulement. Dans cette partie, les performances des sept algorithmes complets de la 3D PTV sont évaluées, les différences entre les algorithmes sont générées par différents algorithmes de suivi temporel et méthodes de correspondance spatiales. L'évaluation se fait numériquement sur deux types d'écoulements tridimensionnels, laminaire et macro à l'échelle des solutions de Navier-Stokes connues. La comparaison est basée sur l'exactitude, le nombre de trajectoires détectées, et la longueur maximale des trajectoires de chaque algorithme en fonction de la densité de suivi des particules et du nombre total d'images. Les résultats des tests numériques montrent que les performances de la plupart des algorithmes de mesure 3D PTV augmentent à mesure que la densité de suivi des particules augmente. Quand le nombre d'images suivies augmente, les

performances de tous les algorithmes de mesure sont clairement diminuées. Il suggère qu'en répartissant le nombre total d'images en des ensembles de plus petite taille et en réinitialisant le suivi sur chaque groupe, on peut améliorer la précision de tout algorithme de mesure 3D PTV. Par ailleurs, les résultats montrent également que les algorithmes utilisant la contrainte épipolaire plutôt que la méthode de correspondance spatiale ont généralement de meilleures performances. Il est à noter que les algorithmes ayant la capacité de fournir le plus de trajectoires de particules n'ont pas nécessairement la meilleure précision de suivi. Les algorithmes de mesure qui ont de meilleures performances sont ensuite comparés expérimentalement à un écoulement d'air tridimensionnel réel dans une cavité cubique. Les résultats se sont avérés similaires à ceux fournis par l'étude numérique.

La dernière partie a consisté à conduire l'investigation expérimentale pour obtenir la distribution d'écoulement d'air à l'intérieur, en utilisant la technologie 3D PTV basée sur l'analyse réalisée dans les parties précédentes. Dans cette partie, l'écoulement d'air intérieur réel généré avec la méthode de ventilation de mélange est mesuré. L'investigation est effectuée pour connaître l'état isotherme, l'état anisotherme, et l'état d'une source de chaleur. Sur la base des analyses antérieures, deux algorithmes 3D PTV sont appliqués dans cette partie pour mesurer les vitesses d'écoulement d'air intérieur. Des thermocouples sont utilisés pour mesurer la température d'écoulement d'air pour les états anisothermes et une source de chaleur. Grâce aux mesures expérimentales, les trajectoires, la vitesse et la température pour l'écoulement d'air sont obtenues. D'après ces résultats, certaines structures d'écoulement d'air sont détectées. Une méthode est proposée pour ensuite traiter les résultats expérimentaux originaux, afin de générer l'indice de référence expérimental pour la validation et le développement des modèles CFD à l'avenir.

Afin de promouvoir les applications de la technologie 3D PTV à l'étude de l'écoulement d'air intérieur, il y a encore plusieurs points qui doivent être améliorés.

Le premier est le développement continu des algorithmes de mesure. Les algorithmes peuvent être étendus pour traiter le domaine de mesure plus grande rencontré dans les bâtiments réels, ce qui signifie que plusieurs caméras peuvent être utilisées simultanément pour prendre les images sous plusieurs angles. Par ailleurs, le temps de traitement des algorithmes devrait être largement réduit, afin d'augmenter la disponibilité de cette technologie. En outre, une plate-forme complète, y compris les différents algorithmes de mesure peut être développée, afin que, grâce à cette plate-forme, les chercheurs puissent sélectionner les algorithmes appropriés en fonction de leurs besoins de recherche.

Parce que l'un des objectifs importants de la mesure expérimentale est de fournir des données pour la validation et le développement des modèles CFD, le deuxième point est de développer une méthode pour traiter et afficher les résultats originaux en représentation Lagrangienne afin que ces résultats puissent être facilement utilisés par les chercheurs de CFD. La dernière tâche d'aborder, dans une perspective plus longue, est la thermométrie par image de particules (PIT) dans les domaines de l'air intérieur, ce qui signifie la mesure simultanée de la vitesse et de la température Lagrangiennes. Par conséquent, les particules spéciales qui peuvent refléter la variance de la température dans l'écoulement d'air intérieur doivent être recherchés ou développés.

Conclusions and perspectives

The aim of this thesis is to promote the applications of 3D PTV technology in indoor airflow study; therefore, four main research works are conducted in the thesis. First, the typical PTV technology and its previous main applications for indoor airflow field are reviewed. Through this review, the typical PTV equipment and methods for indoor airflow applications are introduced systematically, including the illumination system, tracer particles, image recording devices and tracking algorithms. Besides, the limitations and future developments of PTV technology for indoor airflow fields are discussed. This review shows how the quantitative and detailed turbulent flow information obtained by PTV measurement is critical for analyzing turbulent properties and developing numerical simulations. It also suggests that user-friendly PTV procedures and fast tracking algorithms are the two important issues for the development of PTV technology for indoor airflow fields in the future.

The second part of this thesis evaluates the measuring performance of 3D PTV algorithms and typical PIV algorithms. Different to previous studies, the evaluation is done based on the perspective of tracking density, the index which reflects the tracking difficulty. The measuring performance of a typical 2D PIV cross-correlation algorithm and the 3D PTV modified cross-correlation algorithm are compared numerically and experimentally. The numerical results suggest that the tracking density has direct and important influence on typical PIV and 3D PTV measurement results. When the tracking density is smaller than 2, PTV generally cannot give the reliable results. But as the tracking density increases, 3D PTV has similar accuracy, and a better ability to measure larger displacement than typical 2D PIV. Therefore, pre-evaluating an appropriate tracking density may have a significant impact on the measurement process.

The third part aims at comparing the performances of several complete 3D PTV measurement algorithms, in order to decide the optimal algorithm to use for the experimental investigation with respect to the flow characteristics. In this part, the performances of seven complete 3D PTV algorithms is evaluated, the differences among the algorithms are generated by different temporal tracking algorithms and spatial matching methods. The evaluation is done numerically on two types of three dimensional laminar macro scale flows of known Navier-Stokes solutions. The comparison is based on the accuracy, the measuring volume coverage, and the achievable trajectory length of each algorithm with respect to the particle tracking density and the total number of frames. The results of numerical tests show that the performance of most 3D PTV measurement algorithms increases as the tracking density increases. As the number of tracked frames increases, the performance of all measurement algorithms is clearly diminished. It suggests that dividing the total number of frames into sets of smaller number of frames and reinitializing the tracking on each set may improve the accuracy of any 3D PTV measurement algorithm. Besides, the results also show that the algorithms employing the epipolar constraint as the spatial matching method generally have better performance. It is noted that the algorithms with the ability to provide longer particle trajectory have not necessarily the better tracking accuracy. The measurement

algorithms with better performances are further compared on the experimental measurement of a real three dimensional airflow in a cubic cavity. Results similar to the numerical study are found.

The last part is to conduct the experimental investigation of indoor airflow distribution using 3D PTV technology based on the analysis in previous parts. In this part, the real indoor airflow generated by mixing ventilation method is measured. The investigation is done for isothermal condition, non-isothermal condition, and heat source condition. Based on the previous analyses, two 3D PTV algorithms are applied in this part to measure the indoor airflow velocities. And thermocouples are employed to measure the airflow temperature for non-isothermal condition and heat source condition. Through the experimental measurements, the airflow trajectories, velocity and temperature are obtained. From these results, some airflow structures are detected. A method is proposed to further process the original experimental results, in order to generate the experimental data benchmark for validating and developing CFD models in the future.

In order to promote the applications of 3D PTV technology in indoor airflow study, there are still several points which should be further improved. The first is the continuous development of the measurement algorithms. The algorithms can be expanded to process the much larger measurement domain in real buildings, which means that more cameras can be used simultaneously to take the images from more views. Besides, the processing time of algorithms should be largely reduced, to increase the availability of this technology. Furthermore, a comprehensive platform including different measurement algorithms may be developed, so that through this platform, researchers can select the suitable algorithms based on their research needs.

Because one important aim of experimental measurement is to provide data for validating and developing the CFD models, the second point is to develop a method to process and display the original Lagrangian results so that these results can be easily used by CFD researchers. The last task to tackle, in a longer perspective, is particle image thermometry in the indoor air fields, which means the simultaneous measurement of Lagrangian velocity and temperature. Therefore, special particles which can reflect the temperature variance in the indoor airflow should be searched or developed.

Bibliography / Bibliographie

- [1] Lean HH, Smyth R. CO₂ emissions, electricity consumption and output in ASEAN. *Appl Energy* 2010; 87 (11): 1858-64.
- [2] Chang CC. A multivariate causality test of carbon dioxide emissions, energy consumption and economic growth in China. *Appl Energy* 2010; 87(11): 3533-37.
- [3] Govindaraju VGRC, Tang CF. The dynamic links between CO₂ emissions, economic growth and coal consumption in China and India. *Appl Energy* 2013; 104:310-8.
- [4] Sharma SS. Determinants of carbon dioxide emissions: empirical evidence from 69 countries. *Appl Energy* 2011; 88:376-82.
- [5] Pérez-Lombard L, Ortiz J, Pout C. A review on buildings energy consumption information. *Energ Build* 2008; 40:394-8.
- [6] European Parliament and Council. Directive 2010/31/EU of the European Parliament and of the Council of 19 May 2010 on the energy performance of buildings. *Official Journal of the European Union*, L153 (2010): 13-35.
- [7] ODYSSEE and MURE. Energy efficiency trends and policies in the household and tertiary sectors. June 2015.
- [8] Lim TS, Schaefer L, Kim JT, Kim G. Energy benefit of the underfloor air distribution systems for reducing air-conditioning and heating loads in buildings. *Indoor Built Environ* 2012; 21(1): 62-70.
- [9] Li X, Niu J, Gao N. Co-occupants's exposure to exhaled pollutants with two types of personalized ventilation strategies under mixing and displacement ventilation systems. *Indoor Air* 2013; 23(2): 162-71.
- [10] Li Y, Leng GM, Tang JW, Yang X, Chao CYH, Lin JZ et al. Role of ventilation in airborne transmission of infectious agents in the built environment - a multidisciplinary systematic review. *Indoor Air* 2007; 17(1): 2-18.
- [11] Chen Q. Ventilation performance prediction for buildings: A method overview and recent applications. *Build Environ* 2009; 44(4): 848-58.
- [12] Li Y, Nielsen PV. CFD and ventilation research. *Indoor Air* 2011; 21: 442-53.
- [13] Sun Y, Zhang Y. An overview of room air motion measurement: technology and application. *HVAC & R Res* 2007; 13(6): 929-50.
- [14] Cao X, Liu J, Jiang N, Chen Q. Particle image velocimetry measurement of indoor airflow field: A review of the technologies and application. *Energ Build* 2014; 69: 367-80.
- [15] Etheridge DW, Sandberg M. *Building Ventilation: Theory and Measurement*. London: Wiley; 1996.
- [16] Awbi HB. *Ventilation systems: design and performance*. London: Taylor & Francis; 2007.
- [17] Niachou. K, Hassid. S, Santamouris. M, Livada. I. Experimental performance investigation of natural, mechanical and hybrid ventilation in urban environment. *Build Environ* 2008; 43(8): 1373-82.
- [18] Chen. Q, Lee. K, Mazumdar. S, Poussou. S, Wang. L, Wang. M, et al. Ventilation performance prediction for buildings: Model assessment. *Build Environ* 2010; 45(2): 295-303.

- [19] Kato. S, Ito. K, Murakami. S. Analysis of visitation frequency through particle tracking method based on LES and model experiment. *Indoor Air* 2003; 13(2):182-93.
- [20] Zhai. Z, Johnson. M-H, Krarti. Assessment of natural and hybrid ventilation models in whole-building energy simulations. *Energ Buildings* 2011; 43(9): 2251-61.
- [21] Schulze. T, Eicker. U. Controlled natural ventilation for energy efficient buildings. *Energ Buildings* 2013; 56: 221-32.
- [22] Homod. R, Sahari. K. S. M. Energy savings by smart utilization of mechanical and natural ventilation for hybrid residential building model in passive climate. *Energ Buildings* 2013; 60: 310-29.
- [23] Ji. Y, Lomas. K. J, Cook. M. J. Hybrid ventilation for low energy building design in south China. *Build Environ* 2009; 44(11): 2245-55.
- [24] Menassa. C. C, Taylor. N, Nelson. J. Optimizing hybrid ventilation in public spaces of complex buildings - A case study of the Wisconsin Institutes for Discovery. *Build Environ* 2013; 61: 57-68.
- [25] Lomas. K. J, Cook. M. J, Fiala. D. Low energy architecture for a severe US climate: Design and evaluation of a hybrid ventilation strategy. *Energ Buildings* 2007; 39(1): 32-44.
- [26] Seppänen. O. Ventilation Strategies for Good Indoor Air Quality and Energy Efficiency. *Int J Vent* 2008; 6(4): 297-306.
- [27] Biwole. P. H, Yan. W, Zhang. Y, Roux J-J. A complete 3D particle tracking algorithm and its applications to the indoor airflow study. *Meas Sci Technol* 2009; 20(11): 1154-66.
- [28] Robben. F, Cheng. R. K, Popovich. M. M, Weinberg. F. J. Associating particle tracking with laser fringe anemometry. *J Phys E: SciInstrum* 1980; 13(3): 315-22.
- [29] Suzuki. Y, Kasagi. N. Turbulent air-flow measurement with the aid of 3-D Particle Tracking Velocimetry in a curved square bend. *Flow Turbul Combust* 1999; 63 (1-4): 415-22.
- [30] Lee. S. J, Kim. S. Simultaneous measurement of size and velocity of microbubbles moving in an opaque tube using an X-ray particle tracking velocimetry technique. *Exp Fluids* 2005; 39 (3): 492-7.
- [31] Virant. M, Dracos. T. 3D PTV and its application on Lagrangian motion. *Meas Sci Technol* 1997; 8 (12): 1539-52.
- [32] Holzner. M, Liberzon. A, Nikitin. N, Lüthi. B, Kinzelbach. W, Tsinober. A. A Lagrangian investigation of the small-scale features of turbulent entrainment through particle tracking and direct numerical simulation. *J Fluid Mech* 2008; 598: 465-75.
- [33] Kim. S, Lee. S. J. Measurement of Dean flow in a curved micro-tube using micro digital holographic particle tracking velocimetry. *Exp Fluids* 2009; 46 (2): 255-64.
- [34] Satake. S, Kunugi. T, Sato. K, Ito. T, Kanamori. H, Taniguchi. J. Measurements of 3D flow in a micro-pipe via micro digital holographic particle tracking velocimetry. *Meas Sci Technol* 2006; 17(7): 1647-51.
- [35] Loomans. M. The measurement and simulation of indoor air flow [Ph.D. Thesis]. The Netherlands: Eindhoven University of Technology; 1998.
- [36] Mass. H. G, Gruen. A, Papantoniou. D. Particle tracking velocimetry in three-dimensional flows-Part 1: photogrammetric determination of particle coordinates. *Exp Fluids* 1993; 15(2): 133-46.

- [37] Malik. N. A, Dracos. Th, Papantoniou. D. A. Particle tracking velocimetry in three-dimensional flows-Part 2: particle tracking. *Exp Fluids* 1993;15(4-5): 279-94.
- [38] Khalighi. B, Lee. Y. H. Particle tracking velocimetry: an automatic image processing algorithm. *Appl Optics* 1989; 28(20): 4328-32.
- [39] Adrian. R.J. Particle-imaging techniques for experimental fluid mechanics. *Annu Rev Fluid Mech* 1991; 23: 264-304.
- [40] Willneff. J, Gruen. A. A new spatio-temporal matching algorithm for 3D-Particle Tracking Velocimetry. In: *Proceeding of The 9th International Symposium on Transport Phenomena and Dynamics of Rotating Machinery*, Honolulu, USA, Feb 10-14,2002.
- [41] Doh. D. H, Hwang. T. G, Saga. T. 3D-PTV measurements of the wake of a sphere. *Meas Sci Technol* 2004; 15(6): 1059-66.
- [42] Jones. J.D.C, Andersen.D.J, Greated C.A. Fibre-optic beam delivery systems for particle image velocimetry. *Opt Laser Eng* 1997; 27(6): 657-74.
- [43] Sun.Y, Zhang.Y, Wang.A, Jennifer L. T, James S. B, Besant R.W. Experimental characterization of airflows in aircraft cabins. Part I: Experimental system and measurement procedure. *ASHRAE T* 2005; 111(2): 45-52.
- [44] Sun.Y. Volumetric particle streak-tracking velocimetry and its application in indoor airflow measurements [Ph.D. Thesis]. USA: University of Illinois at Urbana-Champaign; 2007.
- [45] Biwole. P. H. Large-scale particle tracking velocimetry for 3-dimensional indoor airflow study [Ph.D. Thesis]. France: Institut National des Sciences Appliquées - Lyon; 2009.
- [46] Yan. W. Development of hybrid particle tracking algorithms and their applications in airflow measurement within aircraft cabin mock-up [Ph.D. Thesis]. USA: University of Illinois at Urbana-Champaign; 2010.
- [47] Lobutova. E, Resagk. C, Putze. T. Investigation of large-scale circulations in room air flows using three-dimensional particle tracking velocimetry. *Build Environ* 2010; 45(7): 1653-62.
- [48] Steinhoff. P, Schmidt. M, Müller. D. Redesign of a 3D PTV system with ANDOR's Neo sCMOS. Germany: Institute for Energy Efficient Buildings and Indoor Climate (EBC), RWTH Aachen University, 2013.
- [49] Barker D. Development of A Scalable Real-Time Lagrangian Particle Tracking System For Volumetric Flow Field Characterization [Ph.D. Thesis]. USA: University of Illinois at Urbana-Champaign; 2012.
- [50] Melling A. Tracer particles and seeding for particle image velocimetry. *Meas Sci Technol* 1997; 8: 1406-16.
- [51] Kessler. M, Leith. D. Flow measurement and efficiency modeling of cyclones for particle collection. *Aerosol Sci Tech* 1991; 15(1): 8-18.
- [52] Muller.R.H.G, Rotger.Th, Rotger.Th, Schaumann.O, Markwart.M. Large body aircraft cabin A/C flow measurement by helium bubble tracking. *J Flow Visualization* 1997; 4(3): 295-306.
- [53] Zhao. L, Zhang. Y, Wang. X, Riskowski. G. L, Christianson. L. L. Measurement of airflow patterns in ventilated spaces using particle image velocimetry. In: *ASAE/CSAE Annual International Meeting*, Toronto, Canada, 1999.

- [54] Machacek. M. A quantitative visualization tool for large wind tunnel experiments [Ph.D. Thesis]. Switzerland: ETH zürich; 2002.
- [55] Ma. B, Ruwet. V, Corieri. P, Theunissen. R, Riethmuller. M, Darquenne. C. CFD simulation and experimental validation of fluid flow and particle transport in a model of alveolated airways. *J Aerosol Sci* 2009; 40(5): 403-14.
- [56] Bosbach. J, Kuhn. M, Wagner. C. Large-scale particle image velocimetry with helium filled soap bubbles. *Exp Fluids* 2009; 46(3): 539-47.
- [57] Okuno. Y, Fukuda. T, Miwate. Y, Kobayashi. T. Development of three dimensional air flow measuring method using soap bubbles. *JSAE Rev* 1993; 14(4): 50-5.
- [58] Maxey M.R, Riley. J.J. Equation of motion of a small rigid sphere in a nonuniform flow. *Phys Fluids* 1983; 26(4): 883-9.
- [59] Kerho. M.F, Bragg. M.B. Neutrally buoyant bubbles used as flow tracers in air. *Exp Fluids* 1994; 16(6): 393-400.
- [60] Ouellette. N.T, O'Malley. P. J, Gollub. J. P. Transport of finite-sized particles in chaotic flow. *Phys Rev Lett* 2008; 101(17): 174504 (1-4).
- [61] Lobutova. E, Resagk. C, Rank. R, Dirk. Müller. Extended three dimensional particle tracking velocimetry for large enclosures. In: Nitsche. W, Dobriloff. C. *Imaging Measurement Methods for Flow Analysis*. Berlin: Springer; 2009, pp. 113-24.
- [62] Agüi. J, Jiménez. J. On the performance of particle tracking. *J Fluid Mech* 1987; 185: 447-68.
- [63] Hain. R, Kahler. C. J, Tropea. C. Comparison of CCD, CMOS and intensified cameras. *Exp Fluids* 2007; 42(3): 403-11.
- [64] Ouellette. N. T, Xu. H, Bodenschatz. E. A quantitative study of three-dimensional Lagrangian particle tracking algorithms. *Exp Fluids* 2006; 40(2): 301-13.
- [65] Okamoto. K, Nishio. S, Kobayashi. T, Saga. T, Takehara. K. Evaluation of the 3D-PIV Standard Images (PIV-STD Project). *J Visual-Japan* 2000; 3(2): 115-23.
- [66] Zhang. Z. Flexible camera calibration by viewing a plane from unknown orientations. In: *Proceedings of the 17th IEEE International Conference on Computer Vision (ICCV'99)*, Corfu, Greece, Sep 20-27, 1999.
- [67] Li D. Numerical and experimental study of volumetric particle tracking velocimetry in a spatial and temporal domain [Ph.D. Thesis]. USA: University of Illinois at Urbana-Champaign; 2008.
- [68] Svoboda. T, Martinec. D, Pajdla. T. A convenient multi-camera self-calibration for virtual environments. *Presence: Teleop Virt* 2005; 14(4): 407-22.
- [69] Resagk. C, Lobutova. E, Rank. R, Müller. D, Putze. T, Maas. H-G. Measurement of large-scale flow structures in air using a novel 3D particle tracking velocimetry technique. In: *13th International Symposium on Applications of Laser Techniques to Fluid Mechanics*, Lisbon, Portugal, June 26-29, 2006.
- [70] Doh. D. H, Kim. D. H, Choi. S. H, Hong. S. D, Saga. T, Kobayashi. T. Single-frame (two-field image) 3-D PTV for high speed flows. *Exp Fluids* 2000; 29(1): 85-98.
- [71] Mann. J, Ott. S, Anderson. J. S. Experimental Study of Relative, Turbulent Diffusion, Riso National Laboratory Report, Riso-R-1036(EN), 1999.

- [72] Nobach. H, Honkanen. M. Two-dimensional Gaussian regression for sub-pixel displacement estimation in particle image velocimetry or particle position estimation in particle tracking velocity. *Exp Fluids* 2005; 38(4): 511-15.
- [73] Zhao. L, Zhang. Y, Wang. X, Riskowski, Gerald. L. Analysis of airflow in a full-scale room with non-isothermal jet ventilation using PTV techniques. *ASHRAE T* 2007; 113(1): 414-25.
- [74] Yan. W, Zhang. Y, Sun. Y, Li. D. Experimental and CFD study of unsteady airborne pollutant transport within an aircraft cabin mock-up. *Build Environ* 2009; 44(1): 34-43.
- [75] Barker. D, Lifflander. J, Arya. A, Zhang. Y. A parallel algorithm for 3D particle tracking and Lagrangian trajectory reconstruction. *Meas Sci Technol* 2012; 23(2): 025301(1-14).
- [76] Klimentjew. D, Flick. N. E, Bosselmann. T, Zhang J. 3D hypergraph-oriented air flow analysis based on PTV. In: *Proceedings of the 2010 IEEE International Conference on Information and Automation*, Harbin, China, June 20-25, 2010.
- [77] Klimentjew. D, Flick. N. E, Bosselmann. T, Zhang J. Hypergraph-oriented 3D reconstruction, interpretation and analysis of air flows. *Int J MechatronAutom* 2011; 1(1): 9-18.
- [78] Cowen. E. A, Monismith. S. G. A hybrid digital particle tracking velocimetry technique. *Exp Fluids* 1997; 22(3): 199-211.
- [79] Kim. H. B, Lee. S. J. Performance improvement of two-frame particle tracking velocimetry using a hybrid adaptive scheme. *Meas Sci Technol* 2002; 13: 573-82.
- [80] Stellmacher. M, Obermayer. K. A new particle tracking algorithm based on deterministic annealing and alternative distance measures. *Exp Fluids* 2000; 28(6): 506-18.
- [81] Li. D, Zhang. Y, Sun. Y, Yan W. A multi-frame particle tracking algorithm robust against input noise. *Meas Sci Technol* 2008; 19(10): 1054-64.
- [82] Kähler. C. J, Scharnowski. Cierpka. C. On the uncertainty of digital PIV and PTV near walls. *Exp Fluids* 2012; 52:1641–56.
- [83] Zhang. Y, Sun. Y, Wang. A, Topmiller. J. L, Bennett. J. S. Experimental characterization of airflows in aircraft cabins. Part II: Results and research recommendations. *ASHRAE T* 2005; 111(2): 53-9.
- [84] Wang. A, Zhang. Y, Sun. Y, Wang. X. Experimental study of ventilation effectiveness and air velocity distribution in an aircraft cabin mockup. *Build Environ* 2008; 43(3): 337-43.
- [85] Wang A. Quantifying air distribution, ventilation effectiveness and airborne pollutant in an aircraft cabin mockup [Ph.D. Thesis]. USA: University of Illinois at Urbana-Champaign; 2006.
- [86] Steinhoff. P, Schmidt. M, Resagk. C, Müller. D. Measurements with a redesigned 3D-PTV system in natural and mixed convection. In: *10th International Symposium on Particle Image Velocimetry*, Delft, The Netherlands, July 1-3, 2013.
- [87] Lubutova. E, Resagk. C, Tank. R, Müller. D, Putze. T, Maas. H-G. Visualization of large-scale flow structures in air using a novel 3D particle tracking velocimetry technique. In: *12th International Symposium on Flow Visualization*, German Aerospace Center(DLR), Gottingen, Germany, Sep. 2006.
- [88] Scholzen. F, Moser. A. Three-dimensional particle streak velocimetry for room air flows with automatic stereo-photogrammetric image processing. In: *ROOMVENT International Conference*, Yokohama, Japan, 1996. p. 555-62.

- [89]Sun. Y, Zhang. Y, Zhao. L, Wang X. An algorithm of stereoscopic particle image velocimetry for full-scale room airflow studies. *ASHRAE T* 2004; 110(1): 75-80.
- [90]Müller. D, Müller. B, Renz. U. Three-dimensional particle-streak tracking (PST) velocity measurements of a heat exchanger inlet flow -A new method to measure all three air-flow velocity components in a plane is applied to a steady-state three-dimensional flow. *Exp Fluids* 2001; 30(6): 645–56.
- [91]Rosenstiel. M, Grigat. R. Segmentation and classification of streaks in a large-scale particle streak tracking system. *Flow MeasInstrum* 2010; 21(1): 1-7.
- [92]Voelker. C, Maempel. S,Kornadt. O. Measuring the human body's microclimate using a thermal manikin. *Indoor Air* 2014; 24(6): 567–79.
- [93]SAI. (2012). Sage Action Inc. Bubble Generator Systems for Air Flow Visualization and Measurement. <http://www.sageaction.com/>.
- [94]Satake. S, Kanamori. H, Kunugi. T, Sato. K, Ito. T, Yamamoto. K. Parallel computing of a digital hologram and particle searching for microdigital-holographic particle-tracking velocimetry. *Appl Optics* 2007; 46(4): 538-43.
- [95]Satake. S. Study on high speed parallel algorithm using PC grid environment for visualization measurements by Digital Holographic Particle Tracking Velocimetry. *Comput Phys Commun* 2008; 178(1): 1-7.
- [96]Sun. H, Zhao. L, Zhang. Y. Evaluating RNG k- ϵ models using PIV data for airflow in animal buildings at different ventilation rates. *ASHRAE T* 2007; 113(1): 358-65.
- [97]Meslem. A, Dia.A, Beghein. C, Hassan. M.E, Nastase.I, Vialle.P.J.A comparison of three turbulence models for the prediction of parallel lobed jets in perforated panel optimization. *Build Environ* 2011; 46(11): 2203-19.
- [98]Sanjuan. C, Suarez. M. J, Blanco. E, Heras. M.d.R. Development and experimental validation of a simulation model for open joint ventilated façades. *Energ Buildings* 2011; 43(12): 3446-56.
- [99]Chami. N, Zoughaib. A. Modeling natural convection in a pitched thermosyphon system in buildings roofs and experimental validation using particle image velocimetry. *Energ Buildings* 2010; 42(8): 1267-74.
- [100]Keane RD, Adrian RJ. Optimization of particle image velocimeters. Part I: Double pulsed systems. *Meas. Sci. Technol* 1990; 1 (11):1202-15.
- [101]Keane RD, Adrian RJ. Optimization of particle image velocimeters. Part II: Multiple pulsed systems. *Meas. Sci. Technol* 1991; 2 (10):963-74.
- [102]Keane RD, Adrian RJ, Zhang Y. Super-resolution particle imaging velocimetry. *Meas. Sci. Technol* 1995; 6 (6):754-68.
- [103]Raffel M, Willert C, Werely S, Kompenhans J. *Particle Image Velocimetry: A Practical Guide*, Springer-Verlag, Berlin, 2007.
- [104]Fu S, Biwole PH, Mathis C.Particle Tracking Velocimetry for indoor airflow field: A review. *Build Environ* 2015; 87: 34-44.
- [105]Foucaut JM, Miliat B, PerenneN, Stanislas M. Characterization of different PIV algorithms using the EUROPIV synthetic image generator and real images from a turbulent boundary layer. In: *Particle Image Velocimetry: Recent Improvements. Proceedings of the*

- EUROPIV 2 Workshop. Zaragoza, Spain. Springer-Verlag, Berlin, 2004.
- [106]Cameron SM. PIV algorithms for open-channel turbulence research: Accuracy, resolution and limitations. *J Hydro-environ Res* 2011; 5(4): 247-62.
- [107]Shi S, Chen D. The development of an automated PIV image processing software - SmartPIV. *Flow Meas Instrum* 2011; 22 (3): 181-89.
- [108]Kim H, Westerweel J, Elsinga GE. Comparison of Tomo-PIV and 3D-PTV for microfluidic flows. *Meas. Sci. Technol* 2013; 24 (2):024007(1-12).
- [109]Lecordier B, Demare D, Vervisch LMJ, Reveillon J, TriniteM. Estimation of the accuracy of PIV treatments for turbulent flow studies by direct numerical simulation of multi-phase flow. *Meas. Sci. Technol* 2001; 12 (9): 1382-91.
- [110]Stanislas M, Okamoto K, KahlerCJ, WesterweelJ, Scarano F. Main results of the third international PIV Challenge. *Exp. Fluids* 2008; 45 (1): 27-71
- [111]Okamoto K, NishioS, Saga T, Kobayashi T. Standard images for particle-image velocimetry. *Meas. Sci. Technol* 2000; 11 (6), 685-91.
- [112]LecordierB, Westerweel J. The EUROPIV synthetic image generator (S.I.G.). In: *Particle Image Velocimetry: Recent Improvements. Proceedings of the EUROPIV 2 Workshop, Zaragoza, Spain. Springer-Verlag, Berlin, 2004.*
- [113]Kovaszny LIG. Laminar flow behind a two-dimensional grid. In: *Proc. Cambridge Philos. Soc, 1948.*
- [114]Keane RD, Adrian RJ. Theory of cross-correlation analysis of PIV images. *Appl. Sci. Res* 1992;49 (3):191-215.
- [115]Taylor ZJ, Gurka R, Kopp GA, Liberzon A. Long-duration time-resolved PIV to study unsteady aerodynamics. *Instrum&Meas, IEEE Tran on* 2010; 59(12): 3262-69.
- [116]Lewis JP. Fast Template Matching. In: *Vision Interface 95, Canadian Image processing and Pattern Recognition Society. Quebec City, Canada, 1995.*
- [117]Maas H G. Complexity analysis for the establishment of image correspondences of dense spatial target fields. *International Advances of Photogrammetry and Remote Sensing XXIX* 1992; (B5): 102-107.
- [118]Biwole PH, Krauss G, Favier E, Rusaouen G, Roux JJ. Non-stereoscopic 3D particle tracking velocimetry for full scale rooms. In: *Advanced building ventilation and environmental technology for addressing climate change issues. Kyoto, Japan, 2008.*
- [119]Groth J, Johansson A. Turbulence reduction by screens. *J. Fluid Mech* 1988; 197: 139–55.
- [120]Kuznik F. Etude expérimentale des jets axisymétriques anisothermes horizontaux se développant près d’une paroi. Application à la modélisation numérique des cavités ventilées. Ph.D. Dissertation, Institut National des Sciences Appliquées de Lyon, 2005.
- [121]Kühn M, Ehrenfried K, Bosbach J, Wagner C. Feasibility study of tomographic particle image velocimetry for large convective air flow. 14th IntSymp on Applications of Laser techniques to Fluid Mechanics, Lisbon, Portugal, 07-10 July, 2008.
- [122]Li J, Cao X, Liu J, Wang C, Zhang Y. Global airflow field distribution in a cabin mock-up measured via large-scale 2D-PIV. *Build Environ*, 93(2) (2015), 234-244.
- [123]Fu S, Biwole P.H, Mathis C. Numerical and experimental comparison of 3D particle

tracking velocimetry (PTV) and particle image velocimetry (PIV) accuracy for indoor airflow study. *Build Environ*, 100 (2016), 40-49.

[124]Bouguet J-Y. Camera Calibration Toolbox for Matlab, available on website http://www.vision.caltech.edu/bouguetj/calib_doc/ (consulted on October 8 2007).

[125]Ethier C.R, Steinman D.A. Exact fully 3D Navier-Stokes solutions for benchmarking. *Int J Num Meth Fluids*, 19 (1994),369-375.

[126]Cao G, Awbi H, Yao R, Fan Y, Siren K, Kosonen R, Zhang J. A review of the performance of different ventilation and airflow distribution systems in buildings. *Build Environ*. 2014 (73) 171-186.

[127]Nielsen PV. Models for the prediction of room air distribution. In: *Proceedings of the 12 th AIVC conference, Ottawa, Canada, 1; Sep 24-27, 1991*, pp, 55-71.

[128]Sandberg M, Wiren B, Claesson L. Attachment of a cold plane jet to the ceiling length of recirculation region and separation distance. In: *Proceedings of roomvent 1992*. pp. 489-99.

[129]Awbi HB, Gan G. Evaluation of the overall performance of room air distribution. In: *Proceedings of indoor air, vol. 3; 1993*. pp. 283-8.

[130]Lee H, Awbi HB. Effect of internal partitioning on indoor air quality of rooms with mixing ventilation-basic study. *Build Environ*.2004 39:127-41.

[131]Cao G, Ruponen M, Jarek K. Experimental investigation of the velocity distribution of the attached plane jet after impingement with the corner in a high room. *Energy Build* 2010; 42(6): 935-44.

[132]Krajcik M, Angela S, Bjarne W. Olesen air distribution and ventilation effectiveness in an occupied room heated by warm air. *Energy Build* 2012;12(55): 94-101.

[133]Kim JT, Zhang Z, Liberzon A, Zhang Y, Chamorro LP. On the Lagrangian features of circular and semicircular jets via 3D Particle Tracking Velocimetry. *Exp Therm Fluid Sci*. 2016; 77:306-16.